Regional and Seasonal Impact of Volcanic Eruptions on European Climate over the Last Centuries

Diplomarbeit

an der Philosophisch-naturwissenschaftlichen Fakultät
der Universität Bern

vorgelegt von

Erich Fischer
2003

Leiter der Arbeit:
Prof. Dr. Heinz Wanner
Geographisches Institut

(...) nubes, (...), ex quo monte (Vesuvium fuisse postea cognitum est), oriebatur, cuius similitudinem et formam non alia magis arbor quam pinus expresserit. nam longissimo velut trunco elata in altum quibusdam ramis diffundebatur, credo, quia recenti spiritu evecta, dein senescente eo destituta aut etiam pondere suo victa in latitudinem vanescebat, candida interdum , interdum sordida et maculosa, (...)

Plinius, Epistula XVI. In his letter to Tacitus, Plinius (109) described the plume of the devastating Vesuvius eruption in A.D. 79.

In the summer of 1816 we visited Switzerland, and became the neighbors of Lord Byron (...) But it proved a wet, ungenial summer, and incessant rain often confined us for days to the house (...) "We will each write a ghost story," said Lord Byron; and his proposition was acceeded to (...) I busied myself to think of a story,— a story to rival those which had excited us to this task. One which would speak to the mysterious fears of our nature, and awaken thrilling horror (...)

Mary Shelley, 1816. Inspired by the pervasive gloom from Tambora's dust—she wrote the immortal Gothic horror novel *Frankenstein* (de Boer and Sanders 2002).

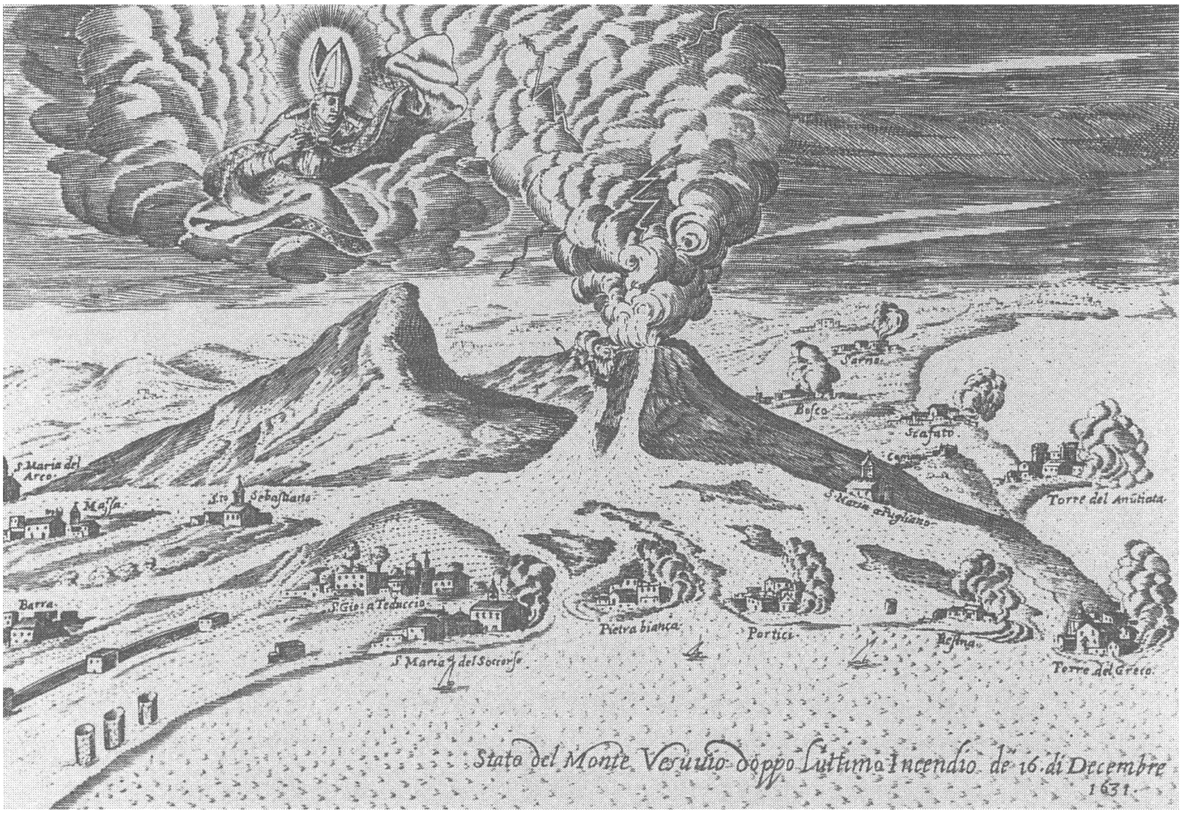

Figure 1: *An old lithographic depicting the 1631 eruption of Vesuvius, showing Saint Januarius imploring the volcano to cease its destructive activity (de Boer and Sanders 2002)*

Abstract

Volcanic eruptions are an important natural cause of climate variations. The climate response to explosive volcanic eruptions has been studied extensively on a hemispherical and global scale within the instrumental period. A new compilation of 500 year spatio-temporal highly resolved reconstructions, recently developed for Europe, offers extended insight into the impact of major volcanic eruptions on a continental scale. The reconstructions include monthly temperature and precipitation fields (seasonal before 1658) over the European land areas as well as sea level pressure and 500 hPa geopotential height fields over the North Atlantic / European region. These reconstructed fields are used to precisely investigate the seasonal climate response to major volcanic eruptions on a regional scale.

I calculated seasonal anomalies of European climate following selected major volcanic eruptions over the last centuries. Composite analysis is performed to identify the mean climate response to large volcanic eruptions. Statistical significance of the anomalies is established at every grid point using the non-parametric Mann-Whitney test and a Monte Carlo resampling procedure.

The composite temperature field for the first and second summer after an eruption reveals cooling in most parts of Europe, with a significant maximum during the second post-eruption summer. The negative temperature anomalies are found to be most pronounced over southern Scandinavia and the Baltic. The cooling is suggested to be caused by radiative forcing due to scattering of stratospheric aerosols. The mean winter temperature pattern in the two years following tropical eruptions is dominated by a strong warming, in particular over Northern Europe (more than +2°C), and somewhat cooler conditions over the eastern and western Mediterranean. These findings are consistent with previous observational and GCM studies. Furthermore, they provide more evidence on the spatial distribution of the post-eruption temperature anomalies.

The winter warming is associated by a SLP pattern resembling a strong positive NAO mode. The composite NAO index, reconstructed over the past five centuries, revealed to be significantly positive during the second winter following the selected volcanic eruptions. The geopotential height field shows similar centres of negative and positive anomalies indicating a strong north-south pressure gradient over Europe. This gradient leads to enhanced geostrophic west winds, which are suggested to transport warm and moist air to the areas of maximum winter warming. The composite precipitation field during winter shows positive precipitation anomalies over the British Isles and Scandinavian west coast and drier conditions over the Eastern Mediterranean.

Finally, the results suggest a reversal of the primary response of the winter NAO index and summer and winter temperature to opposite conditions in the third, fourth or fifth year. This finding is independent from previous analyses on the European volcanic signal. A similar post-eruption alteration has recently been detected in the ENSO.

The results reveal a large potential of the composite analysis of climate reconstructions to identify the volcanic effects on climate. Combined with model simulations the method would provide optimal skills for an integrated understanding of volcanic effects on climate at the continental scale.

Zusammenfassung

Vulkanausbrüche sind eine wichtige Ursache natürlicher Klimavariabilität. In diversen Studien wurde der Einfluss von Vulkanen auf das globale Klima mittels Messdaten ausführlich untersucht und dokumentiert. Neue zeitlich und räumlich hochaufgelöste Klimarekonstruktionen Europas ermöglichen nun eine Untersuchung der vulkanischen Einflüsse während der letzten 500 Jahre auf kontinentaler Ebene. Der von uns verwendete Klimadatensatz umfasst sowohl monatliche (saisonale vor 1658) Temperatur- und Niederschlagsfelder für das europäische Festland, als auch Bodendruckfelder und 500 hPa Geopotentialfelder für Europa und den Nordatlantik. Die statistisch rekonstruierten Felder basieren auf instrumentellen Messdaten sowie natürlichen und historischen Klimaarchiven. Diese Rekonstruktionen erlauben uns die Berechnung der mittleren vulkanbedingten Klimaanomalien in den verschiedenen Regionen Europas.

Mittels Compositing berechneten wir das durchschnittliche Anomaliefeld nach 16 ausgewählten grossen Ausbrüchen und bestimmten somit den Vulkaneinfluss auf das europäische Klima. Die Signifikanz des Signals wurde mit dem Mann-Whitney Test und in einem zweiten Schritt mit einer Monte Carlo Analyse getestet.

Auf der Basis dieser Daten kann gezeigt werden, dass es während dem ersten und besonders dem zweiten Sommer nach einem grossen Vulkanausbruch in Europa signifikant kühler ist als vor dem Ausbruch. Dies zeigt sich am ausgeprägtesten in Südskandinavien und den baltischen Staaten. Die Abkühlung im Sommer kann durch die Streuung des Sonnenlichts an vulkanischen Aerosolen in der Stratosphäre erklärt werden. Im Gegensatz zum Sommer führen Vulkane im Winter zu einer Erwärmung des europäischen Festlandes während den ersten beiden Jahren. Über Nordeuropa ist die Temperaturabweichung mit über +2°C am stärksten. Unsere Resultate zeigen eine gute Übereinstimmung mit verschiedenen früheren Untersuchungen der instrumentellen Periode und Klimamodellen. Die höhere räumliche Auflösung und die längere Untersuchungsperiode erlauben uns aber eine genauere Bestimmung der regionalen bis kontinentalen Auswirkungen über eine längere Zeitspanne.

Neben möglichen strahlungsbedingten Veränderungen dürfen die zirkulationsbedingten Einflüsse nicht unterschätzt werden. Gleichzeitig mit der Temperaturerwärmung zeigt

nämlich das mittlere Bodendruckfeld im Winter eine Anomalieverteilung, die einem positiven NAO-Druckmuster sehr ähnlich sieht. Die Zentren positiver und negativer Anomalien der Geopotentialhöhe deuten entsprechend auf einen überdurchschnittlichen Nord-Süd Gradient hin. Dieser Gradient führt zu stärkeren geostrophischen West-/Südwestwinden über Westeuropa, die im Winter oft warme, maritime Luft zum europäischen Kontinent transportieren. Die stärkeren Westwinde sind verbunden mit positiven Niederschlagsanomalien über Grossbritannien und der Westküste Skandinaviens während den ersten beiden Wintern nach Vulkaneruptionen.

Die vorliegenden Resultate verdeutlichen das grosse Potential der Analyse von Klimarekonstruktionen zur Bestimmung des saisonalen und regionalen Vulkaneinflusses. Optimale Erkenntnisse für das Verständnis des vulkanischen Strahlungsantriebs (Forcing) sind allerdings nur durch eine Kombination mit Klimamodellsimulationen zu erreichen. Ausserdem zeigt die Arbeit die wichtige Rolle des vulkanischen Einflusses auf das europäische Klima während den letzten 500 Jahren auf.

Acknowledgements

This diploma thesis could not have been completed without the motivation and contribution of various persons. In particular I would like to acknowledge:

Dr. Jürg Luterbacher, my tutor, for his motivating support and the excellent supervision. In particular I appreciated to be integrated in the research process having the possibility to present my results at different project meetings. Moreover, I would like to thank him for providing the latest reconstruction data and for his comments on the diploma concept and previous versions of the manuscript.

Prof. Dr. Heinz Wanner, head of the climatology and meteorology research group (KLIMET), for offering me the opportunity to work in this interesting field in his research group and to present the results at the EGS/AGU Joint Assembly 2003 in Nice.

Dr. Caspar Ammann from the NCAR, for his advice during his visit in February 2003, for the helpful comments by e-mail and for providing the latest eruption data.

Pavel Michna, Nicolas Schneider and Carlo Casty for their persistent help solving statistical and programming problems.

This Rutishauser, Urs and Patrick Fischer for their corrections and valuable comments on the manuscript.

The developers of the GrADS software, the R software environment and all the other contributors to the Open Source Software Projects used in this diploma thesis.

The members of the KLIMET, especially my “roommates”, for the good working atmosphere and the assistance in all sorts of problems.

Last but not least, special thanks to Susanne Hak and my family for their encouragement and support and to my friends, especially Matthias Walter, Andreas Hauri, Cornelia Lätsch and Jeanne Gerber, for the necessary distraction and motivation during leisure time.

Contents

List of Figures

List of Tables

Abbreviations

CRU	Climatic Research Unit (University of East Anglia)
DVI	Dust Veil Index
ENSO	El Niño Southern Oscillation
EOF	Empirical Orthogonal Function
GCM	General Circulation Model
GPH_{500}	Geopotential Height on the 500 hPa level
hPa	Hectopascal
ITCZ	Innertropical Convergence Zone
IVI	Ice-core-volcano Index
Lidar	Light Detection and Ranging
NAO	North Atlantic Oscillation
NAOI	North Atlantic Oscillation Index
NCAR	National Center of Atmospheric Research
NCCR	National Center of Competence in Research
NCEP	National Centres for Environmental Prediction
NH	Northern Hemisphere
PALVAREX	Paleoclimate Variability and Extreme Events
QBO	Quasi-Biennial Oscillation
RE	Reduction of Error
SE	Standard Error
SEA	Superposed Epoch Analysis
SH	Southern Hemisphere
SLP	Sea Level Pressure
SOI	Southern Oscillation Index
TOMS	Total-Ozone Mapping Spectrometer
VAI	Volcanic Aerosol Index
VEI	Volcanic Explosivity Index

Chapter 1

Introduction

Global climate change is one of the major scientific issues of the last few decades, largely because it has a potentially greater impact on society in the long term than almost any other phenomenon. Furthermore, civilisation itself is deeply involved through anthropogenic changes in the composition of the atmosphere (Bertrand et al. 1999). Changes in climate occur as a result of internal variability within the climate system and external factors (both natural and anthropogenic). These external factors include increases in the atmospheric concentration of greenhouse gases and aerosols, losses of stratospheric ozone and land-use changes (anthropogenic factors) as well as explosive volcanic eruptions, changes in the orbital elements and in solar irradiance (natural factors) (IPCC 2001, Wanner et al. 2000a). The influence of external factors on climate can be broadly compared using the concept of radiative forcing. Radiative forcing is an externally imposed perturbation in the radiative energy budget of the Earth's climate system (IPCC 2001). It is a fundamental challenge to determine how much of observed climate change is a response to radiative forcing, as opposed to chaotic variability (Hansen et al. 2002). One important radiative forcing is caused by volcanic eruptions.

Volcanism has long been implicated as a possible cause of weather and climate variations. Already 2000 years ago, Plutarch and others pointed out that the eruption of Mount Etna in 44 B.C. dimmed the sun and that the resulting cooling caused crops to shrivel and produced famine in Rome and Egypt (Forsyth 1988). Benjamin Franklin suggested that the Laki eruption in Iceland in 1783 might have been responsible for the abnormally cold summer of 1783 in Europe and the cold winter of 1783–1784 (Franklin 1784). Humphreys (1913, 1940) associated cooling events after large volcanic eruptions with the radiative effects of the stratospheric aerosols but did not have sufficiently long or horizontally extensive temperature database to quantify the effects (Robock 2000). Mitchell (1961) was the first to conduct a composite analysis, averaging the effects of several eruptions to isolate the volcanic climate response from other fluctuations (Robock 2000). Lamb (1970) intensified the research on this subject and strongly influenced the modern study on the impact of volcanic eruptions on climate (Kelly et al. 1998). Lamb (1970) developed the Dust Veil Index (DVI) as the first single number to evaluate and compare the atmospheric and climatic impact of past eruptions (Zielinski 2000). The DVI was developed based on the assumption that the volcanic dust loading in the atmosphere is the direct cause of the climate response (Graf 2002). It was only by satellite measurements after the El Chichon eruption 1982 that the major climatic impact of volcanic sulphur aerosols was recognised. Detailed studies of the impact of the 1991 Pinatubo eruption and continuing analyses of the El Chichon eruption resulted in a deeper understanding of the complex impacts of volcanic eruptions on climate. Several excellent reviews of the effects of volcanoes on climate include Robock (1991, 2000), Zielinski (2000), and Graf (2002).

1.1 Problem Definition and Objectives

The surface temperature response to explosive volcanic eruptions has been extensively studied on a hemispherical and global scale within the instrumental period. However, the investigation of the climatic response to volcanic eruptions was rarely extended further back in time than 1780, due to lacking temperature data. Prominent exceptions are the works by Briffa et al. (1998) and Mann et al. (1998) evaluating the volcanic signal over 600 years. Briffa et al. (1998) used tree-ring-density chronologies to investigate the influence of volcanic eruptions on Northern Hemisphere summer temperature, and Mann et al. (1998) calculated time-dependent correlations of surface temperature reconstructions with volcanic aerosols.

The statistical analyses often use area-averaged or low resolution data, which do not allow a detailed interpretation of the climate impact on regional scale. The volcanic impact on other climatic parameters than temperature is poorly understood. Recent publications revealed a correlation between volcanic eruptions and teleconnections such as El Niño (Kirchner et al. 1999), Arctic Oscillation (Stenchikov et al. 2002), and North Atlantic Oscillation (Graf et al. 1994).

The main objective of this work includes the detailed investigation of the climatic response to major volcanic eruptions over the last 500 years. A new compilation of 500-year spatio-temporal highly resolved climatic reconstructions, recently developed for the North Atlantic / European region (Luterbacher et al. 2003), allows to get an extended insight into the impact of major volcanic eruptions on a continental scale. I emphasise on the consideration of tropical volcanic eruptions, since most of the major eruptions occurred in the tropics and since the winter climate response is highly dependant on the latitude of the volcano (Robock and Free 1995). The main objective is divided in several sub-objectives:

- **Direct radiative forcing on temperature**
  Various publications suggest a global surface cooling of 0.2–0.6°C mainly during summer in the 1–3 post-eruption years (Robock and Mao 1995, Robock 2000, Parker et al. 1996). A similar signal is expected in the surface temperature reconstructions. I focus on evaluating spatial distribution, magnitude and statistical significance of the temperature response to eruptions.

- **Indirect, dynamical effects on the atmospheric circulation**
  It is difficult to separate the direct and indirect volcanic impact on surface temperature. Based on theory and climate model simulations indirect, dynamical effects are suggested to be dominant in post-eruption winters and rather weak, compared to the direct radiative effects, in summer. I use reconstructions of sea level pressure (SLP) fields and 500 hPa geopotential height fields over the eastern North Atlantic and Europe to get extended insight into the indirect changes in atmospheric circulation following volcanic eruptions.

- **Volcanic effects on precipitation**
  Volcanic effects on precipitation are very poorly investigated. Robock and Liu (1994) analysed the Goddard Institute for Space Studies three-dimensional model simulations (Hansen et al. 1988) and found reduced tropical precipitation for 1–2 years following large eruptions. They also found a reduction in Sahel precipitation, that matched the observed enhancement of the Sahel drought following the El Chichon 1982 eruption. However, this result needs further confirmation before it can be considered robust (Robock 2000). I perform preliminary calculations on the volcanic impact on European seasonal precipitation reconstructions.

- **Duration of the volcanic perturbations and timing of the maximum effect**
  Robock and Free (1995) showed that individual large eruptions produce global or hemispheric summer cooling for two or three years with a maximum cooling approximately one year after the eruptions. The winter warming over northern hemispheric land regions is suggested to occur in the first and second winter after a major volcanic eruption (Robock and Mao 1992). In this study the duration of the volcanic signal and the timing of the maximum effect in Europe will be of major interest.

- **Reversal of the volcanic response to the opposite conditions**
  Volcanic forcing is believed to result in a short and strong disturbance of the Earth's climate system before it is returning to a pre-eruption state. Adams et al. (2003) reexamined the connection between El Niño and volcanic eruptions. They found an initial tendency towards an El Niño-like response subsequently followed by a reversal into a La Niña like state. The results suggest that the volcanic forcing tends to set up and pace

a pattern of El Niño/La Niña-like alternation, before the response to the event appears to finally be damped out by internal variability. I intend to examine the North Atlantic Oscillation (NAO) and the European temperature for a similar rebound effect.

1.2 Structure of Thesis

After the introduction a theoretical overview with regard to the mechanisms of injection, transport of the volcanic cloud, SO_2 conversion to sulphate aerosols and the resulting radiative, dynamical and chemical effects is given. The third chapter includes descriptions of the temperature, precipitation, pressure and volcanic data. The methods and statistical procedures are explained in chapter four. The fifth chapter focuses on the presentation of the results, which are discussed and compared with other publications in chapter six. The conclusions are summarised in chapter seven. Finally, further research topics with respect to the climate response to volcanic eruptions are described in the outlook.

Chapter 2

Climatic Response to Volcanic Eruptions - A Review

The influence of volcanic eruptions on climate is rather complex. It can generally be subdivided in radiative, dynamical and chemical effects, which are all addressed in detail in this chapter. The effects are summarised in table 2.1 containing mechanism, beginning and timescale. In figure 2.1 the mechanisms are illustrated in a schematic diagram.

Volcanic eruptions can inject tens of teragrams of chemically and microphysically active gases and solid aerosol particles into the stratosphere. This affects the Earth's radiative balance and disturbs the stratospheric chemical equilibrium (Stenchikov et al. 1998). The major component of volcanic eruptions is magmatic material, which emerges as solid, lithic material or solidifies into large particles, which are referred to as ash or tephra. These particles fall out of the atmosphere very rapidly. Small amounts can remain in the stratosphere for a few months but have very small climatic impacts. Investigations after the 1883 Krakatau and the 1980 Mount St. Helens eruption showed that this temporary large atmospheric loading reduced the amplitude of the diurnal cycle of surface air temperature in the region of the tropospheric cloud (Robock and Mass 1982). The devastating Mount St. Helens eruption produced a huge local tropospheric loading of volcanic ash. In Yakima, Washington, 135 km to the east, it became so dark that automatic streetlights went on in the middle of the day. This thick layer effectively isolated the Earth's surface from the top of the atmosphere (Robock 2000). In Yakima, on the day of the eruption, the normal morning rise of temperature was completely halted by the arrival of the volcanic dust cloud. The temperature remained at 15°C for 11 hours independent of the normal diurnal cycle. Robock and Mass (1982) compared the measured surface temperature in Yakima with the model output statistic forecast produced by the National Weather Service. As the model did not include volcanic aerosols as predictors, they were able to interpret these errors as the volcanic effect. They found that the aerosols cooled the surface by as much as 8°C in the daytime and warmed it by 8°C at night.

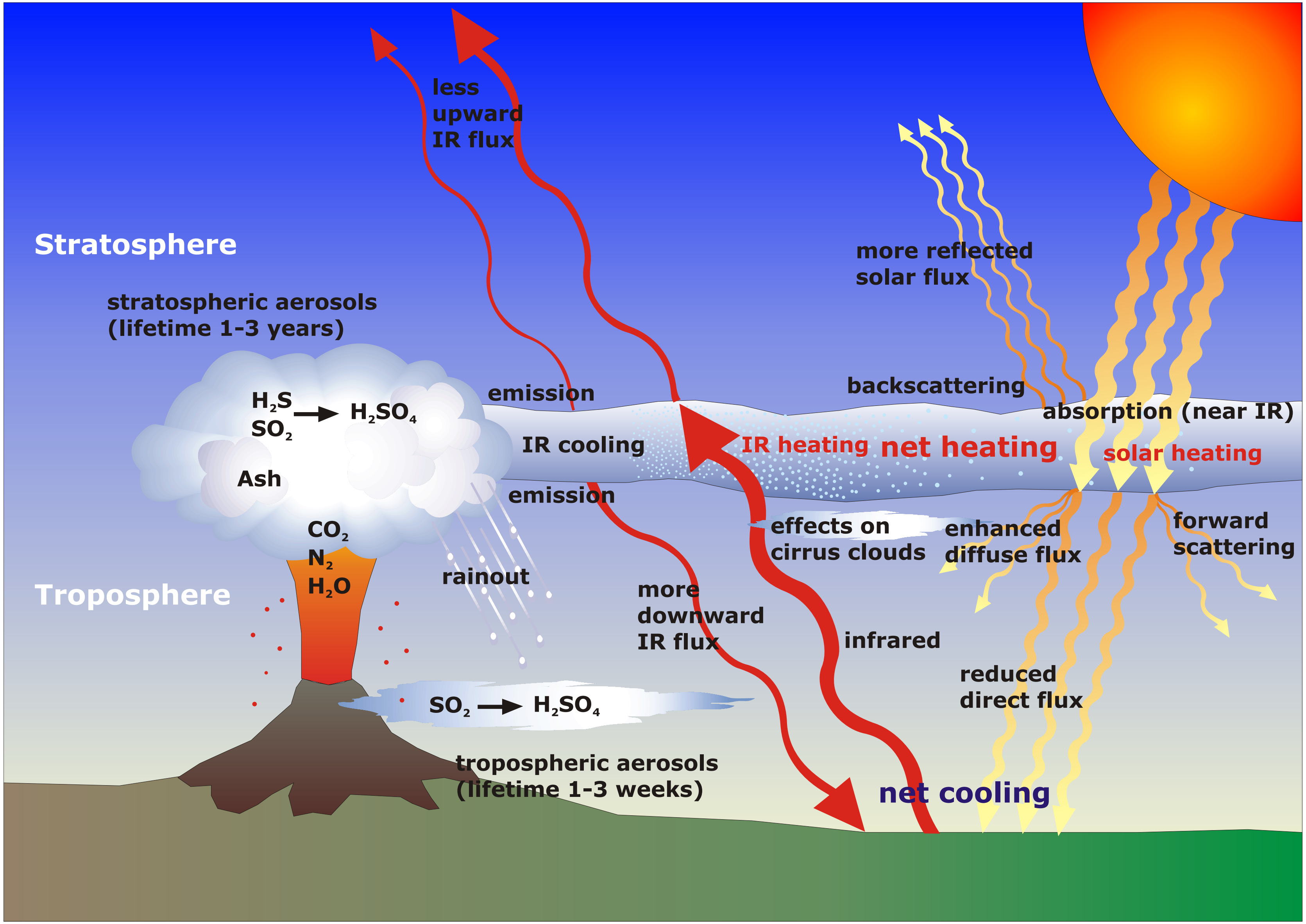

Figure 2.1: *Schematic diagram of volcanic inputs to the atmosphere and their effects (as proposed by Robock 2000 and McCormick et al. 1995).*

The most important climatic effect of explosive volcanic eruptions is through their emission of sulphur species to the stratosphere, mainly in the form of SO_2 (Newhall and Self 1982), sometimes as H_2S. These sulphur species react with OH and H_2O to form H_2SO_4 (Sulphuric Acid) on a timescale of weeks and the resulting H_2SO_4 aerosols produce the dominant radiative effect from volcanic eruptions (Robock 2000). Bluth et al. (1992) estimated from satellite measurements that the 1982 El Chichon eruption injected seven megatons of SO_2 into the atmosphere, and the 1991 Pinatubo eruption 20 megatons, respectively. Once injected into the stratosphere, the aerosols are rapidly dispersed around the globe. In the case of tropical eruptions, the aerosols are transported around the globe and commonly spread poleward into both hemispheres (Ammann and Naveau 2003). Observations after the 1982 El Chichon and the 1991 Pinatubo eruptions showed that the aerosol cloud circled the earth in three weeks (Bluth et al. 1992). Although El Chichon (17°N) and Pinatubo (15°N) are separated by only 2° of latitude, their clouds, after only one circuit around the globe ended up separated by 15° of latitude (Robock 2000). The dispersal of the aerosols into each hemisphere can be asymmetrical as a function of time of the year, location of the intertropical convergence zone (ITCZ), and the quasi-biennial oscillation (QBO) (Zielinski 2000).

2.1 Radiative Forcing

Volcanic aerosols scatter visible solar radiation, reflect and absorb in the near-infrared bands, and absorb and emit thermal longwave radiation, providing significant radiative forcing of the climate system (Stenchikov et al. 1998). The resulting disturbance to the Earth's radiation balance affects surface temperatures through direct radiative effects as well as through indirect effects on the atmospheric circulation (Robock 2000). The sulphate aerosols scatter incoming solar radiation to space, increasing planetary albedo and cooling the Earth's surface and troposphere (Bertrand et al. 1999). This backscattering is the dominant radiative effect at the surface and results in a net cooling there (Robock 2000). Much of the solar radiation is forward scattered, resulting in enhanced downward diffuse radiation that somewhat compensates for a large reduction of the solar radiation. The effect on solar radiation is so strong that it can easily be seen by the naked eye, making the normally blue sky milky white. The reflection of the sunlight at the lower end of the stratospheric volcanic aerosol layer produces the characteristic red sunset. The famous Edvard Munch painting "The Scream" (figure 2.2) shows a red volcanic sunset over the Oslo harbour produced by the 1892 Awu eruption (Robock 2000). Apart from the scattering of solar radiation, the absorption of radiation plays an important role in the energy budget (Graf 2002). To evaluate the effects of a volcanic eruption on climate, the radiative forcing from the aerosols must be calculated (Robock 2000). Stenchikov et al. (1998) showed that a complete formulation of radiative forcing for aerosols

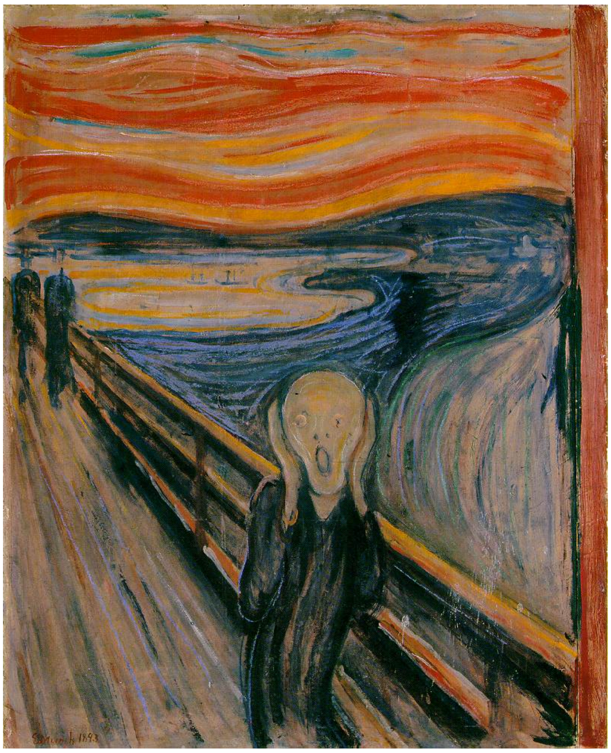

Figure 2.2: *The Scream, painting by Edvard Munch 1893.*

with nonuniform horizontal and vertical distribution is rather complex. It must include not only the changes of net fluxes at the tropopause, but also the vertical distribution of atmospheric heating rates and the change of downward thermal and net solar radiative fluxes at the surface. At the top of the aerosol cloud, the atmosphere is warmed by absorption of solar radiation in the near-infrared. This effect dominates over the enhanced infrared cooling due to the enhanced emissivity because of presence of aerosols (Andronova et al. 1999). In the lower stratosphere the atmosphere is heated by absorption of upward longwave radiation from the troposphere and surface (Robock 2000). In the troposphere, there are small radiative effects, since the reduced downward near-infrared is compensated by the additional downward longwave radiation from the aerosol cloud. At the surface the large reduction in direct shortwave radiation overwhelms the additional downward diffuse shortwave flux and the small additional downward longwave radiation from the aerosol cloud, except in the polar night, where there is no sunlight (Harshvardhan 1979).

2.2 Dynamical Effects

The heating of the stratospheric aerosol layer is of higher magnitude in the tropics, where the surface temperatures are highest and the solar radiation is strongest (Graf 2002). Especially for tropical eruption, as Pinatubo 1991, the lower stratosphere heating is much larger in the tropics than at the poles. It is this latitudinal gradient of heating which sets up a dynamical response in the atmosphere. This dynamical response results in circulation anomalies in both the stratosphere and the troposphere, and often dominates over the direct radiative effects in winters following tropical eruptions. The perturbation of the temperature gradient results in an enhanced polar vortex in the lower stratosphere and strengthening of the westerlies in the winter (Kirchner et al. 1999, Mao and Robock 1998). A coupling between the stratosphere and troposphere causes the dynamic signal to penetrate downward and modifies the tropospheric circulation patterns. This dynamic feedback mechanism produces winter warming and provides a very important contribution to the resulting climate change (Robock and Mao 1992, Robock and Mao 1995, Kirchner et al. 1999). The winter warming was observed after several volcanic eruptions during the 20th century. However, it was difficult to isolate the effect because it often occurred simultaneously with a strong El Niño. Several attempts were made to separate the two signals by statistical methods (e.g. Robock and Mao 1992, Robock and Mao 1995, Mass and Portman 1989) and by climate modelling (e.g. Kirchner and Graf 1995). Generally the winter surface temperature warming was strongest in the mid-latitudes with a maximum over Eurasia, whereas a cooling in the first and second winters occurred over the oceans and over the Middle East (Graf 2002). In the low-latitudes a cooling was observed in all seasons. After the Pinatubo eruption 1991 higher than normal temperatures were observed in the lower troposphere over Northern America, Europe and Siberia, meanwhile Greenland, the Middle East and south-eastern Asia were cooling (Graf 2002). In both the first and second winter it was snowing in Jerusalem and large populations of corals in the Red Sea died. The temperature anomalies showed a large-scale wave-like pattern in contrast to the cooling over the mid- and high-latitude continents, which would be expected due to the radiative forcing. Obviously there have to be strong dynamical effects influencing the circulation in the mid-latitudes and the structure of the planetary waves (Graf 2002). Perlwitz and Graf (1995) showed a direct relationship between the strength of the winter polar vortex in the lower stratosphere and the phase and the amplitude of planetary waves in the troposphere. An enhanced polar vortex results in a structure of the planetary waves that corresponds to the observed temperature anomalies after volcanic eruptions (Graf 2002).

Observations show that strong equatorial volcanic eruptions have been followed by a pronounced positive phase of the Arctic Oscillation (AO) for one or two Northern Hemisphere winters. Stenchikov et al. (2002) showed that the enhanced polar vortex forces a positive phase of the AO. The positive phase of the AO is not only caused by aerosol heating in the lower tropical stratosphere. Stenchikov et al. (2002) showed by experiment that only a tropospheric effect of aerosols is sufficient to force a positive AO phase. Aerosol-induced tropospheric cooling in the subtropics decreases the meridional temperature gradient in the

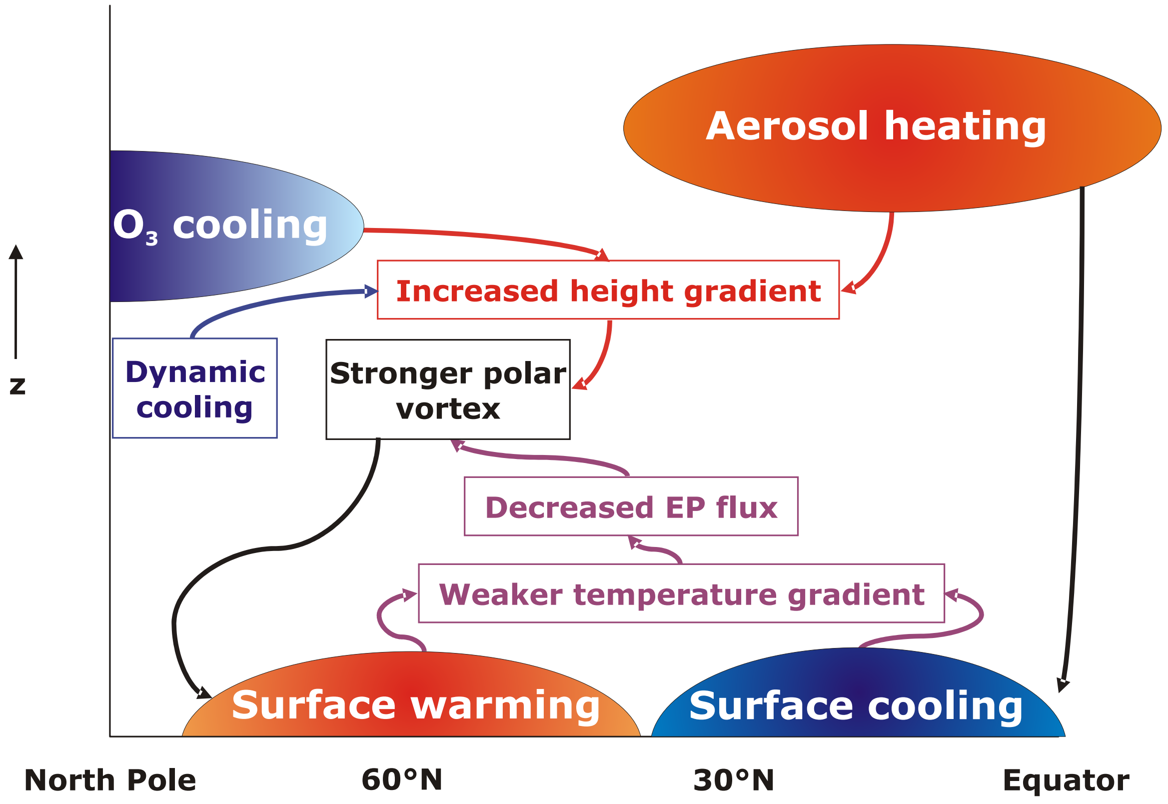

Figure 2.3: *Schematic diagram of how the stratospheric gradient and tropospheric gradient mechanisms are triggered by volcanic aerosol clouds in the tropical stratosphere (after Stenchikov et al. 2002).*

winter troposphere between 30°N and 60°N. The corresponding reduction of mean zonal energy and amplitudes of planetary waves in the troposphere decreases wave activity flux into the lower stratosphere. The resulting strengthening of the polar vortex forces a positive phase of the AO (Stenchikov et al. 2002). This mechanism is schematically illustrated in figure 2.3.

Franklin (1784) noted that the winter in Europe following the 1783 Laki eruption was extremely cold rather than warm. Because Laki was a high-latitude eruption, it could have produced high-latitude stratospheric heating during the winter of 1783/84 and a reduced pole-to-equator temperature gradient (Robock 2000). This theory suggests that the opposite phase of the pattern discussed above was produced, associated with a large negative NAO anomaly. This suggestion is being tested with GCM experiments (Robock 2000).

2.3 Chemical Effects

Volcanic aerosols have the potential to change not only the radiative flux in the stratosphere, but also its chemistry. The most important chemical changes in the stratosphere are related to ozone, which has significant effects on ultraviolet and longwave radiative fluxes (Robock 2000). The reactions which produce and destroy ozone depend on the ultraviolet flux, the temperature, and the presence of surfaces for heterogeneous reactions, all of which are changed by volcanic aerosols (Graf 2002). The heterogeneous chemistry responsible for the ozone hole over Antarctica, occurs on polar stratospheric clouds in the extremely cold isolated spring vortex in the Southern Hemisphere. Sulphate aerosols produced by volcanic eruptions can also provide these surfaces for ozone depletion at lower latitudes and at all times of the year (Graf 2002). Quantifying the effects of volcanic aerosols on the amount of ozone is difficult, as chemical and dynamical effects occur simultaneously. Nevertheless, attempts were made after the 1991 Pinatubo eruption to estimate the effects on ozone. Column ozone reduction ranging from about 2% in the tropics to about 7% in the mid-latitudes and up to 30% in the aerosol cloud itself was observed (Robock 2000). Decrease of the ozone concentration causes less ultraviolet absorption in the stratosphere, which modifies the aerosol heating effect (Graf 2002). The volcanic effect on ozone chemistry is a new phenomenon, dependent on anthropogenic chlorine in the stratosphere. Because of the Montreal protocol 1987, an international agreement designed to protect the stratospheric ozone layer, chlorine concentration has peaked in the stratosphere and is now decreasing. Therefore ozone effects will go away in the future and volcanic eruptions will have a stronger effect on atmospheric circulation without the negative feedback produced by ozone depletion (Robock 2000).

Table 2.1: *Effects of Large Explosive Volcanic Eruptions on Weather and Climate (Robock 2000).*

Effect	Mechanism	Beginning	Duration
Reduction of diurnal cycle	blockage of shortwave and emission of longwave radiation	immediately	1–4 days
Reduced tropical precipitation	blockage of shortwave radiation, reduced evaporation	1–3 months	3–6 months
Summer cooling of NH tropics and subtropics	blockage of shortwave radiation	1–3 months	1–2 years
Stratospheric warming	stratospheric absorption of short- and longwave radiation	1–3 months	1–2 years
Winter warming of NH continents	stratospheric absorption of short- and longwave radiation, dynamics	$\frac{1}{2}$ year	one or two winters
Global cooling	blockage of shortwave radiation	immediately	1–3 years
Global cooling from multiple eruptions	blockage of shortwave radiation	immediately	10–100 years
Ozone depletion, enhanced ultraviolet	dilution, heterogeneous chemistry on aerosols	1 day	1–2 years

Chapter 3

Data

A compilation of spatio-temporal highly resolved estimates of past climate were used to assess the climatic response to volcanic eruptions. The climate reconstructions include monthly gridded temperature, precipitation, sea level pressure (SLP) and 500 hPa geopotential height fields back to 1659 and seasonal reconstructions from 1500–1658 for the eastern North Atlantic / European region. The volcanic data used in this study is a combination of different volcanic indices and the dating of the volcanic eruptions is based on a compilation by Simkin and Siebert (2003). All data sets are presented in detail in this chapter.

3.1 Temperature and Precipitation Data

The land temperature and precipitation reconstructions (given on a $0.5° \times 0.5°$ grid) were developed by Luterbacher et al. (2003) using principal component regression analysis based on the combination of early instrumental station series (pressure, temperature and precipitation) and documentary proxy data from Eurasian sites. The relationships were derived over the 1901–1960 calibration period and verified over the period 1961–1995. For the period 1901–1998 the temperature and precipitation data set by New et al. (2000) was used.

3.1.1 Predictor Data

The available time series of documentary proxy and early instrumental data and the domain of the reconstructed area are presented in figure 3.1. Red circles/triangles mark time-varying instrumental series, which were provided by different sources. Blue circles/triangles mark data series, which include not directly measured values, but were estimated from high-resolution documentary evidence. These temperature, precipitation and other paleoenvironmental indices are estimations from very high-resolution documentary proxy data, such as observations

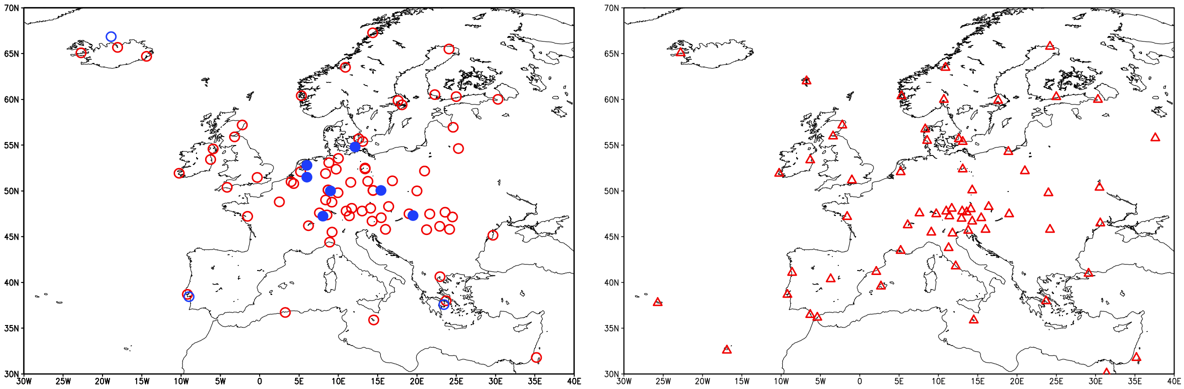

Figure 3.1: *Geographical distribution of the temperature (left panel) and pressure (right panel) predictor locations. Red circles/triangles indicate instrumental data series, blue circles indicate data series estimated from high-resolution documentary evidence. Solid circles mark data series available before 1659 and open circles/triangles data series and indices for the post-1659 period. The precipitation predictors are not shown.*

of ice and snow features, and phenological and biological observations. Prior to 1659 only reconstructed climatic indices on a seasonal resolution are available (Luterbacher et al. 2002b).

3.1.2 Predictands

The dependent variables (predictands) consist of gridded temperature and precipitation fields (0.5°× 0.5°) of the land areas from 25°W to 40°E and 35°N to 70°N. The reconstructions are monthly resolved back to 1659 and seasonally for the period 1500–1658. However, in this study all the data are seasonally averaged for winter, spring, summer and autumn (winter is December, January and February (DJF); spring=(MAM); summer=(JJA); autumn=(SON)).

The monthly temperature and precipitation data for the period 1901–1990 were provided by New et al. (2000). They have the same spatial resolution (0.5°× 0.5°) and are used as calibration data set for the temperature and precipitation reconstructions by Luterbacher et al. (2003) (cf. section 3.1.3). New et al. (2000) interpolated fields of monthly temperature and precipitation anomalies from station data compiled by the Climatic Research Unit (CRU) (see New et al. (2000) for details).

3.1.3 Reconstruction Method

In this section the reconstruction method of the temperature and precipitation is shortly summarised based on Luterbacher et al. (2002b). Principal component regression analysis was used to develop monthly temperature and precipitation reconstructions back to 1659 and seasonal reconstructions from 1500–1658.

In order to reconstruct the gridded temperature and precipitation fields all predictors were first identified for which data were available for that particular month (season) and all other months from the same climatological season (e.g. December, January, February). Due to the large time-varying data base over the last centuries, more than 400 different models for each parameter had to be developed. Statistical models of the relationship between predictors, and gridded temperature and precipitation (predictands) were developed and applied to data over a calibration period (1901–1960). The transfer functions were then applied to the corresponding predictor variables for the independent verification period 1961–1995. The temperature record was reconstructed using temperature and pressure predictors, whereas the precipitation fields were reconstructed by precipitation and pressure predictors (cf. figure 3.1.)

In the following the statistical details are presented, illustrated by the example of the temperature reconstruction method, based on Luterbacher et al. (2002b). Let $T_{calib}(t, x)$ denote the mean monthly standardised surface temperature at the q grid points $x = 1, ..., q$ for observation time $t = 1, ..., n$ (over the calibration period 1901–1960). The $S_{calib}(t, y)$ data field consists of standardised observations at p stations $y = 1, ..., p$ at the same observation time $t = 1, ..., n$ for the calibration period 1901–1960. Both, the predictands and the predictors for each climatological season were transformed into Empirical Orthogonal Functions (EOFs) (Preisendorfer 1988, von Storch and Zwiers 1999). This was done to separate the dominant spatial patterns of variability, accounting for a substantial fraction of the predictors and predictands variances, from noise and irrelevant details.

$$M_{calib}(t, i) = \sum_{y=1}^{p} S_{calib}(t, y) \cdot \alpha_{yi} \tag{3.1}$$

$$N_{calib}(t, j) = \sum_{x=1}^{q} T_{calib}(t, x) \cdot \beta_{xj} \tag{3.2}$$

where $M_{calib}(t, i)$ and $N_{calib}(t, j)$ are the i-th and j-th EOF-time series, respectively, and α_{yi} and $beta_{xj}$ the i-th and j-th EOF-patterns, respectively; $i = 1, ..., p* < p$ and $j = 1, ..., q* < q$ (Luterbacher et al. 2002b).

The leading predictor data EOFs sharing 95% of total variance and the leading temperature EOFs explaining 90% of the total variability were calculated and the higher order EOFs have been discarded. A multivariate regression was then performed regressing each of the grid-point EOFs of the calibration period in turn against all the retained EOFs of the predictor data for the same period. The multivariate regression yielded an expansion of the EOF subspaces of the predictors and predictands

$$N_{calib}(t,i) = \sum_{i=1}^{p*} M_{calib}(t,i) \cdot \gamma_{ij} + Error(t,j) \tag{3.3}$$

where $j = 1, ..., q*$, where γ are the unknown regression coefficients and $Error$ is the residuum. We estimated the regression coefficients $\hat{\gamma}_{ij}$ by the usual least squares method. As we then wished to have a prediction $T_{verif}(t,x)$ and a predictor data set $S_{verif}(t,y)$ for the verification period (1961–1995), we assumed that $S_{verif}(t,y)$ is standardised by the same values as $S_{calib}(t,y)$ and calculated

$$M_{verif}(t,i) = \sum_{y=1}^{p} S_{verif}(t,y) \cdot \alpha_{yi} \tag{3.4}$$

where $i = 1, ..., p*$

$$\hat{N}_{verif}(t,j) = \sum_{i=1}^{p*} M_{verif}(t,i) \cdot \hat{\gamma}_{ij} \tag{3.5}$$

and transform the $q*$-components of the EOFs back to

$$\hat{T}_{verif}(t,x) = \sum_{j=1}^{q*} \hat{N}_{verif}(t,j) \cdot \hat{\beta}_{xj}. \tag{3.6}$$

Finally, the standardisation made on the gridded temperature fields had to be reversed in order to obtain the temperature reconstructions for the verification period 1961–1995. For the seasonal reconstructions from 1500 to 1658, the same method was applied but regressing the seasonal means of the gridpoint EOFs in turn against all the retained seasonal predictors EOFs.

Finally, the EOFs for the predictors and predictands were derived over the entire 95 years from 1901–1995 and the subsequent principal components regression analysis performed and applied to the predictor data, giving the temperature and precipitation estimates back to AD 1500.

3.2 Sea Level Pressure (SLP) and 500 hPa Geopotential Height Data

Sea level pressure (SLP) fields (5°× 5°) and 500 hPa geopotential height fields (2.5°× 2.5°) were reconstructed for the eastern North Atlantic / European area from 30°W to 40°E and 35°N to 70°N using the reconstruction method defined above (cf. section 3.1.3). The data includes gridded monthly fields back to 1659 and seasonal reconstructions for the period 1500–1658. In this study only seasonally averaged estimates are used. The monthly SLP data for the period 1901–1998 were prepared by NCEP (National Centres for Environmental Prediction, see Trenberth and Paolino 1980 for source details). This data was used as calibration and verification data for the reconstruction procedure. Missing pressure values for some months prior to 1940 were replaced by linear interpolation between adjacent grid points. The monthly 500 hPa geopotential height data for the post 1947 period, also used as verification data, was provided by the NCEP/NCAR Reanalysis Project (Kistler et al. 2001, Kalnay et al. 1996). Both SLP and 500 hPa geopotential height fields were reconstructed using temperature, precipitation and pressure predictors.

3.3 Volcanic Data

The effect of a volcanic eruption on climate is most directly related to the sulphur content of emissions that reach into the stratosphere and not to the explosivity of the eruption. Therefore it would be desirable to have a volcanic index that is proportional to the physical effect of the volcanic dust veil on climate, namely, the net radiation deficit (Robock and Free 1995). The suitable volcanic index for this type of study should be complete in its geographical and temporal coverage. A circular reasoning must be excluded (temperature anomalies after the eruption must not be used to create the index). It should not be a measure of some property of volcanic eruptions other than their stratospheric dust loading (Robock and Free 1995). Table 3.1 gives an overview on the indices of past volcanic activity, their units and data sources. In this study a compilation by Ammann et al. (2003) was used to select 16 major volcanic indices over the last 500 years. The dating of the eruptions was established using a comprehensive list of all known volcanoes and their eruptions provided by Simkin and Siebert (2003) and compared with various volcanic indices presented below.

3.3.1 Direct Evidence: Satellite and Direct Stratospheric Measurement

Advances in technology have given the scientific community a much better opportunity to characterise the climatic and atmospheric impact of volcanism. Satellite data, such as provided by the total-ozone mapping spectrometer (TOMS) unit, are available to make real-time estimates of the quantity of SO_2 injected into the stratosphere by an eruption. One specific advantage of these measurements is that they provide estimates of variability in optical depth τ, which is an important parameter needed to determine the climatic impact of an eruption (Zielinski 2000).

However, still up to the present there may be eruptions on the Southern Hemisphere not being reported. Even in December 1981 aerosols from the eruption of Nyamuragira (Democratic Republic of Congo) were observed with lidar (LIght Detection And Ranging) but were reported as mystery cloud for several years until the source was identified by re-examining the TOMS satellite record (Robock and Free 1995).

In addition to satellite data, direct stratospheric measurements of SO_4^{2-} have been undertaken, although such measurements are discontinuous both spatially and temporally (e.g. Sedlacek et al. 1983). However, direct satellite measurement started in late 1978 (Sato et al. 1993) and direct stratospheric measurements do not reach much farther back in time (Zielinski 2000). Therefore various volcanic indices were constructed to classify the different volcanic eruptions further back in time.

3.3.2 Volcanic Indices

As high quality measurements are lacking, different compilers have reconstructed volcanic indices using geological evidence, ice core profiles and the available surface radiation measurements combined with indirect measures such as reports of red sunsets in diaries and paintings. Geological methods, based on examination of the lava deposits are useful information on the total mass erupted and the date of the eruption, but provide no accurate estimates of the atmospheric sulphur loading (Robock and Free 1995). As we go further back in time the problem of missing volcanoes and their associated dust veils becomes increasingly important for all the indices (Robock and Free 1995) and the uncertainty obviously tends to increase (Sato et al. 1993).

3.3.2.1 Lamb's Dust Veil Index

The dust veil index (DVI) is the first extensive compilation of past volcanic eruptions. The DVI was specifically designed for analysing the effects of volcanoes on surface weather, on lower and upper atmospheric temperatures, and on the large-scale wind circulation (Lamb 1970). The methods used to define the DVI include historical reports of eruptions, optical phenomena, radiation measurements (since 1883), temperature information, and estimates of the total mass erupted (Robock 2000). Lamb's DVI has often been criticised (e.g. Bradley 1988) as having used climatic information in its derivation, thereby resulting in a circular reasoning if the DVI is used as an index to examine the temperature response. The DVI was calculated based only on temperature information for few eruptions between 1763 and 1882, but for several in this period it was calculated partially based on temperature information (Robock and Free 1995). Lamb used various parameters to produce an arbitrary scale with the standard being the 1883 Krakatau eruption (DVI = 1000) (Zielinski 2000). The DVI is by definition an annual average, with 40% of the volcanic loading assigned to the year of the eruption, 30% to the next year, 20% to second, and 10% to the third year after the eruption. Lamb provided a NH DVI for 1500–1982 and a SH DVI for 1890–1982. Robock and Free (1995) updated the indices for the years 1983–1995.

3.3.2.2 Mitchell Index

Mitchell (1970) produced a volcanic index based on data from Lamb for the period 1850–1968. Mitchell's index is more detailed, because Lamb excluded all volcanoes with DVI < 100 in producing his NH annual average DVI. Mitchell provided a table of the order of magnitude of total mass ejected from each volcano, which is a classification similar to the volcanic explosivity index (Robock 2000).

3.3.2.3 Volcanic Explosivity Index

The volcanic explosivity index (VEI) was developed by Newhall and Self (1982) for all known eruptions and gives a geologically based measure of the power of the volcanic explosion. Eruptions dating back as far as 12'000 years ago have been assigned to VEI values (Robertson et al. 2001). It is still being updated for present eruptions (e.g. Simkin and Siebert 2003). The VEI never was intended to be used as a tool for evaluating the climatic impact of an eruption (Zielinski 2000). It is generally accepted that the value of the VEI as an index of the effect of volcanic eruptions on climate is limited, because it is a geological measure of the explosivity and not of the sulphate input to the stratosphere (Robock and Free 1995). Newhall and Self (1982) restricted themselves to the consideration of volcanological and explicitly not atmospheric data. Since the abundance of sulphate aerosol is important in climate problems, the VEI must be combined with a compositional factor before use in climate impact studies (Newhall and Self 1982). Any agreement between climatic perturbation and VEI numbers simply reflects the greater potential for a larger eruption to have an impact on climate (Zielinski 2000).

3.3.2.4 Sato Index

Sato et al. (1993) developed an index of stratospheric aerosol optical depth for the period 1850–1990. Their index expresses the optical depth at wavelength $\lambda = 0.55$ μm. The sources of the stratospheric aerosol data differ between four periods, which have a successively improved data quality (Sato et al. 1993). In period 1 (1850–1882) they provide only very crude estimates of aerosol optical thickness based on the volume of the ejecta from major known volcanoes. During period 2 (1883–1959) measurements of solar extinction were used, but during the time of principal volcanic activity (1883–1915) the data are confined to middle-latitude NH observatories. In period 3 (1960–1978) the index is based on more widespread measurements of solar and stellar extinction and in period 4 (1979–1990) precise widespread data from satellite measurements are added (Sato et al. 1993). Robock and Free (1995) criticise that the seasonal and latitudinal distribution for the beginning of the record are uniform and offer no advantages over the DVI, but that the more recent part of the record would presumably be more accurate than the DVI and VEI. Stothers (1996) has improved the index for the period 1881–1969 by incorporating more pyrheliometric data from stations primarily in the Northern Hemisphere and historical accounts of starlight extinction, purple twilight glows, and other turbidity indicators.

3.3.2.5 Ice-core-Volcano-Index

Ice cores offer a valuable opportunity to reconstruct volcanic aerosols through the measurement of volcanic sulphate deposited on glacial ice in the years following immediately an eruption (Robertson et al. 2001). This allowed Robock and Free (1995) to develop an ice-core-volcano-index (IVI) based on ice core acidity and sulphate records. These two records, containing physical evidence of atmospheric loading, are a promising source of information on past volcanic aerosols, but contain also large non-volcanic signals (Robock and Free 1995). Eight NH and six SH ice core records for the period 1850–1995 were used and converted to equivalent optical depth units, isolating the volcanic from the background signal. The indices were adjusted to equivalent optical depth (τ) at wavelength $\lambda = 0.55$ μm and normalised to the values of Sato et al. (1993) for Krakatau in 1883 (Robock and Free 1995).

3.3.2.6 Volcanic Aerosol Index

The volcanic aerosol index VAI was developed by Robertson et al. (2001) and combines historical observations, ice core data from both Greenland and Antarctica, as well as recent satellite data. The index incorporates ice core data that were unavailable for previous reconstructions and avoids ice cores that are less well dated or strongly influenced by non-volcanic aerosols (Robertson et al. 2001). The VAI is a yearly latitude-dependent estimate of optical depth for the past 500 years. Excess sulphate (SO_4^{2-}) flux data was used from five ice cores (GISP2, GR89, and Site A in Greenland; Siple and Dyer Plateau in Antarctica). All data except for GISP2 (error less than 5 %) had been corrected for the presence of sea-salt, the primary non-volcanic component of naturally derived sulphate in the high-latitude ice core (Robertson et al. 2001). The recent background trend in the Greenland ice cores data, which was hypothesised to be the result of tropospheric anthropogenic sulphate deposition, was removed (Robertson et al. 2001). The local optical depth perturbation (τ) at the latitude of the ice cores was calculated by the following equations by Stothers (1984):

$$\tau = \sigma n l, \tag{3.7}$$

where

$$\sigma = \pi r^2 Q, \tag{3.8}$$

$$n = \frac{M}{Alm}, \tag{3.9}$$

and

$$m = \frac{4\pi r^3 \rho}{3}, \tag{3.10}$$

where σ is the mean scattering coefficient, n is the number density of aerosols, l is the vertical path length through the aerosol layer, r is the mean aerosol radius (r $\approx$ 0.3 μm, Q is a dimensionless scattering factor (characteristically $Q = 2$), M is the sulphate loading over an area A, and ρ is the mean aerosol density (characteristically 1.5 g/cm^3). The latitudinal profile was determined by estimating the pattern of elevated optical depth centred over the latitude of the eruption. A linear relationship was established between time of the year of eruption and the width of the peak of elevated optical depth. Poleward of this peak the profile was estimated as a linear trend in optical depth on either side to the poles (Robertson et al. 2001).

Despite the many advantages of the VAI, there are some limitations. First, there are probable limitations in the historical record especially of the record before 1600. The eruption frequency plot in figure 3.2 suggests that the number of volcanic eruptions reported is related to historical events (e.g. wars) and the number of potential observers (population) and therefore decreases as we go farther back in time (Robertson et al. 2001). However, the frequency of the highly explosive (VEI $\geq$ 4) eruptions shows no comparable trend for the last 400 years. Secondly, there are limitations involving the ice core contamination by tropospheric aerosols. Third, the model used to estimate stratospheric transport is based on sparse data from atmospheric bomb testing, based on the assumption that volcanic aerosols will behave similarly to bomb fallout when injected into the stratosphere. A fifth possible limitation is the possibility of a sulphate signal from a major volcanic eruption not appearing in an ice core (Robertson et al. 2001).

3.3.3 Dating of Volcanic Eruptions

The major volcanic eruptions of the past 250 years have each drawn attention (Robock and Free 1995) and are therefore well described and dated in historical documents. Minor eruptions, eruptions in less populated areas and especially eruptions before the 18th century are not well dated. Simkin and Siebert (1994) provide a comprehensive list of all known volca-

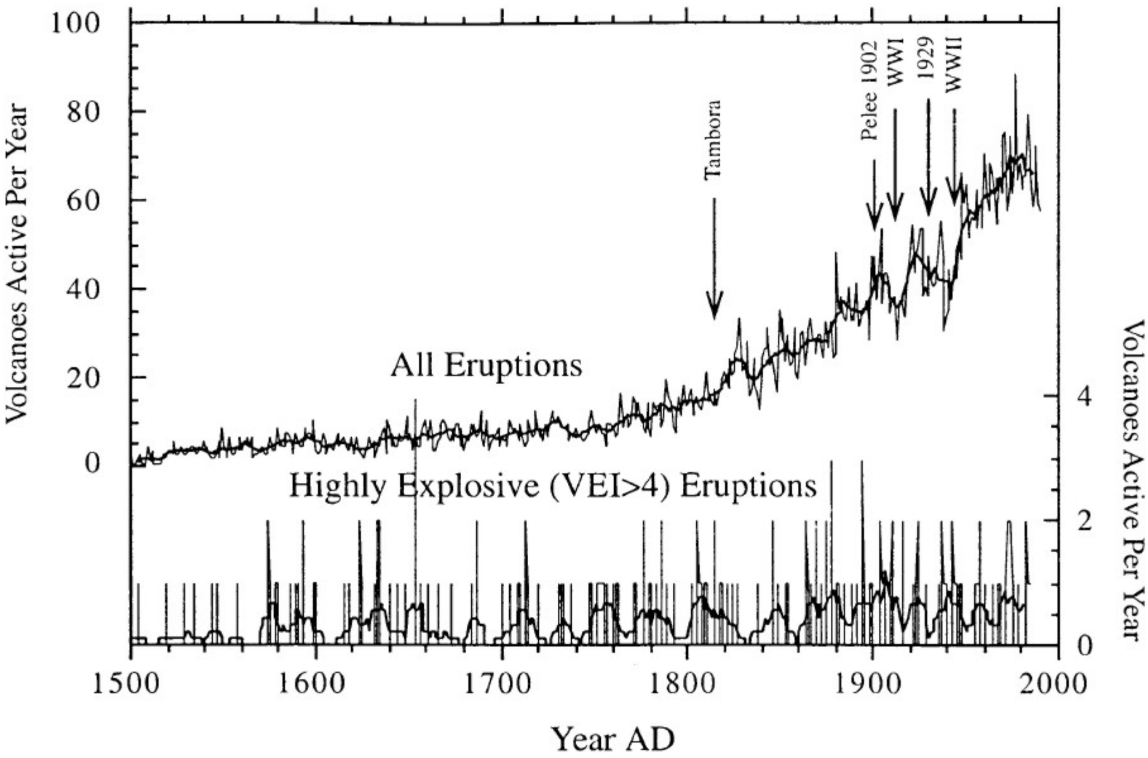

Figure 3.2: *Frequency of volcanic eruptions reported per year for the last 500 years (Robertson et al. 2001, after Simkin and Siebert 1994). The top plot shows total number of volcanic eruptions reported per year with the 9-year running mean. The bottom plot shows only highly explosive (VEI ≥ 4) volcanic eruptions with the 9-year running mean.*

Table 3.1: *Indices of past volcanic activity (after Robock 2000)*

Name	Units	Data source	Reference
Dust veil index (DVI)	Krakatau = 1000	Sapper (1917, 1927), sunsets, eruption, and radiation observations	Lamb (1970, 1977, 1983)
Mitchell Index	aerosol mass	based on Lamb (1970)	Mitchell (1970)
Volcanic explosivity index (VEI)	Krakatau = 6	explosivity, from geologic and historical reports	Newhall and Self (1982) and (Simkin and Siebert 1994)
Sato Index	τ ($\lambda = 0.55$ mm)	Mitchell (1970), radiation and satellite observations	Sato et al. (1993)
Ice core volcanic index (IVI)	τ ($\lambda = 0.55$ mm)	average of ice core acidity or sulphate measurements	Robock and Mao (1995, 1996)
Volcanic aerosol index (VAI)	τ ($\lambda = 0.55$ mm)	historical observations, ice core data, satellite data	Robertson et al. (2001)
Binary Volcanic Forcing Data Set	binary (0 or 1)	IVI, recent ice core sulphate data	Ammann et al. (2003)

noes and their eruptions. An updated electronic version is provided by the Global Volcanism Program, Smithsonian Institution (Simkin and Siebert 2003, http://www.volcano.si.edu/).

The selection of volcanic eruptions used in this study is based on a compilation by Ammann et al. (2003). They used the Ice core sulphate-based Volcanic Index (IVI) of Robock and Free (1996) complemented with recent ice core sulphate data to analyse the distribution of volcanic eruption events over the last 600 years. The compilation concentrates on the climatically important eruptions in the tropics (30°N–30°S), using corresponding sulphate signals in both polar ice caps as the selection criterion. In the case of tropical eruptions, the aerosol is transported around the globe and commonly spread poleward into both hemispheres. Unfortunately, due to local depositional effects, up to a third of the volcanic event signals can be missing in a single core (Ammann et al. 2003). Therefore, to obtain a complete volcanic record, a large number of well-dated ice cores have to be compiled, and the sulphate spikes have to be inter-compared (Robock and Free 1996). For a large tropical eruption with a significant sulphate component, a signal in both polar ice caps is to be expected (Ammann et al. 2003). However, the aerosol transport for individual events can in some cases be strongly biased towards one hemisphere and one cannot exclude that some peaks in both Greenland and Antarctica could represent two independent events in the higher latitudes. Nevertheless, multiple ice core data in conjunction with a recorded tropical event in the Smithsonian Catalogue (Simkin and Siebert 1994) lend confidence to the compilation by Ammann et al. (2003). For the 20th century, where the sulphate signal is disturbed by anthropogenic emission, observed atmospheric perturbation data was also used. Each year from 1400 to 1998 was coded by a one if sulphate spikes were recognised in any one or more cores in both hemispheres, and zero otherwise. This results in a binary tropical volcanic data set including no information on the magnitude of individual events. A list of the identified individual volcanic eruptions is provided as supplementary data (figure A.1). I use a selection of this eruption list (figure 3.2) based on information about the magnitude and reliability of the timing of the volcanic eruptions (C. Ammann, personal communication, February 2003). The geographical location of the selected volcanoes is illustrated in figure 3.3 and its influence on the climatic response within Europe is discussed in section 5.1.5. The timing of the eruptions and their geological magnitude is illustrated in figure 3.4.

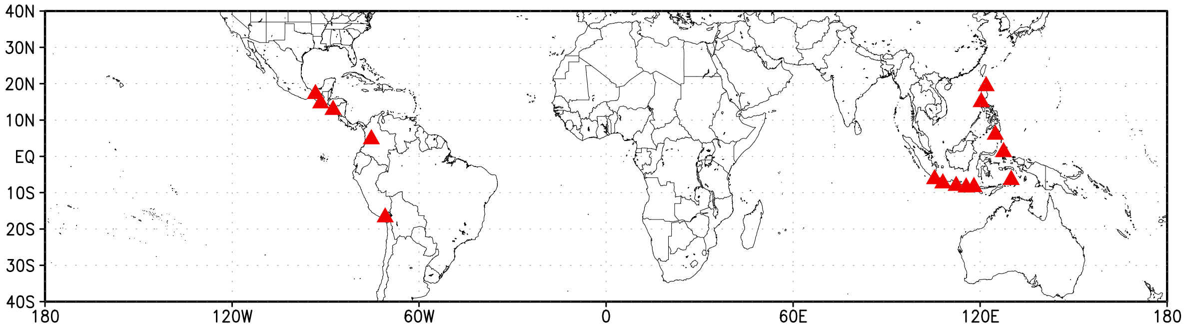

Figure 3.3: *Geographical location of the different volcanoes in table 3.2, excluding the unknown eruption 1809.*

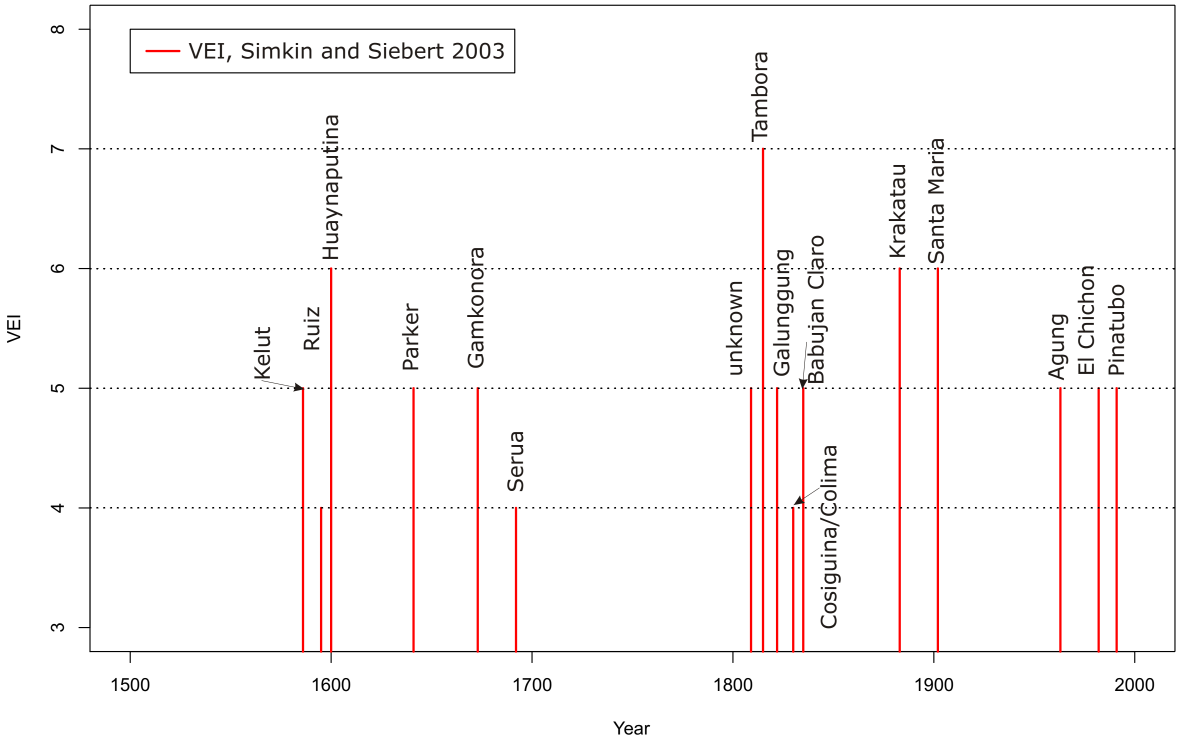

Figure 3.4: *Dating and magnitude of the different volcanic eruptions in table 3.2, excluding the unknown eruption 1809. The geological magnitude of the eruptions is indicated with the volcanic explosivity index (VEI) (Simkin and Siebert 2003, Newhall and Self 1982).*

Table 3.2: *16 selected major tropical volcanic eruptions of the period 1500–1998 used in this study. Year and month (if known) of the start and end of the eruption (Simkin and Siebert 2003) are indicated in column three to four. The dating of the main eruption, estimated by Ammann et al. (2003), is given in column four. Column eight and nine indicate the volcanic indices VEI (Simkin and Siebert 2003) and IVI (Robock and Free 1995) and column ten the season, used as first season after the corresponding eruption in this study.*

Volcano	Country	Start	End	Ammann	Latitude	Longitude	VEI	IVI	first season
Kelut	Indonesia	1586		1586 07	7.93°S	112.308°E	5?	0.25	au 1586
Ruiz	Colombia	1595 03		1595 10	4.895°N	75.323°W	4	0.25	wi 1596
Huaynaputina	Peru	1600 02	1600 03	1600 04	16.608°S	70.85°W	6	0.5	su 1600
Parker	Philippines	1640 12	1641 01	1641 01	6.12°N	124.892°E	5?	0.4	sp 1641
Gamkonora	Indonesia	1673 05		1673 04	1.375°N	127.52°E	5?	0.2	au 1673
Serua?	Indonesia	1693 06	1693 07	1692 10	6.30°S	130.00°E	4?	0.2	wi 1693
unknown		1809		1809 01				0.75	sp 1809
Tambora	Indonesia	1812	1815 07	1815 04	8.25°S	118.00°E	7	1	su 1815
Galunggung	Indonesia	1822 10	1822 12	1822 10	7.25°S	108.05°E	5	0.2	wi 1823
Babujan Claro	Philippines	1831		1830 07	19.523°N	121.940°E	4?	0.3	au 1830
Cosiguina /Colima	Nicaragua	1835 01	1835 01	1835 01	12.98°N	87.57°W	5	0.3	sp 1835
Krakatau	Indonesia	1883 05	1883 10	1883 08	6.10°S	105.42°E	6	0.4	au 1883
Santa Maria	Guatemala	1902 10	1902 11	1902 10	14.76°N	91.55°W	6?	0.25	wi 1903
Agung	Indonesia	1963 02	1964 01	1963 03	8.342°S	115.508°E	5	0.2	au 1963
El Chichon	Mexico	1982 03	1982 09	1982 05	17.360°N	93.228°W	5	0.2	au 1982
Pinatubo	Philippines	1991 04	1991 09	1991 06	15.13°N	120.35°E	5	0.3	au 1991

Chapter 4

Methods

In order to understand the volcanic forcing on climate it is desirable to determine the difference between an unforced climate state and the typical climatic response to major volcanic eruptions. The methodical details used for this study are presented in the following sections based on the publications by von Storch and Zwiers (1999), Wilks (1995) and Yarnal (1992).

4.1 Composite Analysis or Superposed Epoch Analysis (SEA)

To investigate the mean impact of selected major volcanic eruptions I make use of the composite analysis (compositing or composite analysis is virtually equal to superposed epoch analysis (SEA) (von Storch and Zwiers 1999); however in papers about the volcano-climate connection the method is often referred to as SEA). SEA has been widely used in studies of the effects of volcanoes on climate (Sear et al. 1987, Bradley 1988, Portman and Gutzler 1996 and Kelly et al. 1996). Compositing is a very simple concept and easy to apply. Composites are "average maps" of specific situations. The investigator selects a number of maps that satisfy an important criterion (e.g. post-eruption period) and averages them. Compositing is probably one of the most frequently used methods in synoptic climatology. It applies a so called environment-to-classification approach to synoptic climatology (Yarnal 1992). According to this approach the atmospheric circulation is classified from knowledge of the surface environment. Therefore, the classification criteria are independent of the atmospheric circulation, so there is no a priori choice of synoptic types prejudicing the results (Yarnal 1992). Despite all its advantages, there are problems with compositing (Yarnal 1992). The basic idea with composites is to construct typical states of climate conditional on the value of a criterion. It achieves this goal in the sense that we obtain estimates of the mean state. However, there may be considerable variability around each composite, and the composite may not be representative of the typical state (von Storch and Zwiers 1999). Thus, compositing can average disparate settings, inducing a false impression of the typical situation associated with a given criterion (Yarnal 1992). In this study I will calculate the standard deviations and test the robustness of composites by considering each single event in order to reduce this problem.

Compositing and SEA in studies on the volcano-climate connection are used to reduce noise in a data set and to indicate the mean response following specific events (Bradley 1988). The superposition, or compositing, clarifies the volcanic signal by averaging out features not common to the individual events (Bradley 1988). In this study the data is averaged for every climatological season (winter=DJF, spring=MAM, summer=JJA, autumn=SON) to allow a specific investigation of the different volcanic impact on every season. Taking the eruption as a starting date, data for the proceeding seasons were averaged to produce the composite volcanic signals for each season. The first season after each eruption was defined as a key season. To reveal the short-term response and avoid the effects of longer-term climatic changes (Bradley 1988) the data are expressed as seasonal anomalies with respect to the mean value of the same season during the five years preceding the volcanic eruption (e.g. for Pinatubo eruption 1991: autumn temperature 1991 with respect to the mean autumn temperature 1986–1990). The same procedure was used by Kelly and Sear (1984) taking a one year period, Bradley (1988) a 3 year period and Kelly et al. (1996) taking a 5 year period prior to the key date. Problems may arise if the key date falls in the middle of a period when a strong upward or downward trend is occurring. The calculation of the composite temperature field of the first year following 16 selected eruptions is illustrated in the following equation:

$$\overrightarrow{T}_{comp,s} = \frac{1}{16} \sum_{k=v_1}^{v_{16}} (\overrightarrow{T}_{k,s} - \frac{1}{5} \sum_{j=k-5}^{k-1} \overrightarrow{T}_{j,s}), \tag{4.1}$$

where $\overrightarrow{T}_{comp,s}$ is the composite temperature field for the climatological season s, v_1–v_{16} the first year after the 16 selected volcanic eruptions, $\overrightarrow{T}_{k,s}$ the temperature field in the first season after an eruption and $\overrightarrow{T}_{j,s}$ the field of the five years before an eruption. The anomalies were calculated for every grid point and every season during the five years after the selected eruptions. For each grid point in the composite field the standard deviation was calculated.

4.2 Significance Testing

I tested the statistical significance of the composite anomaly field for every gridpoint using the following null hypothesis: $H_0 : \mu_{T_{comp}} = \mu_{T_{ref}}$. An accepted null hypothesis would mean that the temperature after volcanic eruptions at the grid point does not differ significantly from the reference period including non-volcanic years. I define the non-volcanic years as all years,

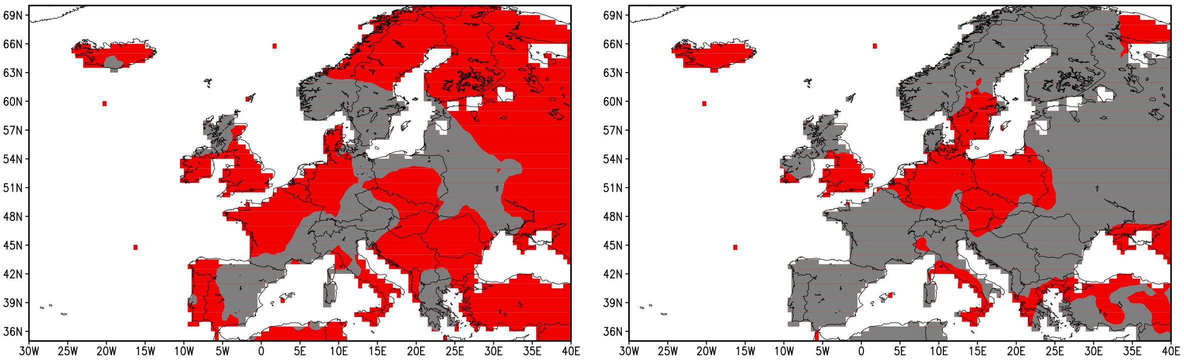

Figure 4.1: *Shapiro Wilk normality test for summer (left panel) and winter (right panel) anomalies of reconstructed temperature 1500–1998 for each gridpoint. Gridpoints with a normal distribution following the Shapiro Wilk test at the 99% confidence level (p-value ≤ 0.01) are marked with red colour, whereas non normally distributed grid points are marked with grey colour.*

for which reconstructions are available except eight years following each eruption. Thus, I exclude all years, whose anomaly could be directly or indirectly influenced by volcanic forcing. The calculation of the reference period composite field is given by the following equation:

$$\overrightarrow{T}_{ref,s} = \frac{1}{n}(\sum_{k=w_1}^{w_n}(\overrightarrow{T}_{k,s} - \frac{1}{5}\sum_{j=k-5}^{k-1}\overrightarrow{T}_{j,s})), \tag{4.2}$$

where w_1–w_n are the non-volcanic years during the period 1505–1998 and n is the number of non-volcanic years and s the climatological season.

In order to determine the appropriate statistical test, the distribution of $T_{ref,s}$ was tested for normality at every grid point using a Shapiro Wilk Normality test (Shapiro and Wilk 1965). The Shapiro Wilk test, proposed in 1965, calculates a W statistic that tests whether a random sample, x_1, x_2, ..., x_n comes from a normal distribution. This test has done very well in comparison studies with other goodness of fit tests. The W statistic is calculated as follows:

$$W = \frac{(\sum_{i=1}^{n} a_i x_{(i)})^2}{\sum_{i=1}^{n}(x_i - \overline{x})^2}, \tag{4.3}$$

where the x_i are the ordered sample values (x_1 is the smallest) and the a_i are constants generated from the means, variances and covariances of the order statistics of a sample of size n from a normal distribution (Shapiro and Wilk 1965). I tested the summer and winter temperature for normality at every grid point over all non-volcanic years. The results for summer (left panel) and winter (right panel) temperature are illustrated in figure 4.1.

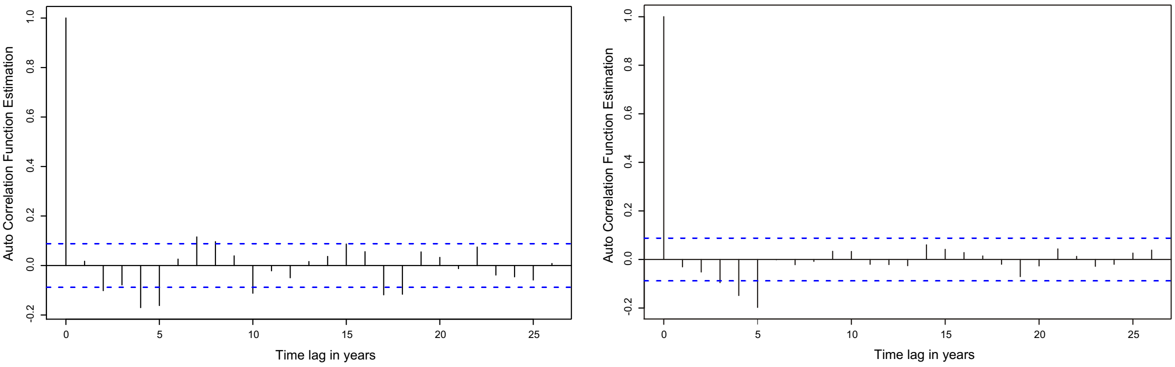

Figure 4.2: *Auto correlation function estimation for summer (left panel) and winter (right panel) temperature series.*

Figure 4.1 reveals a different and nearly opposite pattern of normally distributed gridpoints during summer and winter. However, it is apparent that on a prominent part of the gridpoints the temperature anomalies are not normally distributed in time. Since data sets, which are not normally distributed, tend to indicate statistical significance erroneously, I decided to use the non-parametric Mann-Whitney test, which is equivalent to the Wilcoxon rank-sum test, to estimate the statistical significance. Thereby I minimise the possibility of obtaining significant areas, which are not truly significant.

The Mann-Whitney test is a classical nonparametric test for the difference between two data samples. The test is resistant, meaning that a few "wild" data values that would completely invalidate the student's t test, will have little or no influence on the test decision. It is robust in the sense that even if all assumptions required for the t test are met, the rank-sum test is almost as good as the t test (Wilks 1995). The two samples have to be both serially independent and unpaired. In this case the samples are unpaired and the volcanic years are not serially correlated. For the sample including non-volcanic years I estimated auto correlation functions illustrated in figure 4.2. There is a prominent negative auto correlation at a lag of five, respectively four years. Yet I still do no think that this will influence the test decision considerably.

An accepted null hypothesis of the Mann-Whitney test would express that the two samples have the same location (cf. above) and are from the same distribution. Thus there would be $n = n_1 + n_2$ observations making up a single empirical distribution. The rank-sum test statistic is a function not of the data values themselves, but of their ranks within the n observations (Wilks 1995). Define R_1 as the sum of the ranks held by the members of sample 1 in this pooled distribution and R_2 as the sum of the ranks held by the members of sample 2. If H_0 is true and the two samples have the same location, then R_1/n_1 and R_2/n_2 are similar in magnitude. The Mann-Whitney U statistic is given by

$$U_1 = R_1 - \frac{n_1}{2}(n_1 + 1). \tag{4.4}$$

The added flexibility of the Mann-Whitney test compared with the t test results in a slightly reduced efficiency when the observations are normally distributed. The t test is able to achieve the same power as the Mann-Whitney test using only 95.5% of the observations needed by the latter (von Storch and Zwiers 1999).

4.3 Monte Carlo Resampling

In a second step I used a permutation method, which is suitable to determine the statistical significance of both the area averaged and the field composite climatic response. The method is based on Adams et al. (2003), where it was used to examine the volcano - El Niño hypothesis. For each event in the eruption list, 10 specific seasons (e.g. winters) were entered into a matrix corresponding five pre- and five post-eruption seasons. This provides an interval that spans a reasonable duration of response to the forcing (about five years). This ten year interval constitutes the width dimension of the composite matrix, while the length of the composite matrix is equal to the number of eruptions used (i.e. sixteen). Each composite matrix is centred by removal of the mean across its width (Adams et al. 2003). The significance of the composite responses is established from a Monte Carlo resampling procedure based on an ensemble of (10'000) random surrogates that are derived from permutation of the full composite matrices. Distributions for each of the years of the composite response are generated from random reshuffling of the columns for each eruption event (i.e. for each row) in the composite matrix. Each eruption year contributing to the composite receives equal weight in determining the distributions. I resample from the eruption matrix itself, rather than from the entire data set. This approach preserves the actual distribution of the data contributing to the eruption matrix, but simply destroys any preferred temporal ordering between the pre-eruption and post-eruption intervals (Adams et al. 2003). Thereby I achieve a good representation of the null hypothesis of no post-eruption influence. The resulting composite distributions of the random surrogates are used to determine the statistical significance of the actual composite responses by simply comparing with the 0.5%, 2.5%, 97.5% and 99.5% quantiles.

4.4 Removing Non-Volcanic Components

Robock and Mao (1995) tried to extract the volcanic signal by removing the two principal non-volcanic components low-frequency variations and the El Niño Southern Oscillation

(ENSO) signal. Volcanic eruptions cause basically short-term temperature signals, whereas low-frequency (timescale larger than 10 years) variations may be caused by internal oscillations, greenhouse gases, tropospheric aerosols and solar variations (Robock and Mao 1995). Robock and Mao (1995) used high-pass filtering (Duchon 1979) for every gridpoint to remove the low-frequency variations with periods longer than 10 years. The El Niño Southern Oscillation is a result of complex air-sea interactions, which cause large Sea Surface Temperature (SST) variations and interannual fluctuations in climate. The ENSO is associated with a periodic (3–7 year timescale) warming (El Niño) and cooling (La Niña) of the eastern and central tropical Pacific Ocean surface that influences global-scale climate (Adams et al. 2003). In recent history, some major volcanic eruptions have happened around El Niño events, with most obvious cases being Agung 1963, El Chichon 1982, and Pinatubo 1991 (Robock and Mao 1995). Some publications even suggested and discussed a causal connection between volcanic eruptions and El Niño events. Since the climatic response to ENSO is of the same amplitude and timescales as volcanic responses it would be desirable to separate them in order to examine the volcanic signal. Robock and Mao (1995) established a linear regression relationship between high-frequency surface temperature anomalies and the (Southern Oscillation Index) SOI series. Using this relationship they removed the ENSO signals from the high frequency surface temperature variations.

In this study no data was removed or filtered. There are various methodological problems in removing the two non-volcanic components. Errors in the ENSO signal, which is removed, may well lead to more confusion in interpreting results than leaving the signal in the data set (Kelly et al. 1996). It is impossible to remove the ENSO signal completely by using a linear regression. The linear relationship between SOI and temperature is not simple and has specific regional and seasonal patterns, with the highest correlations at different lags in different locations (Robock and Mao 1995). There is a nonlinear component as well for some seasons and regions, which is dependent at least on the type or strength of the event (Robock and Mao 1995). Moreover, the SOI is not the optimal measure of ENSO, the SST anomaly pattern. There is a reconstruction of seasonal SOI based on Chinese documentary records (Song 1998). However, its reliability is decreasing quickly in the earlier part of the record. Hence I did not remove the ENSO signal and will account for the ENSO effect when interpreting the results.

The data was not filtered to avoid any loss of information in the data. By removing all low-frequencies variations, the possibility of single or multiple eruptions causing long-term variations is a priori excluded. The detailed origin of the different frequencies in the data is poorly known.

Chapter 5

Results

In this chapter selected results are presented including the area-averaged climatic response to volcanic eruptions and the composite anomaly fields following selected eruptions over the past 500 years. The chapter is subdivided in sections corresponding to the different climatic parameters temperature, precipitation, SLP, 500 hPa geopotential height. I emphasise on the summer and winter temperature as the volcanic impact on these seasons seems to be most distinct.

5.1 Temperature Response to Volcanic Eruptions

5.1.1 Mean Temperature Response

A simple approach to investigate the volcano-climate connection is to simply compare reconstructed mean annual temperature with a compilation of major volcanic eruptions. Figure 5.1 shows the annual mean temperature reconstructed by Luterbacher et al. (2003) averaged for the North Atlantic / European region and the volcanic explosivity index (VEI) of major volcanic eruptions. No general volcanic signal (e.g. cooling after every eruption) in the temperature data set can be observed. It is obvious that the temperature is influenced by various different forcings apart from the volcanic forcing. However, some major volcanic eruptions such as Parker 1640 and Tambora 1815 appear to be followed by a drop of the annual mean temperature, which does not necessarily have to be causally related to the volcanic eruption. Some periods of enhanced volcanic activity (1580–1600, 1815–1840) are accompanied by cooling of the 9-year running mean temperature, whereas others (1890–1935) occur simultaneously with a warming. In summary, it may be said that this simple method allows no general statement on the volcanic signal in the temperature record. This can be due to the complexity of the connection between different forcings and temperature or due to the fact

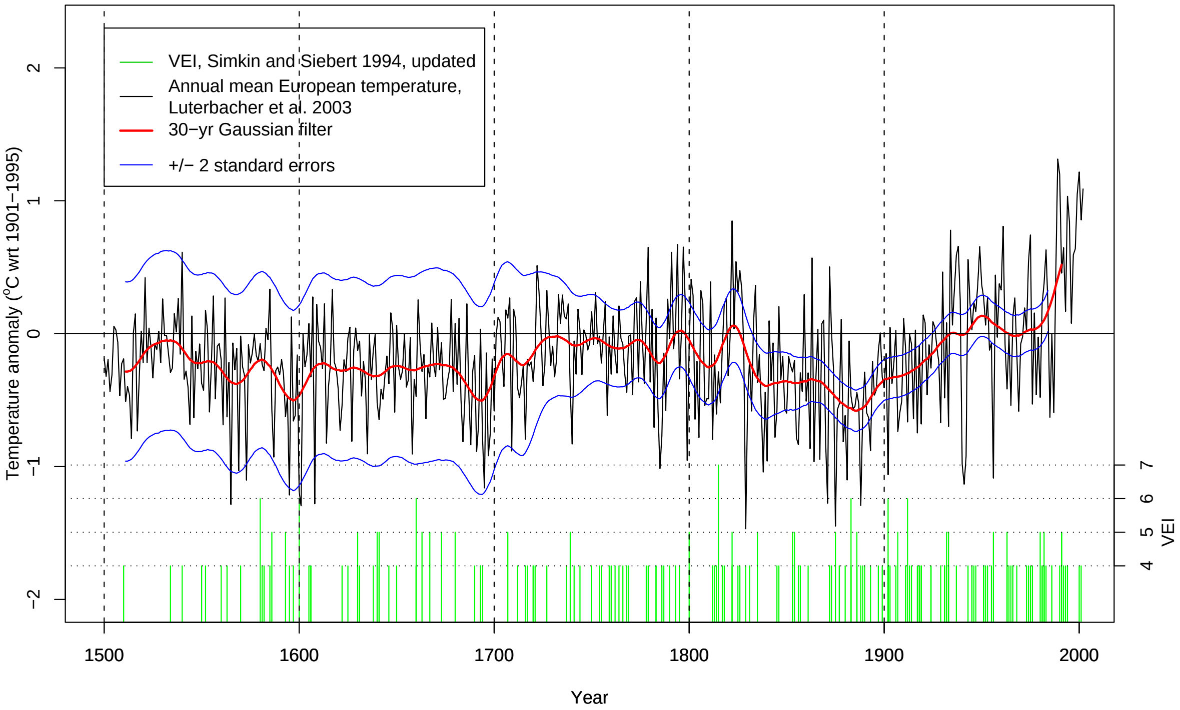

Figure 5.1: *Annual mean temperature for the European land regions (wrt 1901–1995) reconstructed by Luterbacher et al. (2003) (black line), 30 year low-pass filtered time series (red line) and 2 standard errors (SE) of the reconstructions (blue lines). The green bars mark major volcanic eruptions (VEI ≥ 4) (Simkin and Siebert 2003, Newhall and Self 1982).*

that opposite temperature signal in different seasons can compensate for each other. In order to investigate the seasonal temperature effect I compared summer and winter temperature separately with the temporally continuous volcanic aerosol index (VAI) (cf. 3.3.2.6) in figure 5.2.

Looking at specific volcanic events in figure 5.2 a much more consistent signal in the summer and winter temperature can be observed than in the annual mean temperature in figure 5.1. The volcanic events 1586, 1595, 1600, 1673, 1692, 1809, 1815, 1831, 1835, 1883, 1902, 1963 are all followed by a distinct cooling of the summer temperature for 1–2 years. The winter temperature curve reveals a trend to warming temperature during 1–2 winters following the 1595, 1641, 1692, 1815, 1883, 1963, 1982, 1991 eruptions. However, it must be noticed that these trends do not necessarily have to be connected to the volcanic signal.

5.1.2 Composite Temperature Anomaly

In order to get extended insight into the spatial and seasonal variability of the climatic response to volcanic eruptions, the composite temperature anomaly fields are presented in this section.

The composite temperature anomaly field of the first summer (i.e. between zero to eleven months after an eruption depending on the date of the eruption) following 16 major tropical eruptions (figure 5.3, upper left panel) shows a homogenous pattern of slightly negative temperature anomalies (0.5–1°C) over most of the European land areas. The cooling is significant at the 95% level (calculated by the Mann-Whitney test described in 4.2) over three minor regions in the western Mediterranean, northern Scandinavia and southern Iceland. The anomaly field for the second summer (figure 5.3, upper right panel) reveals significant cooling in most parts of Europe. The negative temperature anomaly are especially pronounced over Scandinavia, the Baltic, western Russia, northern Central Europe and down to southern France with a maximum cooling effect (up to 2°C) in Central Sweden and the southern Baltic. The negative anomalies are highly significant at a 99% level over most of Northern and parts of Central Europe, and significant at a 95% level over France, Spain and various Central European Countries. Over the Mediterranean no distinct effect can be noticed.

Figure 5.3 (lower left panel) reveals a spatial difference in the temperature response to volcanic eruptions in the first winter following tropical eruptions between Northern and Southern Europe. A warming up to 1.5°C occurs in the northern parts of Europe and a weak cooling in the southern parts. The signal is significant over a small area in northern Spain. Figure 5.3 (lower right panel) depicts the composite temperature pattern in the second winter after the eruptions indicating a prominent warming over Northern Europe. The positive temperature anomalies are most pronounced (up to more than 2°C) and highly significant over Scandinavia,

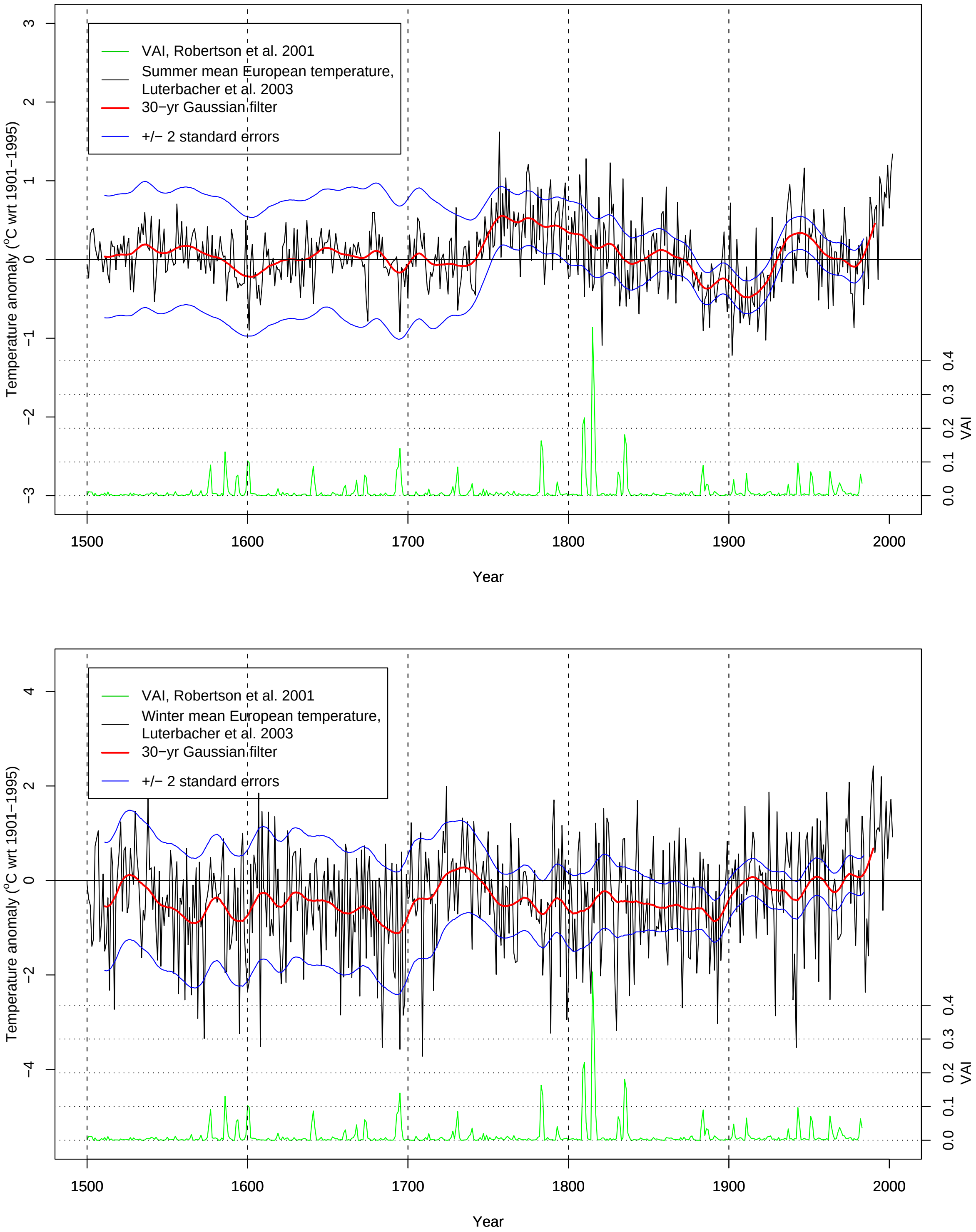

Figure 5.2: *Seasonal summer (upper panel) and winter (lower panel) mean temperature for the European land regions (wrt 1901–1995) reconstructed by Luterbacher et al. (2003) (black line), 30 year low-pass filtered time series (red line) and 2 standard errors (SE) of the reconstructions (blue lines). The green line marks the zonally averaged Volcanic Aerosol Index (VAI) for 35° N to 70° N (Robertson et al. 2001).*

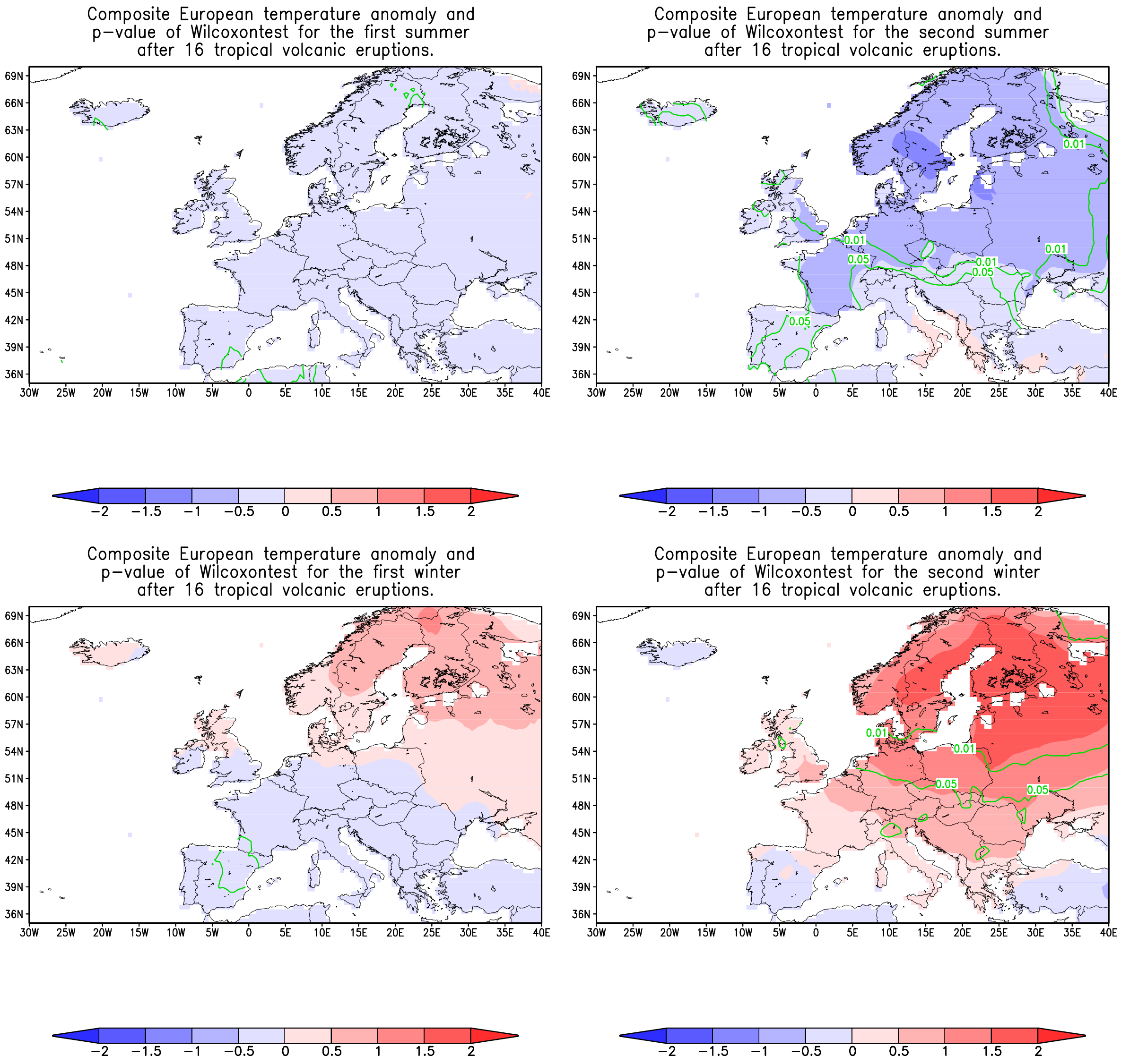

Composite European temperature anomaly and p−value of Wilcoxontest for the first summer after 16 tropical volcanic eruptions.

Composite European temperature anomaly and p−value of Wilcoxontest for the second summer after 16 tropical volcanic eruptions.

Composite European temperature anomaly and p−value of Wilcoxontest for the first winter after 16 tropical volcanic eruptions.

Composite European temperature anomaly and p−value of Wilcoxontest for the second winter after 16 tropical volcanic eruptions.

Figure 5.3: *Composite European land surface temperature anomaly field (°C, shaded) of the first (upper left panel) and second summer (upper right panel) and first (lower left panel) and second winter (lower right panel) following 16 selected major volcanic eruptions during the period 1500–1998. The green contours mark the statistical significance as p-values (representing 95% and 99% confidence level) of the Mann-Whitney Rank Sum Test.*

the Baltic and western Russia. The warming pattern extends south to the Mediterranean. Remarkable exceptions with slightly cooler conditions can be found over Iceland, the Iberian Peninsula and Turkey.

Figure 5.4 displays the composite temperature anomaly for the first and second spring and autumn. The climatic signal in the second spring and autumn is less pronounced than in the second summer and winter. During the first spring slightly positive anomalies can be observed in Western Europe and slightly negative anomalies in Eastern Europe. In the second spring a homogenous pattern of negative anomalies 0–0.5°C extends all over Europe. In the first autumn a warming pattern similar to the first winter can be observed, whereas the temperature field of the second autumn dominated by negative anomalies resembles more the second summer pattern (figure 5.3, upper right panel).

5.1.3 Comparison of Eruption Events

The composite temperature anomaly displays a mean state, which may not be representative of the typical state because of considerable variability (cf. chapter 4.1). In order to examine if the composite field represents the typical state, each of the 16 second summer anomaly fields are displayed and compared in figure 5.5. It is apparent that all composite fields show a pronounced pattern of negative anomalies, except for the post-eruption summer of Santa Maria 1902, where the cooling is restricted to north-eastern Europe. The magnitude of the cooling varies between the different eruptions and does not seem to correlate with the geological magnitude of the eruption (table 5.1). The composite temperature field for the Babujan Claro eruption 1830 shows the most distinct negative temperature anomalies up to more than 2.5°C, whereas the anomalies after Huaynaputina 1600, Parker 1641 and Galunggung 1822 are of smaller scale. The geographical location of the maximum negative anomalies is highly variable. Regarding the direction of the temperature gradient, there seem to be two categories of anomaly fields. Some composite fields show a maximum cooling in Western Europe with a positive temperature gradient to the East (e. g. Kelut 1586, Ruiz 1595, Parker 1641, Gamkonora 1673 and Tambora 1815). In other fields the maximum negative anomaly is located over north-eastern Europe with increasing temperatures to the south or southeast (e. g. Serua 1692, Galunggung 1822, Babujan Claro 1830, Krakatau 1883, Pinatubo 1991). There are few composite fields, which can hardly be classified.

To sum up it may be said that the composite field for the second summer following the 16 eruptions in figure 5.3 (upper right panel) represents a typical state in the sense that it illustrates the general summer cooling trend in Northern, Western, Eastern and Central Europe. Every temperature field in figure 5.5 shows negative anomalies over middle and southern Scandinavia and the Baltic, where the maximum negative anomaly in the composite

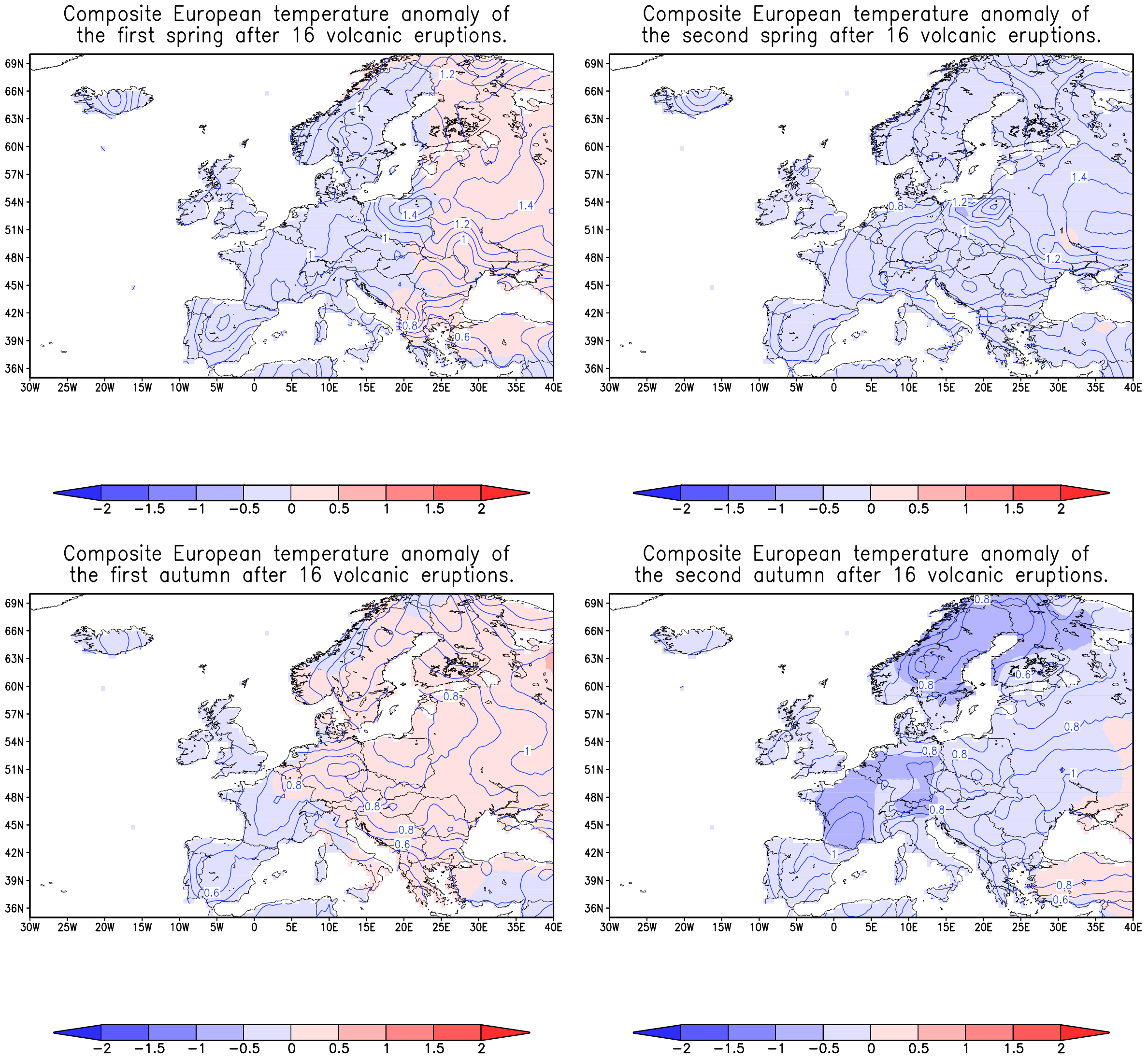

Figure 5.4: *Composite European land surface temperature anomaly field (°C, shaded) of the first (upper left panel) and second spring (upper right panel) and first (lower left panel) and second autumn (lower right panel) following 16 selected major volcanic eruptions during the period 1500–1998. The blue contours mark the standard deviations.*

field is located. Over the Mediterranean no tendency to warmer or colder conditions can be observed.

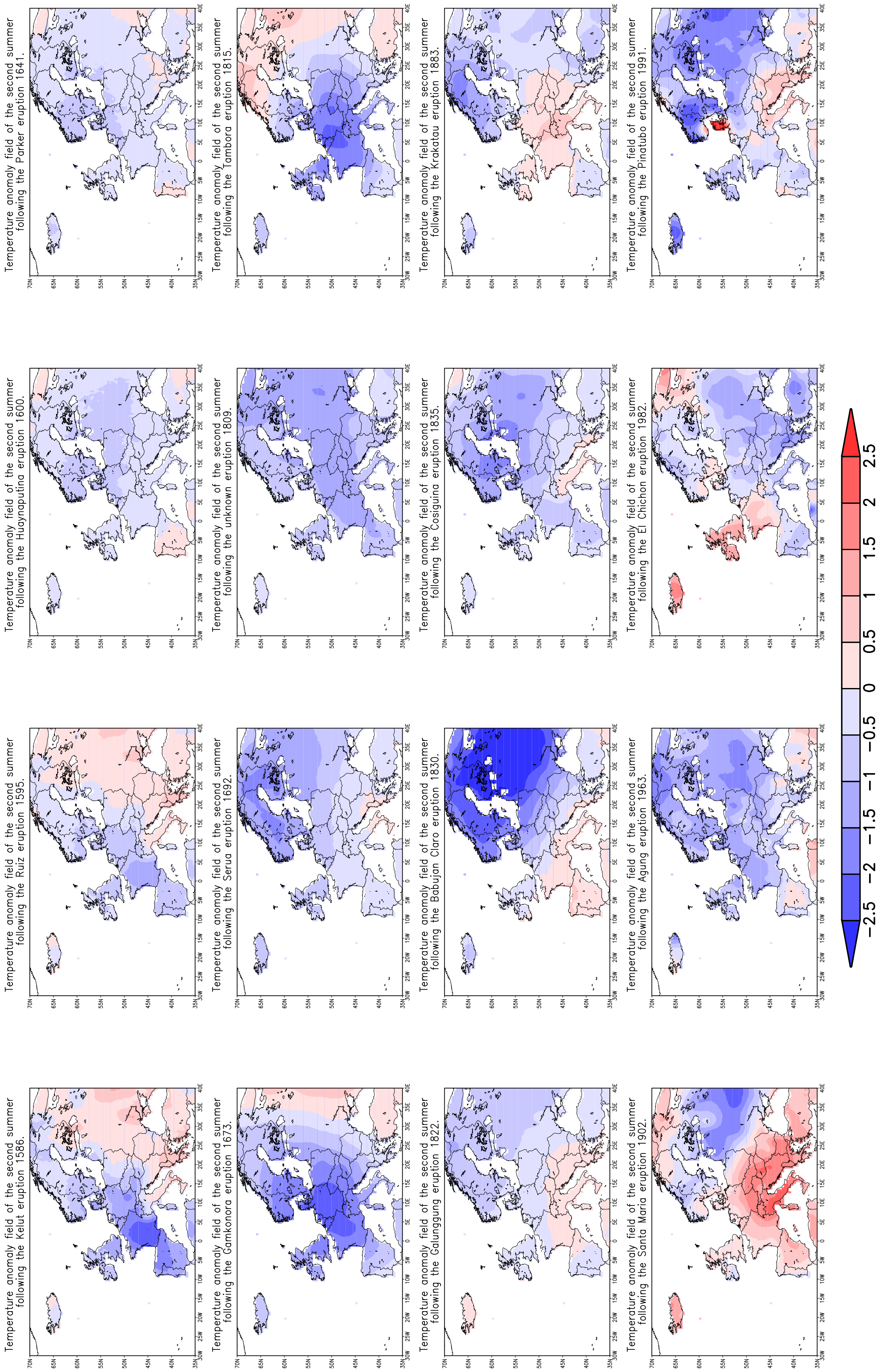
Temperature anomaly field of the second summer following the Kelut eruption 1586.

Temperature anomaly field of the second summer following the Ruiz eruption 1595.

Temperature anomaly field of the second summer following the Huaynaputina eruption 1600.

Temperature anomaly field of the second summer following the Parker eruption 1641.

Temperature anomaly field of the second summer following the Gamkonora eruption 1673.

Temperature anomaly field of the second summer following the Serua eruption 1692.

Temperature anomaly field of the second summer following the unknown eruption 1809.

Temperature anomaly field of the second summer following the Tambora eruption 1815.

Temperature anomaly field of the second summer following the Galunggung eruption 1822.

Temperature anomaly field of the second summer following the Babujan Claro eruption 1830.

Temperature anomaly field of the second summer following the Cosiguina eruption 1835.

Temperature anomaly field of the second summer following the Krakatau eruption 1883.

Temperature anomaly field of the second summer following the Santa Maria eruption 1902.

Temperature anomaly field of the second summer following the Agung eruption 1963.

Temperature anomaly field of the second summer following the El Chichon eruption 1982.

Temperature anomaly field of the second summer following the Pinatubo eruption 1991.

Figure 5.5: *European land surface temperature anomaly field (°C, shaded) of the second summer following each of the 16 selected major volcanic eruptions averaged in figure 5.3.*

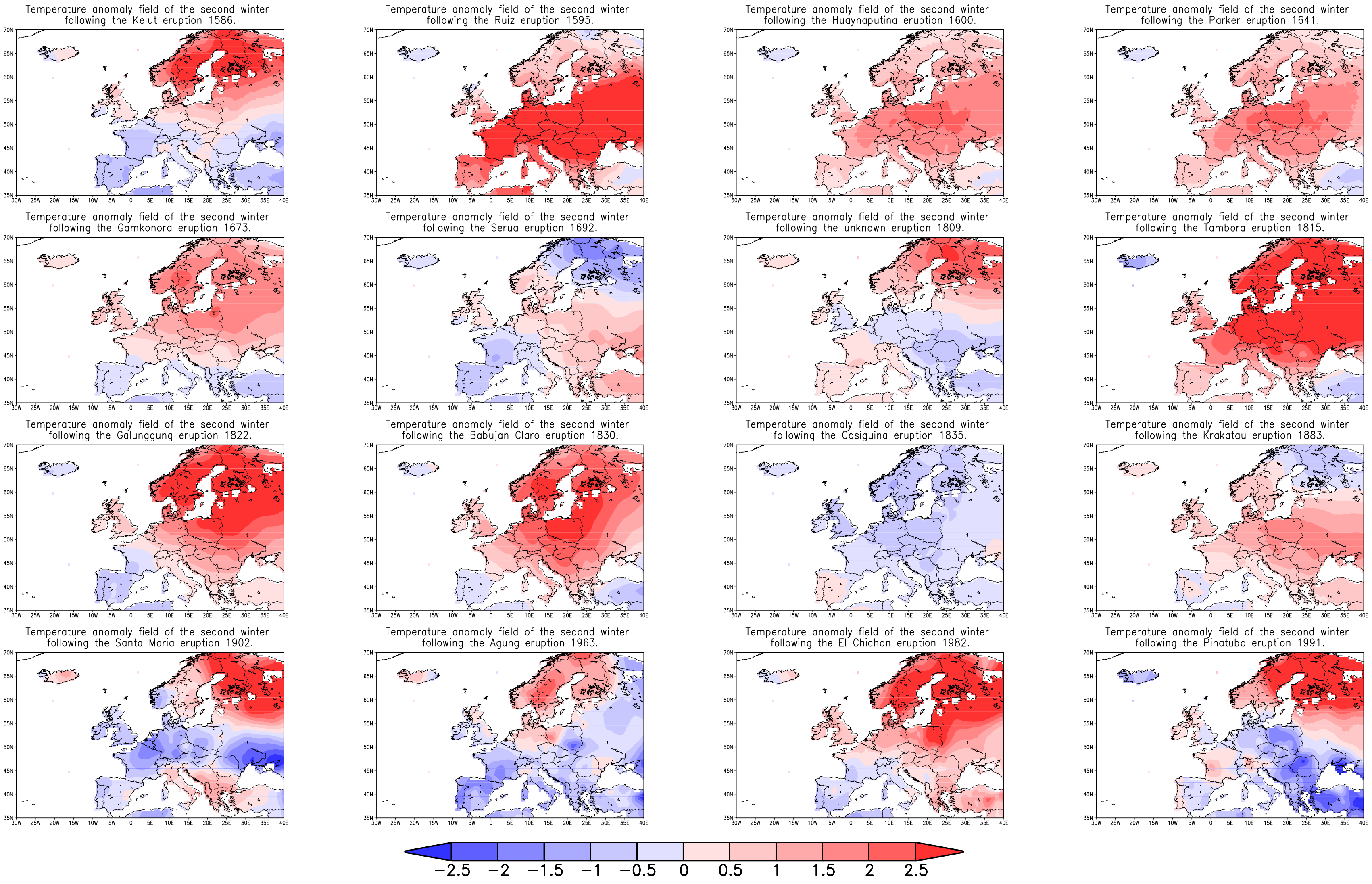

Figure 5.6: *European land surface temperature anomaly field (°C, shaded) of the second winter following each of the 16 selected major volcanic eruptions averaged in figure 5.3.*

The signal in the temperature of the second post-eruption winter (figure 5.6) is revealed to be less uniform. Still, a general trend to positive anomalies is apparent. An exception is observed in the second winter following the Cosiguina eruption (January 1835). In this case the second winter (1837) corresponds to 23–25 months after the eruption, thereby several months more than in most of the other volcanic episodes. The magnitude of the warming is large (up to over 2.5°C) in the majority of cases. In the case of Ruiz 1595 and Tambora 1815 the positive winter temperature anomalies extend almost all over Europe. The maximum warming is often located over north-eastern Europe and Scandinavia, whereas over Iceland and the Mediterranean no distinct effect can be noticed. Even if the overall winter signal is not homogenous, a tendency to positive anomalies with spatial variability can be stated, which corresponds well with the composite anomaly field in figure 5.3 (lower right panel).

5.1.4 Sensitivity Analysis by Leaving-one-out

In order to analyse the sensitivity of the composite anomaly fields to outliers and wrongly dated single eruptions I calculated the same composite fields displayed in figure 5.3 leaving out single eruptions. Figure 5.7 shows the leave-one-out composites of the second summer (upper panels) and the second winter (lower panels) leaving out the most positive and the most negative anomaly fields. Leaving out the second summer anomaly field following Babujan Claro eruption 1830, which represents a maximum cooling pattern (cf. figure 5.5), results in a composite with slightly reduced negative anomalies over Scandinavia (figure 5.7, upper left panel). Stronger negative anomalies over Scandinavia and virtually no warming over the Mediterranean can be observed in the summer composite field, leaving out the anomalous warm temperature field following the Santa Maria eruption 1902 (5.7, upper right panel). Comparing these two composite summer temperature composite field it can be stated, that the magnitude of the anomalies is sensitive to single eruptions but the overall pattern of temperature distribution remains the same. The lower panels in figure 5.7 show the composite temperature anomaly fields leaving out Tambora 1815 (lower left panel) and Cosiguina 1835 (lower right panel). Again the maximum temperature anomaly differs between the two composite anomaly fields, whereas the anomaly pattern remains the same in both panels.

5.1.5 Comparison of American and Asian Eruptions

Regarding the geographical positions of the selected volcanoes in figure 3.4 two distinct regions can be distinguished. Ten volcanoes are located in Asia at about 120°E and 5 volcanoes in Middle and South America at about 70–100°W. The dependence of climate response to eruptions on the latitude of the volcano is described in various publications (e.g. Robock 2000). In order to investigate the dependence on the longitude, the anomaly fields (figure

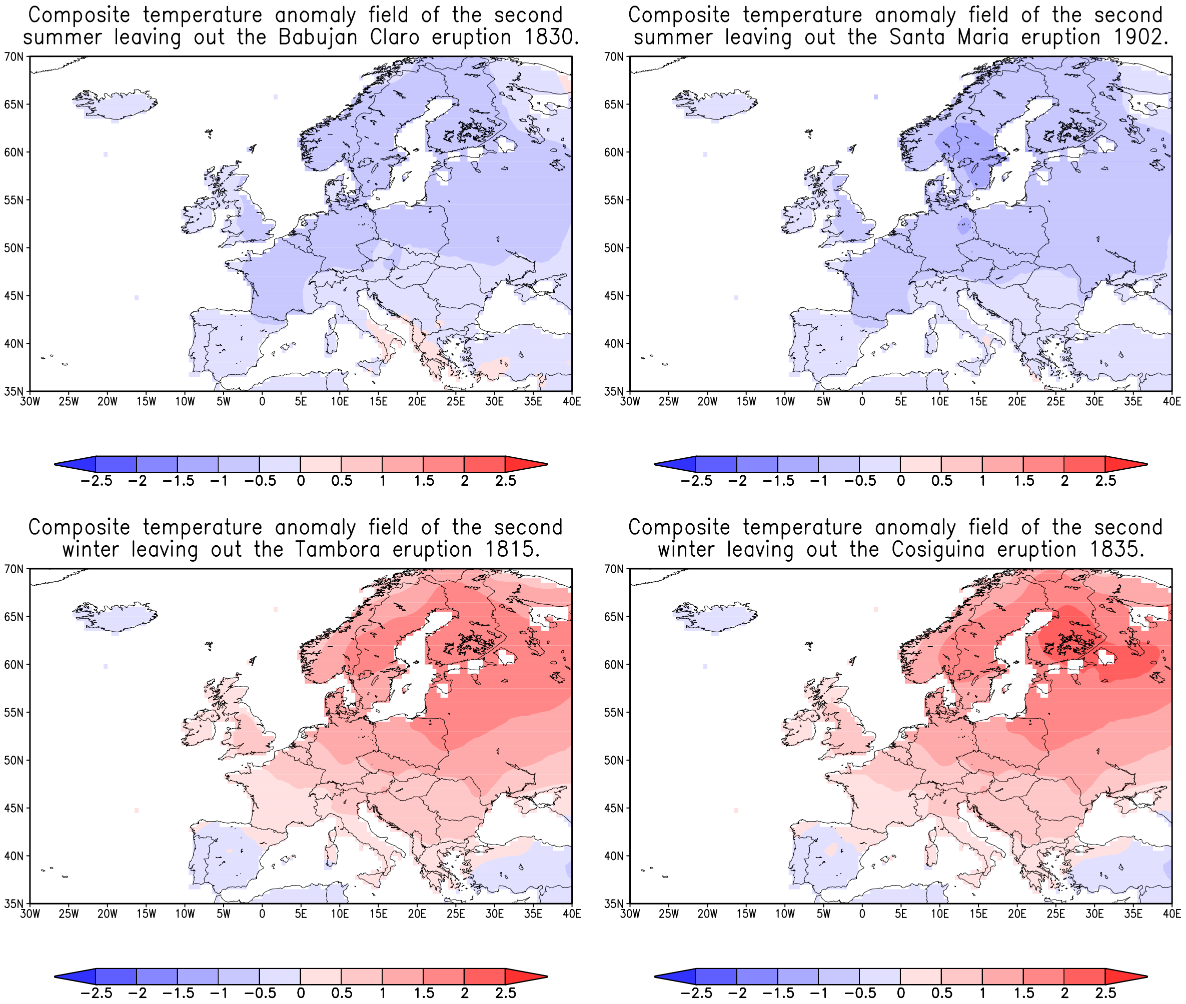

Composite temperature anomaly field of the second summer leaving out the Babujan Claro eruption 1830.

Composite temperature anomaly field of the second summer leaving out the Santa Maria eruption 1902.

Composite temperature anomaly field of the second winter leaving out the Tambora eruption 1815.

Composite temperature anomaly field of the second winter leaving out the Cosiguina eruption 1835.

Figure 5.7: *Composite European land surface temperature anomaly field (°C, shaded) of the second summer following 15 volcanic eruptions leaving out Babujan Claro 1830 (upper left panel) and Santa Maria 1902 (upper right panel) and second winter leaving out Tambora 1815 (lower left panel) and Cosiguina 1835 (lower right panel).*

Table 5.1: *Three selected major high-latitudinal volcanic eruptions of the period 1500–1998 used in this study. Year and month (if known) of the start and end of the eruption (Simkin and Siebert 2003) are indicated in column three and four. The volcanic indices VEI (Simkin and Siebert 2003) is given in column seven and the season, used as first season after the corresponding eruption in this study, in column eight.*

Volcano	Country	Start	End	Latitude	Longitude	VEI	first seas.
Grímsvötn/Laki	Iceland	1783 05	1785 05	64.4°N	17.3°W	4+	su 1783
Novarupta/Katmai	Alaska	1912 06	1912 10	58.3°N	155.2°W	6	au 1912
St. Helens	USA	1980 03	1986 10	46.2°N	122.2°W	5	su 1980

5.8) were averaged for the two different subregions mentioned above and compared with a composite of three major high-latitudinal eruptions of the period 1500–1998. This allows to draw conclusions on the dependence of the temperature response on latitudinal and longitudinal location of the volcano. The composites in figure 5.8 have to be interpreted with care as the number of averaged anomaly fields is relatively small for the American subregion and the high-latitudinal eruptions. Both the composite fields for the American and Asian subregions show a pronounced summer cooling and a winter warming pattern. Asian eruptions are followed by more negative summer temperature anomalies than American eruptions. The cooling pattern after eruptions in the Asian subregion extends all over Europe, whereas after American eruptions different regions even show slightly positive temperature anomalies. The winter warming on the other hand covers a larger region in the American composite field. However, these differences could be influenced by the fact that most of the Asian eruptions were of larger magnitude than the American eruptions (cf. table 5.1). The pattern for the high-latitudinal eruptions is very different from both tropical subregions in winter and summer. The composite field for the second summer reveals a non-homogenous pattern with negative temperature anomalies in Western Europe and positive anomalies in Eastern Europe. In winter and summer positive temperature anomalies are predominant in the east over Russia and negative anomalies over Western and Central Europe. The winter composite following high-latitudinal eruptions is strongly influenced by the extremely cold conditions in winter 1785, which are often attributed to the Grímsvötn/Laki eruption 1783. Taking in account the small number of fields in the composites it seems that the difference between the temperature response to high-latitude and tropical volcanoes is much larger than the difference between the response to Asian and American volcanoes.

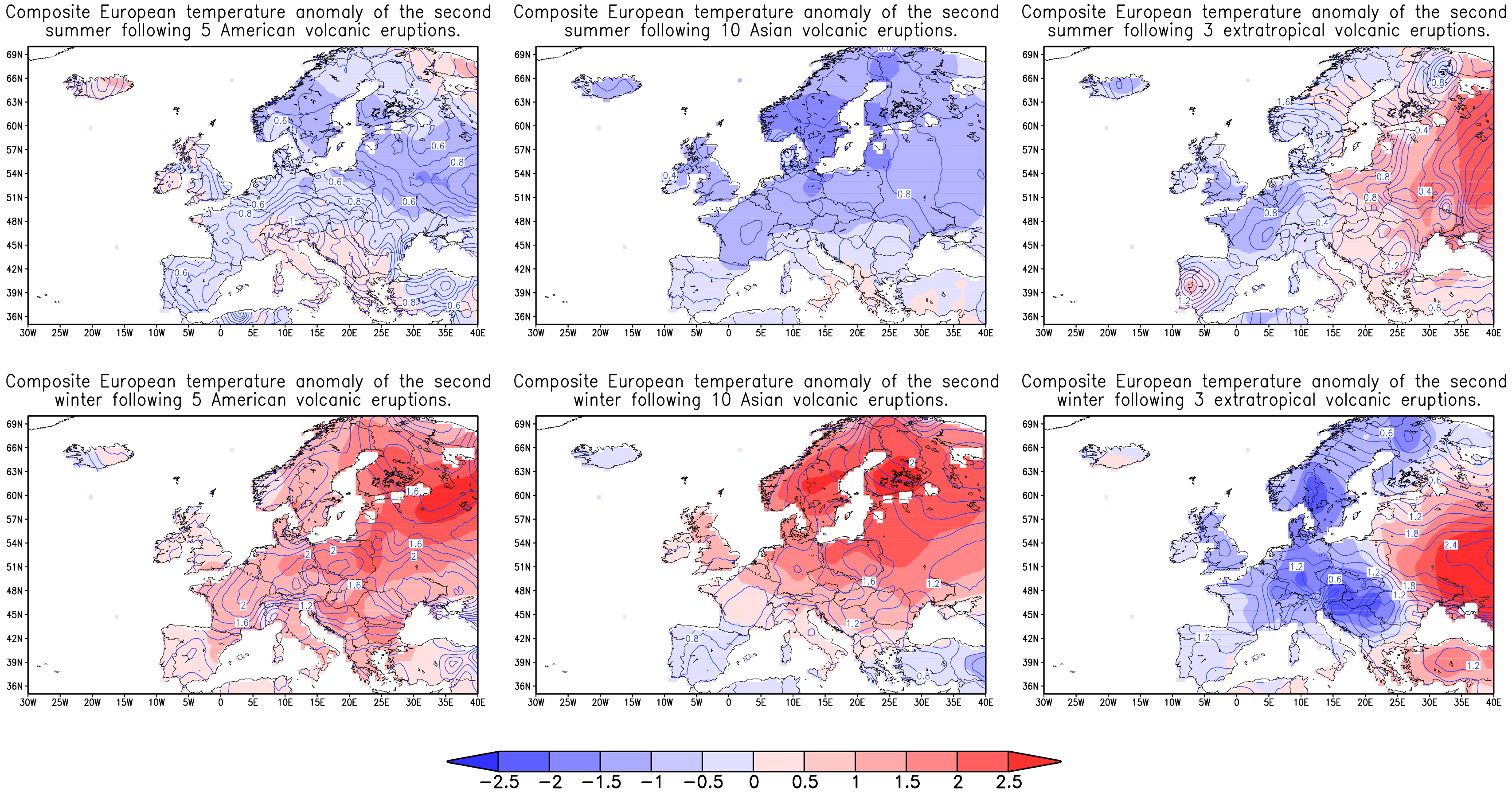

Figure 5.8: *Composite European land surface temperature anomaly field (° C, shaded) of the second summer (upper panels) and second winter (lower panels) following five American eruptions (left panels), ten Asian eruptions (middle panels), and three high-latitudinal eruptions (right panels). The blue contours mark the standard deviations.*

5.1.6 Medium-Term Temperature Response

So far I just considered the temperature of the first two years following volcanic eruptions. However, different publications (Bertrand et al. 1999, Crowley and Kim 1999, Zielinski 2000) suggest a climatic impact up to more than five years after major eruptions. Supposing the response to the volcanic forcing is decreasing in time after a maximum signal, it is more and more difficult to isolate the volcanic signal after several years by composite analysis. I choose to consider five post-eruption years, suggesting that the volcanic signal will be damped out by internal variability after this period. Figure 5.9 and 5.10 depict area averaged land surface temperatures (thick red line) of the European land regions for a ten year period including five pre- and five post-eruption years. The temperature fluctuations for each event are given in black lines and the composite of all eruptions is marked by the red line. All temperature curves are centred by removal of the mean across the ten years period. The significance of the composite temperature established from a Monte Carlo resampling procedure based on an ensemble of 10'000 random surrogates (details in section 4.3) are displayed in table 5.2. Column two includes the composite area averaged temperature (red line in figure) and column three to six the different quantiles of the resampling distribution. Years with positive/negative composite temperatures (P / N) significant at the 95% and 99% confidence level are marked by P*/N* and P**/N**, respectively.

The composite spatial averaged summer temperature (figure 5.9, red line) shows only small fluctuations in the pre-eruption period with relatively high variations in the individual events. It is clearly visible that the event occurring between year 0 and 1 is followed by a distinct change in the curve. The temperature is decreasing to a minimum (-0.45°C) in the second summer. At the same time the standard deviation is reduced, meaning that in most of the cases the temperature was cooling. For some of the events the temperature reaches its minimum already in the first summer. The cooling in the second summer is highly significant at a 99% confidence level (table 5.2). Increasing summer temperature can be observed the third and fourth summer, reaching a maximum warming in the fourth summer (+0.27°C), significant at a 95% confidence level. This suggests that the minimum temperature is followed by a rebound into positive anomalies before the volcanic signal is damped out by internal noise.

Figure 5.10 reveals large winter temperature variability for the individual events in pre-eruption period compensating for each other and resulting in only small variations of the composite temperature. There is no theoretical explanation for the negative peak in composite winter temperature in year 0 (winter before eruption). But as the standard variation is maximal in the same year it is suggested that the composite temperature is

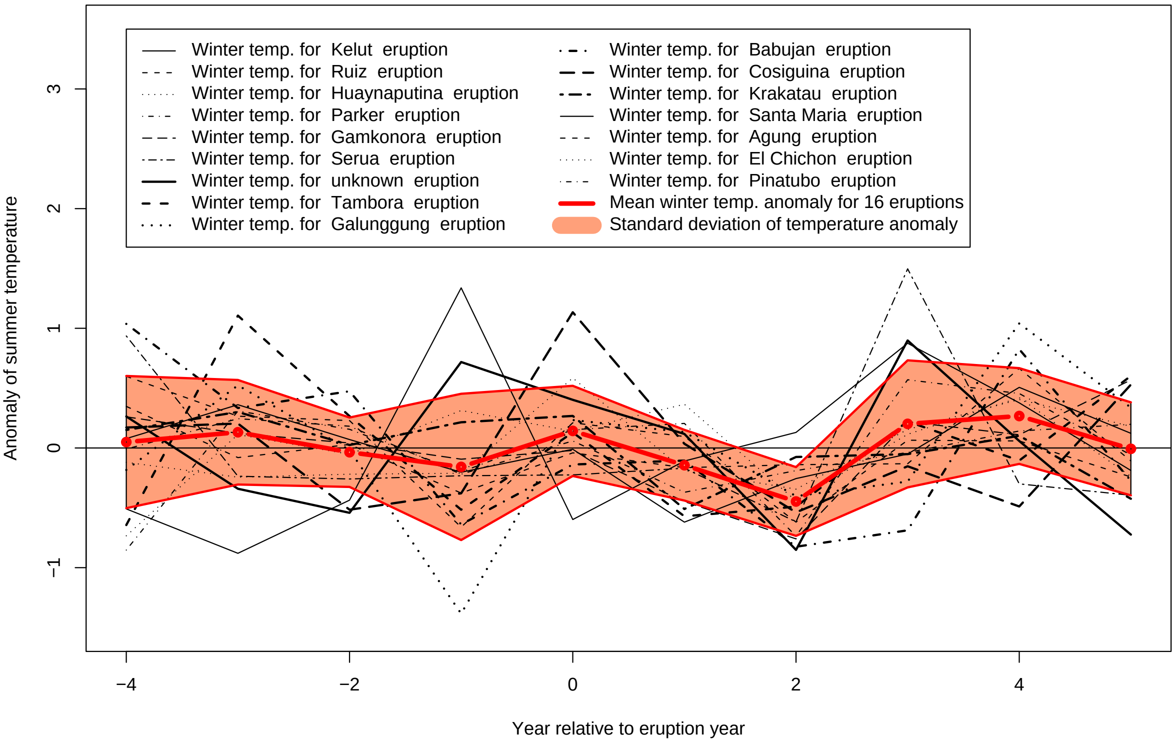

Figure 5.9: *European average land surface summer temperature anomaly (°C) for 16 tropical volcanic eruptions and composite average land surface summer temperature (thick red line) with standard deviations (orange).*

highly influenced by some outliers caused by other forcings and internal variability. Again the volcano event is followed by a distinct change in the composite temperature. The winter temperature increases after the eruption culminating in the second winter succeeding an eruption with a significantly (99% level) warmer composite temperature (+0.73°C). The standard deviation of the composite winter temperature is much smaller after the eruption indicating that in most of the cases the temperature was increasing. In the third years the winter temperature decreases to negative anomalies returning to positive anomalies in the fourth winter. It is remarkable that the fifth winter is characterised by a significantly negative temperature anomaly.

In a next step the same procedure including the Monte Carlo resampling was performed for each gridpoint over the five pre- and post-eruption years. The normalised temperature fields of the five post-eruption years are displayed in figure 5.11 and 5.12. The green contours mark the statistical significance as quantiles of the Monte Carlo resampled distribution (representing the 0.5%, 2.5%, 97.5% and 99.5% levels). The first two panels illustrating the temperature of the first and second summer show very similar anomaly patterns and areas of high significance

Table 5.2: *Average temperature (column two) of the five post-eruption summers (upper table) and winters (lower table) displayed in figure 5.9 and 5.10. The different quantiles after a Monte Carlo resampling (c.f section 4.3) are shown in column three to six. Years with positive composite temperatures (P) significant at the 95% and 99% confidence level are marked by P* and P**, respectively; Years with negative composite temperatures (N) significant at the 95% and 99% confidence level are marked by N* and N**, respectively. For the full table including the pre-eruptions, see table A.2 and A.3 .*

Year	Mean temp.	0.5%	2.5%	97.5%	99.5%	Significance
1	-0.14	-0.29	-0.22	0.23	0.30	N
2	-0.45	-0.29	-0.22	0.23	0.30	N**
3	0.20	-0.29	-0.22	0.23	0.31	P
4	0.27	-0.29	-0.22	0.23	0.31	P*
5	-0.01	-0.29	-0.22	0.23	0.31	N

Year	Average temp.	0.5%	2.5%	97.5%	99.5%	Significance
1	0.04	-0.72	-0.52	0.48	0.62	P
2	0.73	-0.68	-0.53	0.49	0.64	P**
3	-0.35	-0.67	-0.51	0.48	0.63	N
4	0.31	-0.68	-0.51	0.49	0.65	P
5	-0.75	-0.66	-0.51	0.50	0.65	N**

as the panels in figure 5.3. Panel 3 and 4 depict the spatial distribution of the warming in the third and fourth summer mentioned above. It is noteworthy that the significant positive anomalies in the fourth summer are limited to Central Europe and that again over Greece and the eastern Mediterranean an opposite pattern is dominant. Looking at the winter temperature in figure 5.12 the above mentioned warming culminating in the second winter can be observed. The third to fifth winter temperature fields show the same year-to-year variations as the area averaged composite temperature. It is remarkable that the variations have a much larger magnitude over Northern Europe than over Southern Europe. The cooling in the fifth winter is most significant over north-eastern Europe. The cooling pattern in the fifth year could be intensified by methodological reasons, as the mean over a relatively short period is removed, which is strongly influenced by the warming in the second winter.

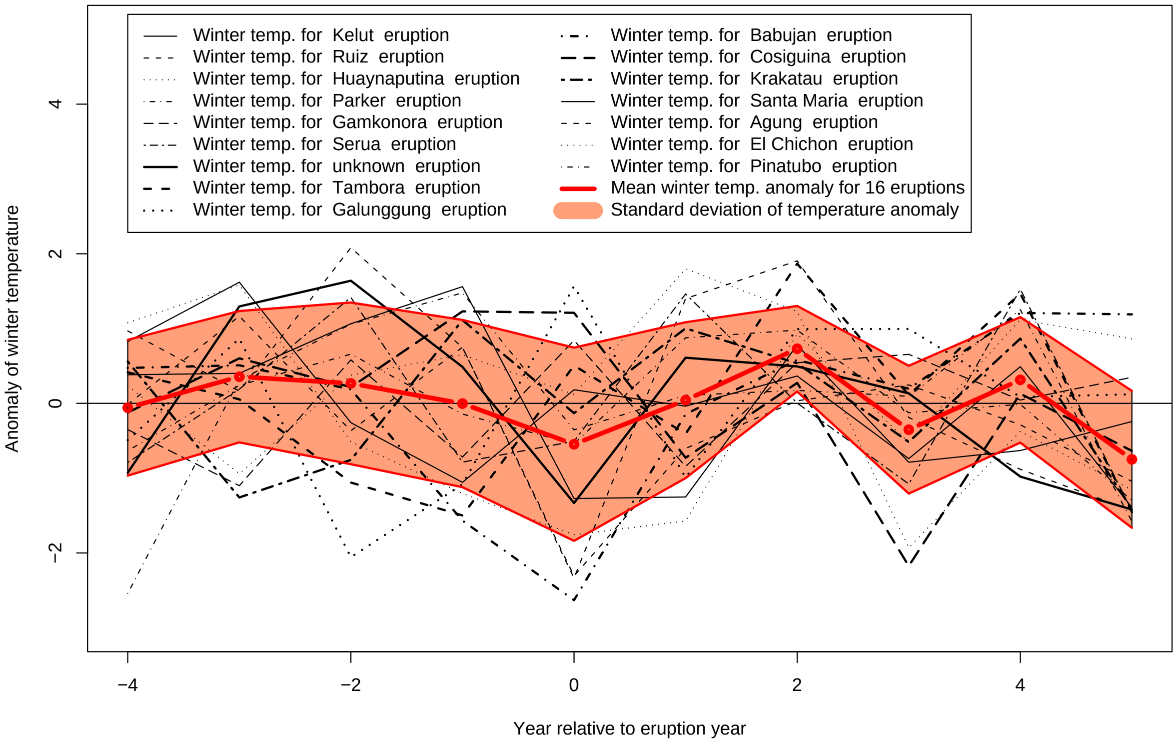

Figure 5.10: *European average land surface winter temperature anomaly (°C) for 16 tropical volcanic eruptions and composite average land surface summer temperature (thick red line) with one standard deviation (orange).*

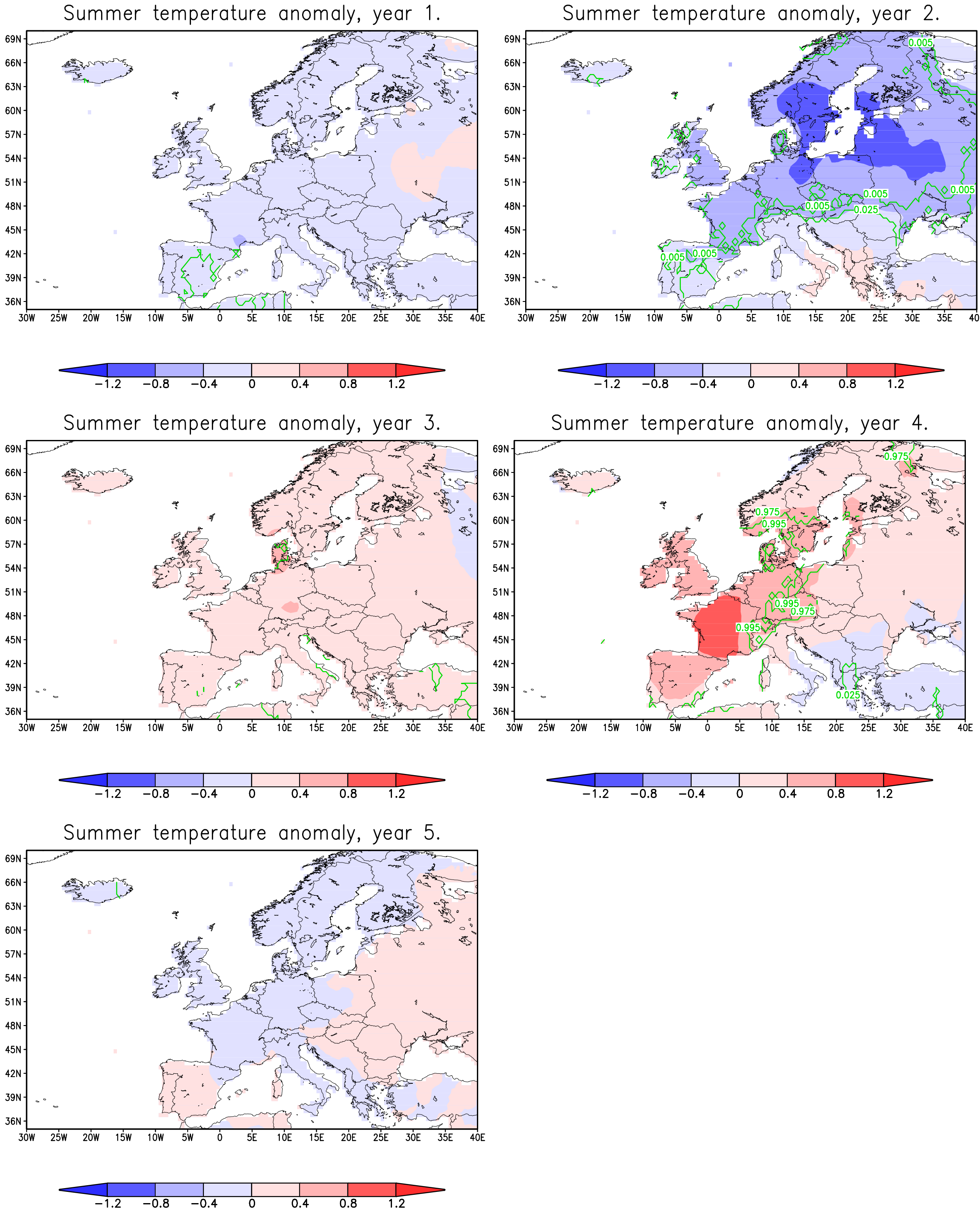

Figure 5.11: *European land surface summer temperature anomaly (shaded, °C) in the five post-eruption years of 16 tropical volcanic eruptions. The green contours mark the statistical significance as quantiles of the Monte Carlo resampled distribution (representing the 0.5%, 2.5%, 97.5% and 99.5% levels).*

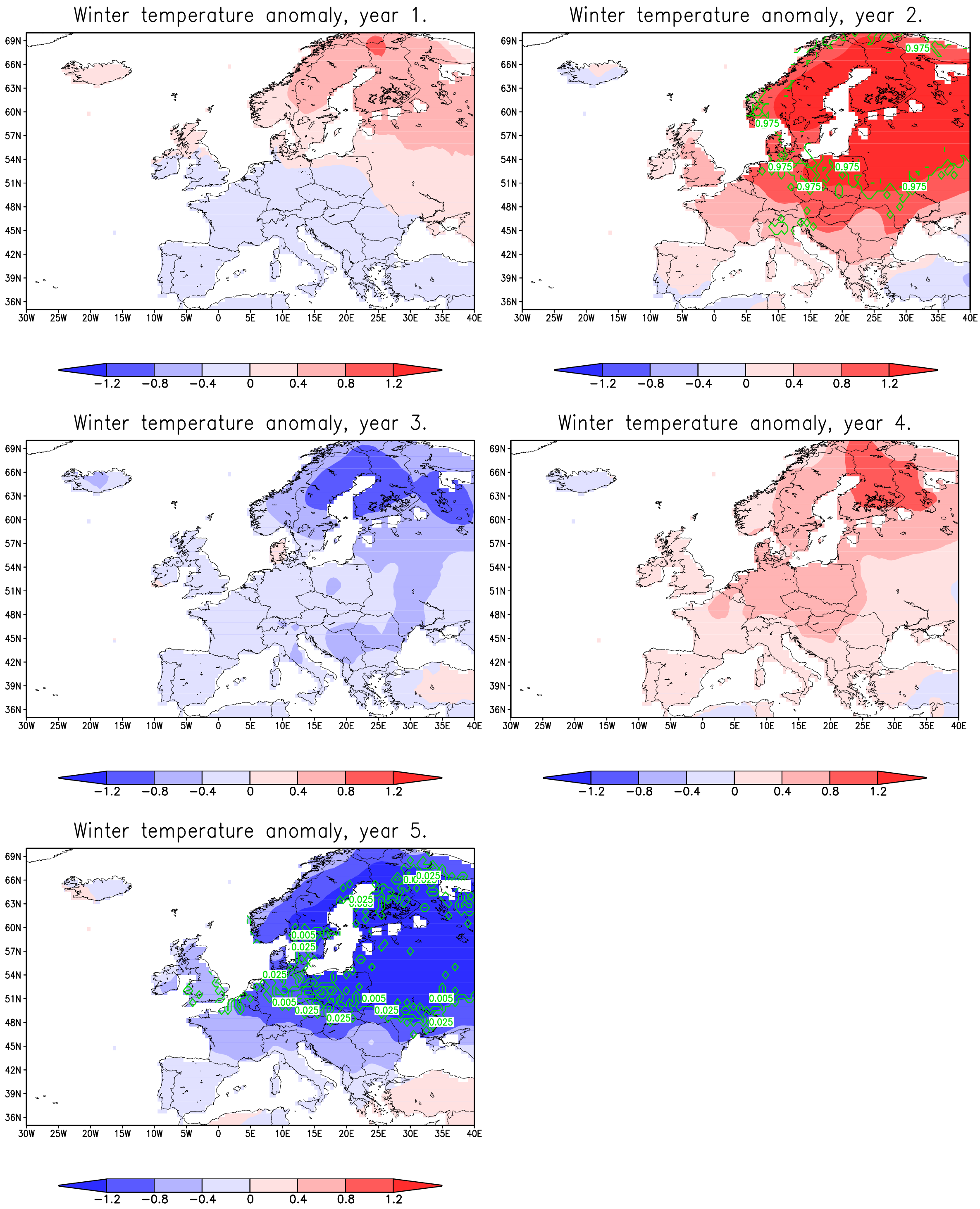

Figure 5.12: *European land surface winter temperature anomaly (shaded, °C) in the five post-eruption years of 16 tropical volcanic eruptions. The green contours mark the statistical significance as quantiles of the Monte Carlo resampled distribution (representing the 0.5%, 2.5%, 97.5% and 99.5% levels).*

5.2 Sea Level Pressure (SLP) and 500 hPa Geopotential Height (GPH$_{500}$)

5.2.1 Summer SLP and GPH$_{500}$

In this section the results illustrating the volcanic impact on sea level pressure (SLP) and 500 hPa geopotential height (GPH$_{500}$) are presented. It has to be pointed out that the SLP and GPH$_{500}$ estimates are reconstructed using the same predictors. The majority of predictors were also used to reconstruct the temperature fields presented above. Therefore the reconstructed fields for the different parameters are not independent and establishing a causal relationship is not allowed.

Figure 5.13 depicts the composite summer SLP field over the last five centuries (upper left panel) and the composite SLP anomaly fields of the three summers following volcanic eruptions. The composite summer SLP field is dominated by high pressure over the Azores. The anomaly fields show only negligible changes of the SLP field except for the second summer, in which weak positive SLP anomalies can be observed over Iceland and negative anomalies over north-eastern Europe.

The gradient of the composite summer GPH$_{500}$ field (1500-1998) (figure 5.14) is exactly north-south directed. In Western Europe the north-south gradient is stronger than in Eastern Europe. The composite anomaly fields of the three post-eruption summers show similar patterns as the SLP anomaly fields. The second summer shows even more pronounced centres of negative and positive anomalies over north-western and north-eastern Europe resulting in southward directed geostrophic wind.

5.2.2 Winter SLP and GPH$_{500}$

The composite European winter SLP field over the period 1500–1998 and the composite anomaly fields of the three winters following volcanic eruptions are displayed in figure 5.15. The composite winter SLP field 1500–1998 shows a pronounced pressure gradient from north-east to south-west with a maximum positive anomaly over Portugal and the Azores and a minimum west of Iceland. A second centre of positive anomaly is located over south-eastern Europe and the Black Sea. Looking at the composite anomaly fields it is noteworthy that the composite pressure anomalies in the first two winters are of larger magnitude than in summer. The SLP anomaly field of the first winter reveals positive pressure anomalies west of the British Isles and negative anomalies over north-eastern Europe. Combined with the absolute values of the last five centuries this leads to a north-south pressure gradient. Remarkable pressure changes can be observed in the second winter SLP anomaly field. Pronounced negative SLP

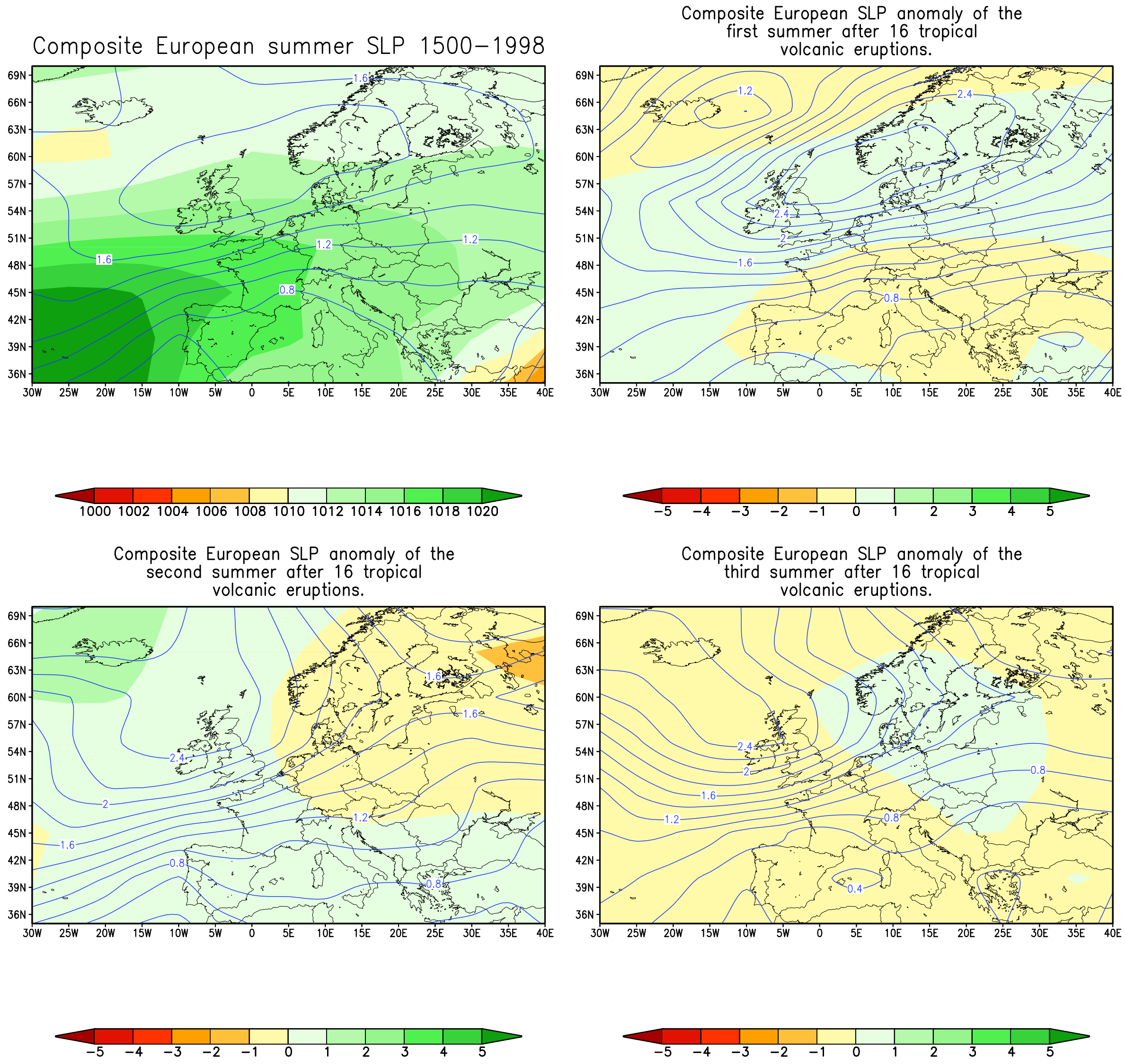

Composite European summer SLP 1500–1998

Composite European SLP anomaly of the first summer after 16 tropical volcanic eruptions.

Composite European SLP anomaly of the second summer after 16 tropical volcanic eruptions.

Composite European SLP anomaly of the third summer after 16 tropical volcanic eruptions.

Figure 5.13: *Composite field of absolute European summer SLP averaged over the period 1500–1998 (shaded, hPa) (upper left panel) and composite summer SLP anomaly fields of the first, second and third summer following 16 tropical volcanic eruptions. The blue contours mark the standard deviations in hPa.*

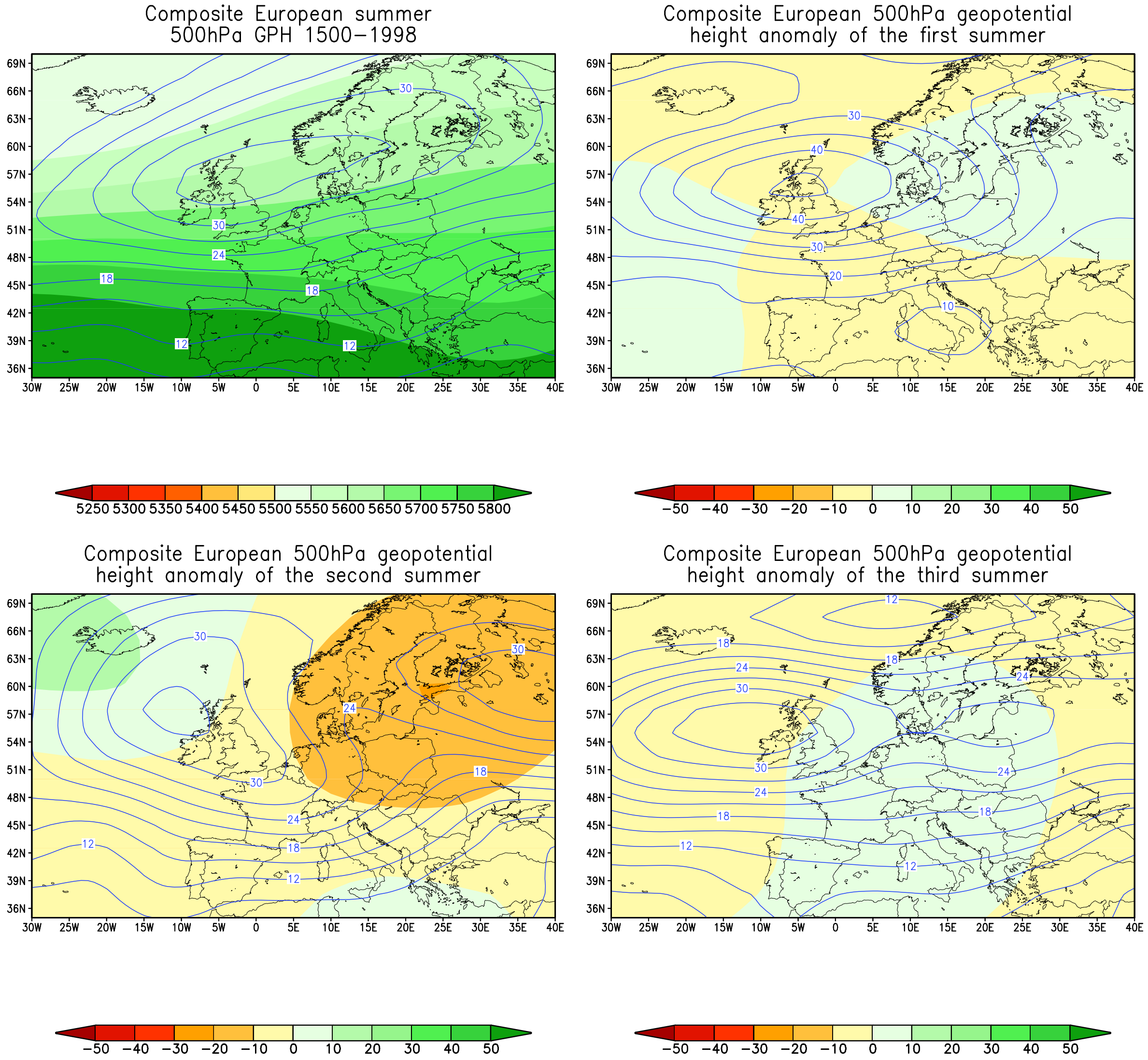

Figure 5.14: *Composite field of absolute European summer GPH$_{500}$ averaged over the period 1500–1998 (shaded, m) (upper left panel) and composite summer GPH$_{500}$ anomaly fields of the first, second and third summer following 16 tropical volcanic eruptions. The blue contours mark the standard deviations.*

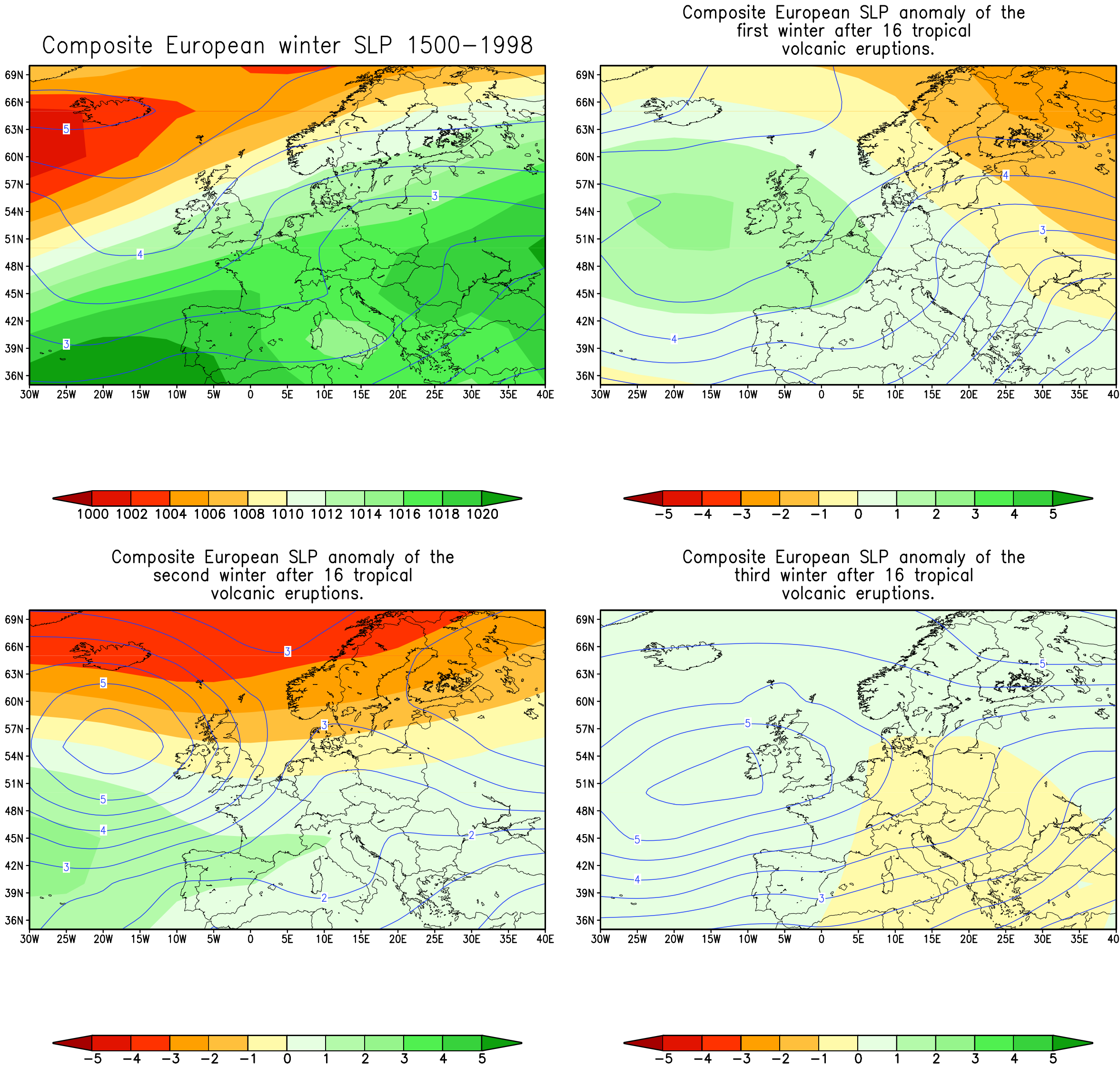

Composite European winter SLP 1500−1998

Composite European SLP anomaly of the first winter after 16 tropical volcanic eruptions.

Composite European SLP anomaly of the second winter after 16 tropical volcanic eruptions.

Composite European SLP anomaly of the third winter after 16 tropical volcanic eruptions.

Figure 5.15: *Composite field of absolute European winter SLP averaged over the period 1500–1998 (shaded, hPa) (upper left panel) and composite winter SLP anomaly fields of the first, second and third winter following 16 tropical volcanic eruptions. The blue contours mark the standard deviations in hPa.*

anomalies (up to 4 hPa) occur over the north and positive anomalies around the Azores and all over Southern Europe. This results in an enhanced pressure gradient of 7 hPa between the Azores and Iceland. Added to the composite absolute SLP field this leads to a large pressure gradient over the Atlantic and Western Europe resembling a positive North Atlantic Oscillation (NAO+) mode (see section 5.3).

The shading of the composite winter GPH$_{500}$ field (1500–1998) in figure 5.16 is nearly latitude parallel with a strong north-south gradient. The GPH$_{500}$ anomaly pattern of the second winter shows negative and positive anomalies similar to the SLP pattern, leading to enhanced geostrophic west winds. Figure 5.17 shows the SLP and GPH$_{500}$ fields for the second winter with the areas of statistical significance calculated by a Mann-Whitney test given in green contours. It is remarkable that both areas of maximum negative and positive anomalies, responsible for the strength of the geostrophic winds, are highly significant. In addition there is another significant area over south-eastern Europe in the SLP anomaly field and north of the Black Sea in the GPH$_{500}$ field.

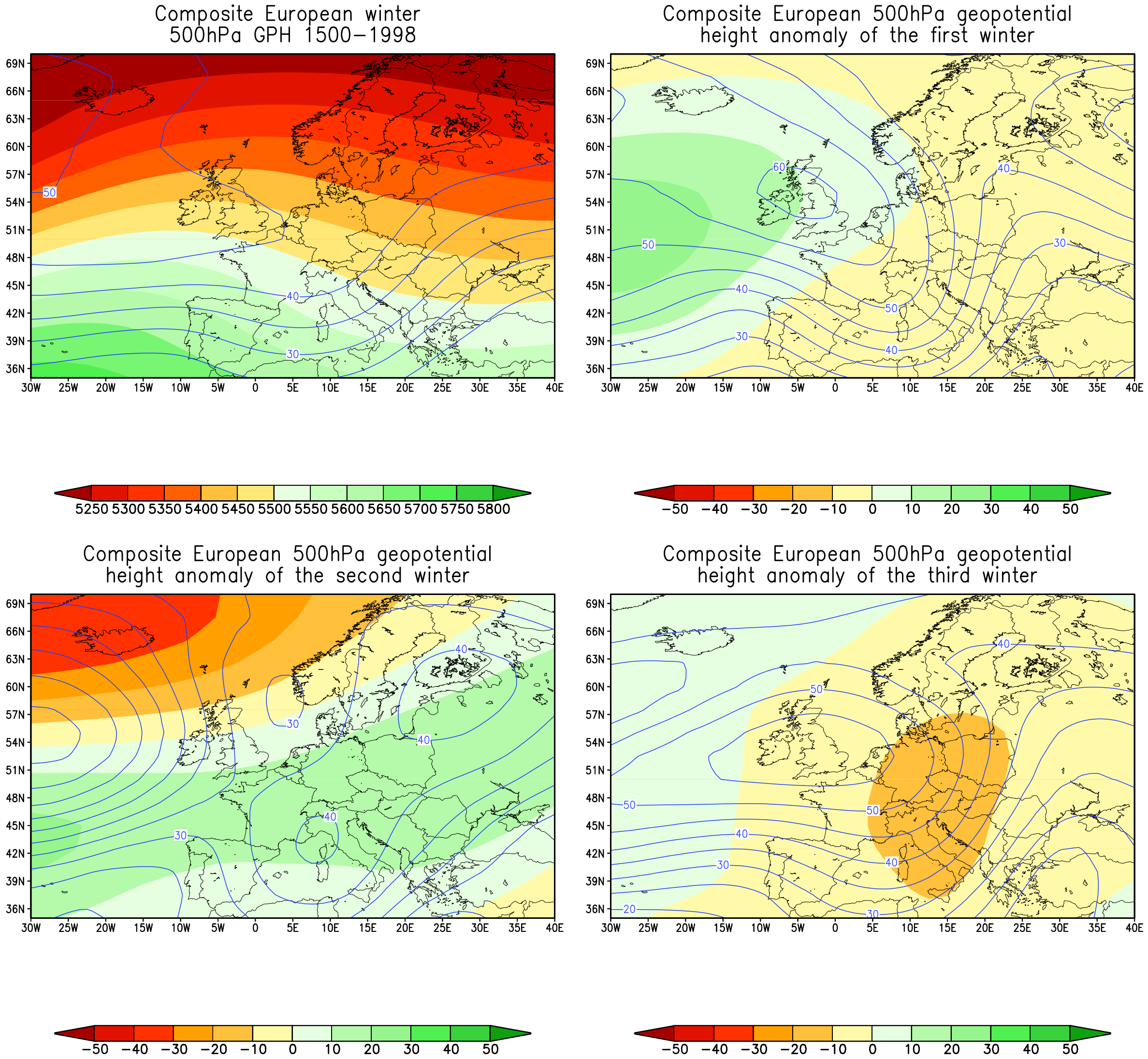
Composite European winter 500hPa GPH 1500–1998

Composite European 500hPa geopotential height anomaly of the first winter

Composite European 500hPa geopotential height anomaly of the second winter

Composite European 500hPa geopotential height anomaly of the third winter

Figure 5.16: *Composite field of absolute European winter* GPH_{500} *averaged over the period 1500–1998 (shaded, m) (upper left panel) and composite winter* GPH_{500} *anomaly fields of the first, second and third winter following 16 tropical volcanic eruptions. The blue contours mark the standard deviations.*

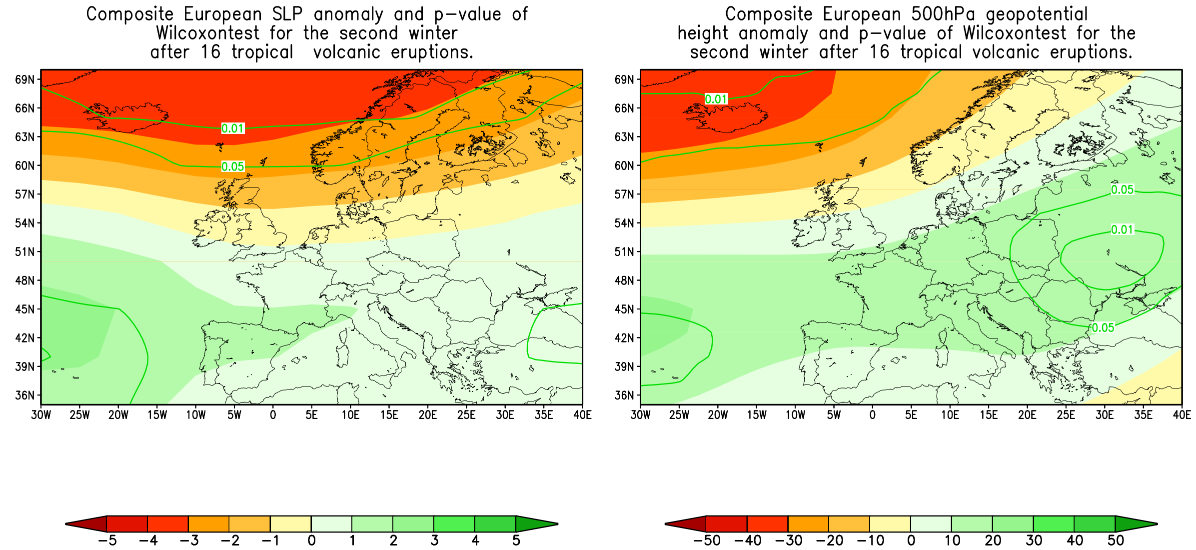

Figure 5.17: *Composite European winter SLP and GPH$_{500}$ anomaly fields of the second winter following 16 tropical volcanic eruptions. The green contours mark the statistical significance as p-values (representing 95% and 99% confidence level) of the Mann-Whitney Rank Sum Test.*

5.3 North Atlantic Oscillation (NAO)

The location of the maximum positive and negative anomalies in both the SLP and GPH_{500} of the second winter following the eruptions correspond well with a positive North Atlantic Oscillation (NAO+) pattern. Negative anomalies up to 4 hPa and 40 m GPH, respectively, are located over Iceland and positive anomalies of 3 hPa and 30 m GPH, respectively, slightly north of the Azores. I therefore suggest that the second winter is associated with a positive NAO index. In order to test this hypothesis I performed the same Monte Carlo resampling procedure used for area averaged summer and winter temperature. The NAO index was reconstructed monthly back to 1659 and seasonally for the period 1500–1658 (see Luterbacher et al. (2002a) for details). The composite winter NAO index for the five pre- and the five post-eruption years is displayed in figure 5.18.

Table 5.3: *Normalised winter NAOI (column two), reconstructed by Luterbacher et al. (2002a), of the five post-eruption years displayed in figure 5.18. The different quantiles after a Monte Carlo resampling (c.f. section 4.3) are shown in column three to six. Years with significant positive NAOI (P) at the 95% and 99% confidence level are marked by P* and P**, respectively; Years with significant negative NAOI (N) at the 95% and 99% confidence level are marked by N* and N**, respectively. For the full table including the pre-eruptions, see table A.4.*

Year	NAO index	0.5%	2.5%	97.5%	99.5%	Significance
1	-0.10	-0.55	-0.43	0.41	0.54	N
2	0.49	-0.55	-0.41	0.41	0.54	P*
3	0.02	-0.55	-0.42	0.42	0.54	P
4	0.51	-0.53	-0.41	0.40	0.53	P*
5	-0.53	-0.54	-0.42	0.41	0.54	N*

As expected the composite winter NAO index is positive in the second winter following the eruptions. After the pre-eruption period with a NAO index around zero, the index is increasing after the eruption, reaching a first maximum in the second winter (0.49) significant at a 95% confidence level. After a decrease to 0.15 in the third winter, the NAO index reaches another even higher maximum (0.51) in the fourth year. In the fifth winter the composite NAO index is changing to negative values. The post-eruption pattern of the NAO index curve reveals remarkable similarities with the composite winter temperature in figure 5.10.

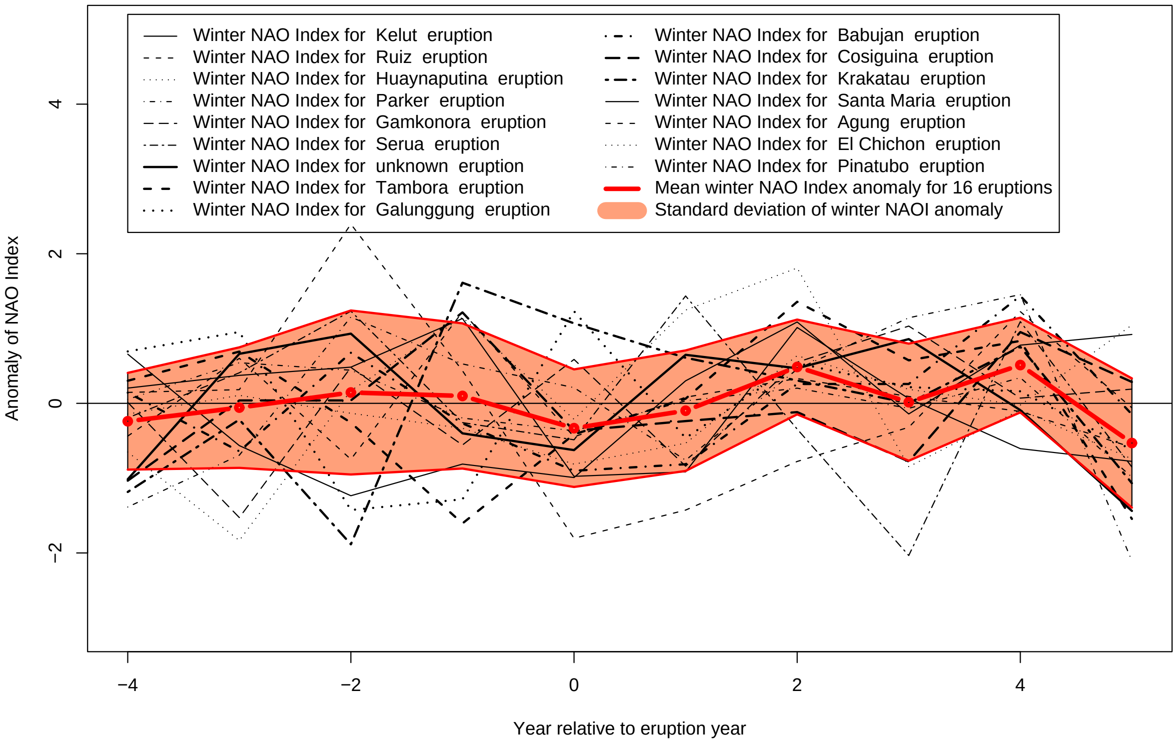

Figure 5.18: *Normalised winter NAOI, reconstructed by Luterbacher et al. (2002a), for 16 tropical volcanic eruptions and composite winter NAOI (thick red line) with standard deviations (orange).*

5.4 Precipitation

The connection between volcanic eruptions and precipitation is poorly investigated and supposed to be very complex. In addition the precipitation reconstruction of the 16th and 17th century is much less reliable than the other reconstructions. However, I present some results for this parameter to present the climatic response to volcanic eruptions as complete as possible.

The precipitation anomaly composites in figure 5.19 are less homogenous than the temperature and pressure composites and it is therefore more difficult to shortly describe them. Positive precipitation anomalies in the first summer can be observed over Southern and northernmost Europe, whereas negative anomalies are dominant between 50°N and 65°N. In the second summer dry conditions are prevailing over southern Scandinavia and the Mediterranean and wet conditions over north-eastern Europe. The first winter shows a remarkably positive precipitation anomaly over the Norwegian west coast associated with large standard deviations meanwhile negative anomalies are predominant all over western Central Europe and the Mediterranean. In the second winter anomaly composite reveals wet conditions at the European west coasts except for Portugal and dry conditions over south-eastern Europe and the Black Sea.

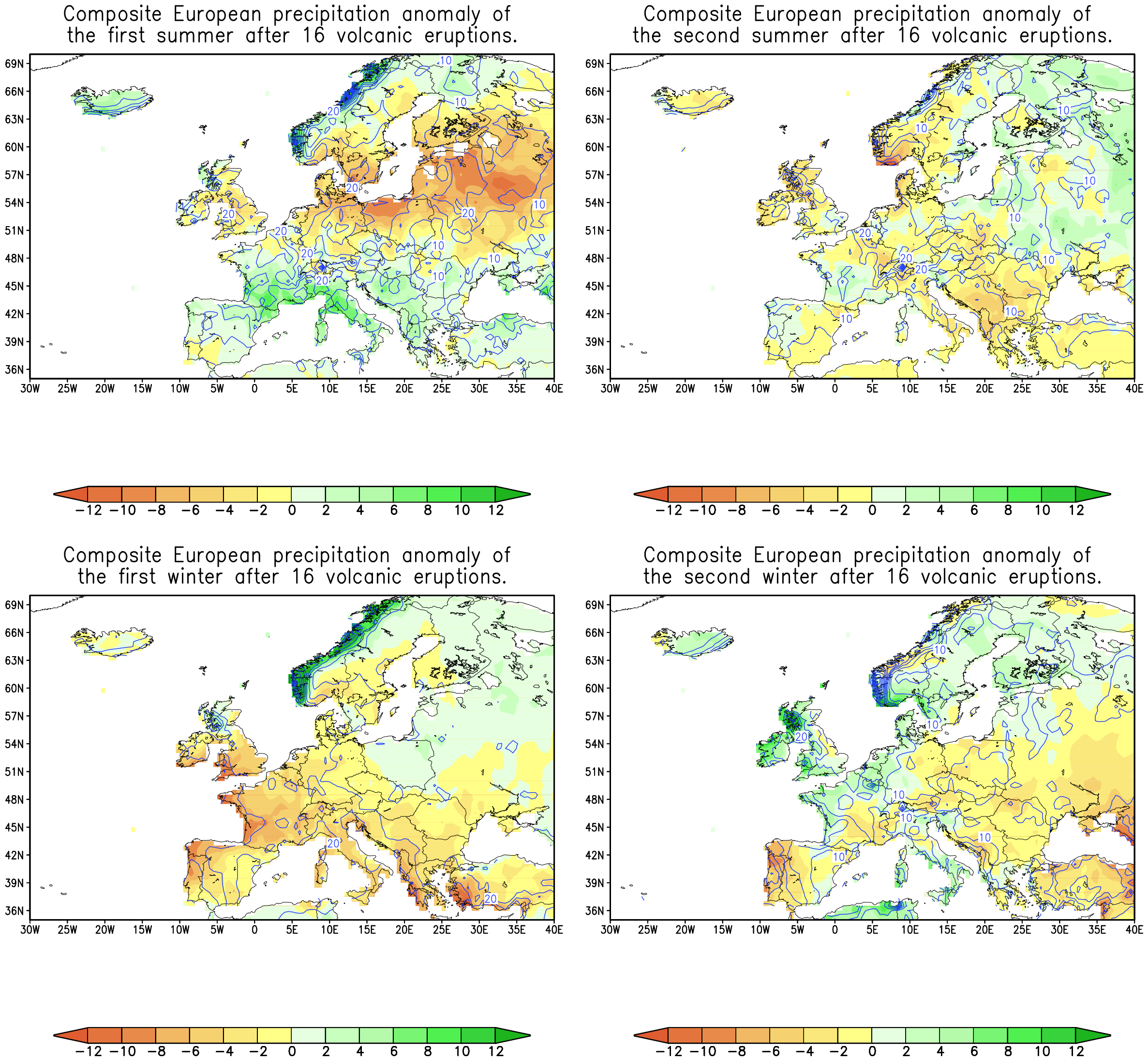
Composite European precipitation anomaly of the first summer after 16 volcanic eruptions.

Composite European precipitation anomaly of the second summer after 16 volcanic eruptions.

Composite European precipitation anomaly of the first winter after 16 volcanic eruptions.

Composite European precipitation anomaly of the second winter after 16 volcanic eruptions.

Figure 5.19: *Composite European summer (upper panels) and winter (lower panels) precipitation anomaly fields of the two years following 16 tropical volcanic eruptions. The blue contours mark the standard deviations.*

Chapter 6

Discussion

In this chapter some selected aspects of the results will be discussed. The results are compared with other studies examining the volcano-climate connection by climate modelling, climate reconstructions and instrumental observations. Due to the large amount of results only a part of them are discussed. I emphasise on results, which are relevant for the discussion of the objectives in section 1.1. In the first section the substantial problem of the data quality is addressed. The rest of the chapter is divided in sections corresponding to the different objectives of the thesis.

6.1 Data Quality

Interpreting the results it has to be taken into account, that all data for the period 1500–1900 are reconstructions. At the moment no statistical measure is available on the quality of these most recent reconstructions. The quality of the reconstructions will be tested in Luterbacher et al. (2003) for every grid point by applying each of the statistical models fitted during the period 1901–1960 and verified over the period 1961–1995. The statistical measure used for the quality check of the reconstructions will be the Reduction of Error (RE) (Lorenz 1956). RE ranges from $+1$ (perfect agreement between reconstructions and analysed fields) to $-\infty$, with $\mathrm{RE} = 0$ no better than climatology (i.e. the mean of the climatological data in the calibration period), $\mathrm{RE} > 0$ better than the calibration mean and $\mathrm{RE} < 0$ no useful information in the reconstructions. It would be desirable to compare the RE values with the different post-eruption anomaly fields to determine the quality of the composites. The RE values were calculated for previous reconstructions, using similar predictors. The climate estimations revealed to be trustworthy over the last centuries (not shown). The RE values indicate winter temperature and pressure reconstructions to be most reliable back to 1700 (for summer back to around 1750) and precipitation data to around 1750. However, in this case, there are areas with reduced skills, such as Southern Europe (not shown). I try to compensate for the lack of information on data quality of the used record by comparing our results with various other studies.

6.2 Direct Radiative Forcing on Temperature

6.2.1 European Area-averaged Summer Temperature

Figure 5.9 depicts the composite summer temperature for the five pre- and post-eruption years of 16 volcanic eruptions, revealing a significant cooling in the two post-eruption summers. These results compare relatively well with Robock and Mao (1995), who observed a similar cooling in the zonally averaged summer temperature (figure 6.1) between 30°N and 60°N by compositing 6 major volcanic episodes (Krakatau 1883, Santa Maria 1902, Novarupta/Katmai 1912, Agung 1963, El Chichon 1982, Mount Pinatubo 1991). They used a global surface temperature data set provided by the Climate Research Unit (CRU) for the years 1854–1993 (Jones et al. 1991, Jones and Briffa 1992). Figure 6.1 illustrates their monthly composite temperature over the five pre- and post-eruption years revealing weak negative anomalies in summer of year 0, of about -0.1°C, a significant maximum cooling in summer of the year 1 (around -0.3°C) and a weaker cooling of about -0.2°C in the summer of year 2.

I suppose, that the maximum cooling, found in the second summer (this study) instead of year 1 (Robock and Mao 1995), is partly the result of a different methodological set up in the definition of the post-eruption seasons. First summer in this study corresponds to the summer in year 0 or year 1 in figure 5.9, depending on the month of the eruption, and the second summer corresponds to summer of year 1 or year 2, respectively. The difference in the magnitude of the cooling can be explained by the difference in the limitation of the research area and the different selection of eruptions. This study includes only major tropical volcanoes, which were in the case of the two largest eruptions, Tambora 1815 and Huaynaputina 1600, followed by extraordinary strong summer cooling. The composite in Robock and Mao (1995) does not reach as far back, but on the other hand includes the high-latitudinal eruption of Novarupta/Katmai, showing negative anomalies in the first summer, but a warming in the second post-eruption summer. The composite temperature field following 3 high-latitudinal eruptions (figure 5.8, this study) indicates similar positive anomalies over large parts of Europe during the second summer. I conclude that there is a difference of the summer response to tropical eruptions and high-latitudinal eruptions, as the maximum cooling following high-latitudinal eruptions tends to occur in the first post-eruption summer and in the second summer following tropical eruptions. The immediate response after high-latitudinal eruptions could be interpreted as the consequence of the relatively fast longitudinal transport of

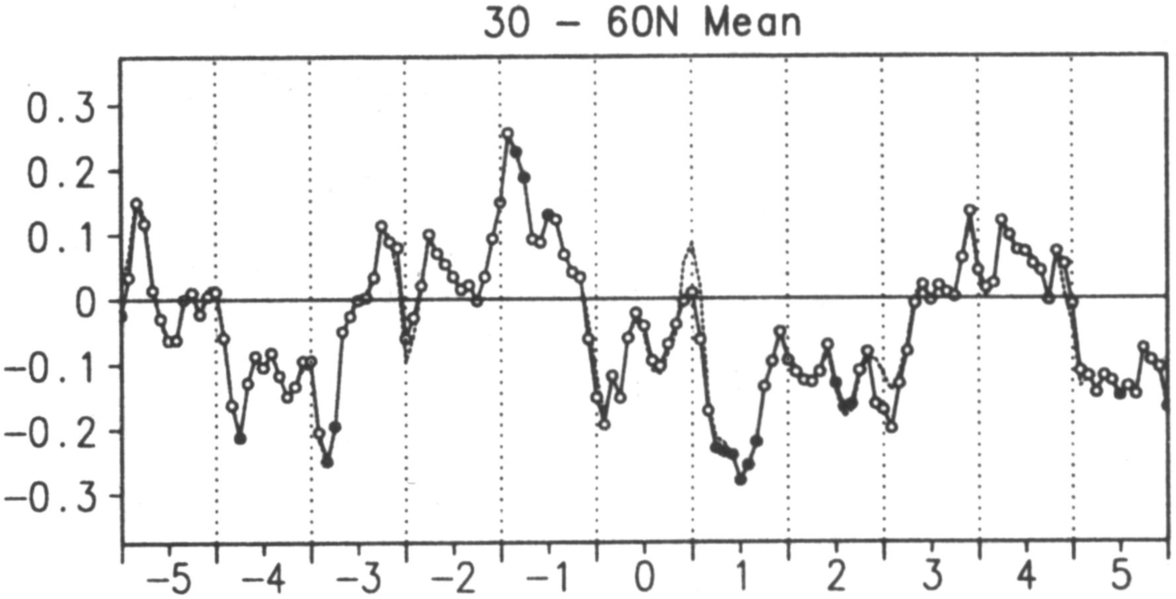

Figure 6.1: *Zonal mean (30–60° N) composite temperature anomalies for six volcanic eruptions with respect to the mean for the 5-year period before the eruption. The points that are significantly different from 0 are shaded. The dashed line without the dots is the same analysis, without removing ENSO. The lower axis shows the years labelled at the centre of each year. The left axis shows the temperature anomaly in ° C (Robock and Mao 1995).*

aerosols compared to the latitudinal transport. However, more evidence and information is required to prove this suggestion. Robock and Mao (1995), Robock (2000) and Parker et al. (1996) suggested a difference in the winter temperature response of tropical eruptions and high-latitudinal eruptions (see below).

Several other publications support our results of an area-averaged post-eruption summer cooling. However, there are differences in the timing and the magnitude of the maximum cooling. Parker et al. (1996) did not separate the different seasons and simply composited the post-eruption month of the tropical eruptions Krakatau 1883, Pelee-Soufriere-Santa Maria 1902, and El Chichon 1982, taking the eruption as month 0. They found negative post-eruption anomalies in the combined global land surface air with sea surface temperatures culminating to nearly -0.2°C (-0.25°C with ENSO-removed temperatures, see Parker et al. (1996) for details) in month 15. Kelly et al. (1996) used the same set up, but taking January of the eruption year as month 0. Using a global temperature data set by Jones et al. (1991) and Jones and Briffa (1992), they found a global cooling of about -0.2°C between month 14 and month 32. Wanner et al. (2000b) examined the average temperature of the first and second summer following six pre-industrial volcanic events. They found very cold summer temperatures in eight of twelve summers. These findings support our results, however, they are difficult to compare as the size of averaged areas differs substantially.

Angell and Korshover (1985) averaged the temperature over Europe, the same research area as this study, but with a slightly differing definition of its limitations. They composited yearly mean European temperature observations following the Asama-Laki 1783 (high-latitudinal), Tambora 1815, Cosiguina 1835, Krakatau 1883 and Pelee-Soufriere-Santa Maria 1902 eruptions. The resulting composite reveals a post-eruption cooling of -0.3°C in year 1, -0.4°C in year 2 and -0.3°C in year 3 (with respect to a pre-eruption period of ten years).

Briffa et al. (1998) used a network of temperature-sensitive tree-ring-density chronologies to provide information on year-by-year changes in NH summer (April to September) temperatures. The high-resolution time series are used to investigate the different extents of the post-eruption cooling during the past 600 years. Figure 6.2 depicts the NH tree-ring-density anomalies (left-hand axis), the regression-based estimates of NH mean summer temperature (right-hand axis) and the main explosive eruptions (VEI 5, 6 and 7) on the lower axis. The large effect of some major eruptions is apparent. The lowest tree-ring density value and thereby the most severe short-term Northern Hemisphere cooling event (-0.8°C) of the past 600 years occurred in 1601, the year after the Huaynaputina eruption. Evidence of other eruptions indicated by years of low tree-ring-density can be ascribed to Kelut (year of reduced tree-ring-density: 1587), Gamkonora (1675), Parker (1641/1642/1643), Tambora (1816/1817/1818), Cosiguina (1836) and Krakatau (1884). The estimated NH mean temperature cooling in these post-eruption summers is of the same magnitude (0.2–0.8°C) as the negative European temperature anomalies composited in this study.

This study as well as all the above mentioned publications suggest a maximum radiative cooling effect about one or two years after an eruption. Volcanic indices and studies on radiative effects, on the other hand, indicate a maximum radiative forcing immediately after an eruption and the eruption year itself, rapidly decreasing and disappearing in 2–5 years afterwards, depending on the sulphur release of the eruption (Mitchell 1970, Minnis et al. 1993, Sato et al. 1993, Robock and Free 1995, Andronova et al. 1999, Robertson et al. 2001, Lamb 1970). The question arises, why the maximum cooling and radiative forcing do not occur simultaneously. Bertrand et al. (1999) give a possible explanation for this phenomenon. They performed numerical experiments with a two-dimensional climate model, showing that the temperature response follows the forcing relatively closely, but that the time for temperature to return to pre-perturbation is much longer than the time for optical depth to recover. This lag is first related to the heat capacity of the system and secondly to the amplification of the climate response by the snow and ice albedo-temperature feedbacks and the water vapour-temperature feedback (Bertrand et al. 1999).

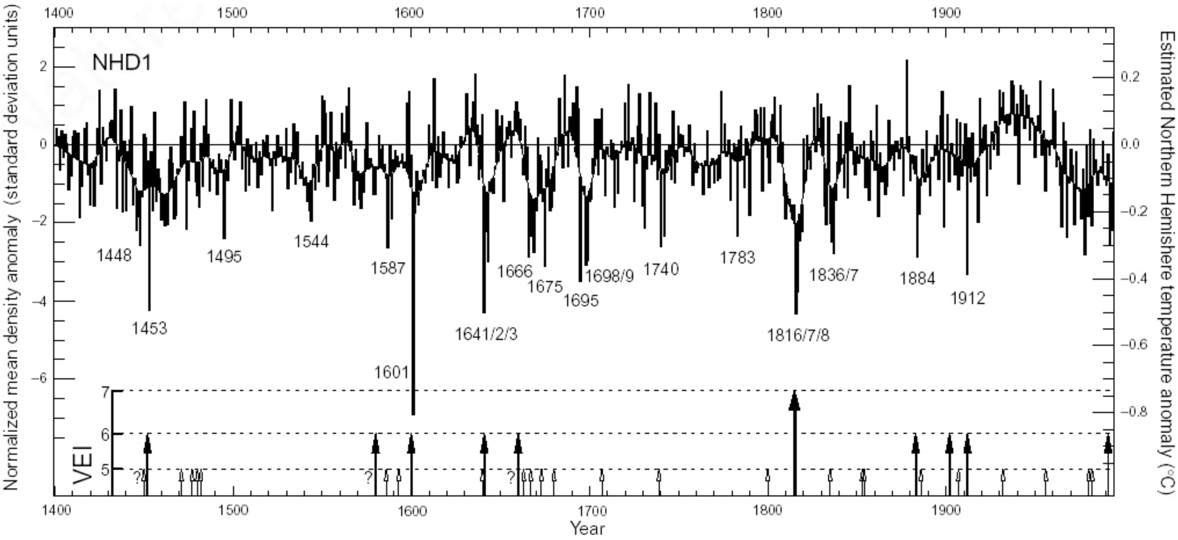

Figure 6.2: *Standardised NH tree-ring-density anomalies from the AD 1881–1960 period (left-hand axis) and in the form of regression-based estimates of NH mean summer temperature anomalies (right-hand axis). The curve shows bidecadal smoothed values. The main explosive eruptions (VEI 5, 6 and 7) are indicated on the lower axis. Question marks indicate uncertainty because dates are based on radiocarbon (Briffa et al. 1998).*

6.2.2 Spatial Patterns of European Summer Temperature Anomalies

In this section the focus is no longer on timing, but on spatial differences of the maximum radiative summer cooling within Europe. Figure 5.3 (upper panels) illustrates the composite summer temperature anomaly fields following 16 eruptions showing a homogenous cooling of 0–0.5°C in the first and a more pronounced cooling with a maximum over Northern Europe in the second summer. Figure 6.3 shows the global composite summer temperature anomaly field calculated by Robock and Mao (1995) for the six volcanic eruptions mentioned above. Again a comparison with our results is difficult, as there are differences in the definition of the first and second year and the selection of composited eruptions. However, the two anomaly fields for the second summer over Europe compare reasonably well with each other. In both fields the most negative temperature anomalies are located over central Scandinavia and the Baltic. The difference in the magnitude of the anomalies might be caused by the different selection of eruptions (a high-latitudinal volcano is included in Robock and Mao 1995).

As it is problematic to compare composite anomaly fields calculated by a different set of eruptions, I compare the spatial cooling pattern for a specific event, "The Year Without a Summer", 1816. The cooling in summer 1816 over Europe and North America after the devastating Tambora eruption 1815 is probably the most written about weather event in history (Chenoweth 1996). Figure 6.4 allows a detailed comparison of the summer (April to

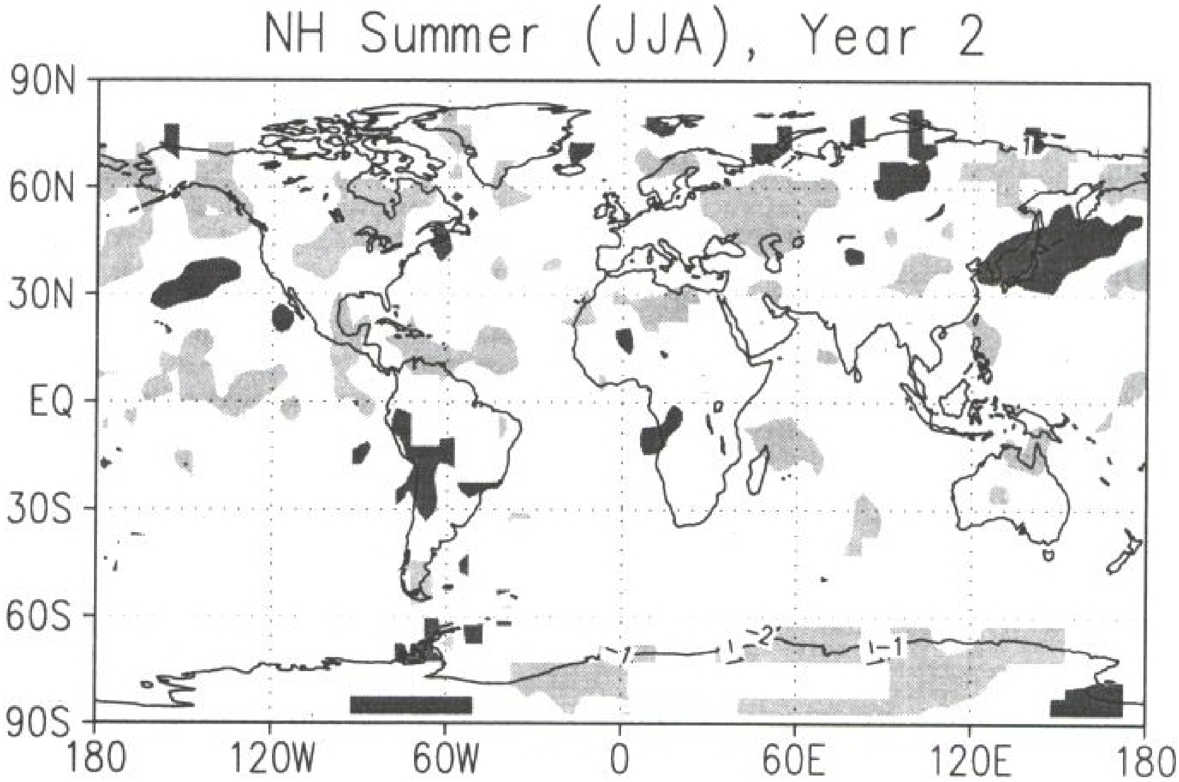

Figure 6.3: *Map of temperature anomalies for the second NH summer following the eruptions averaged for all six volcanoes. Areas with anomalies < -0.25° C are shaded lightly and areas with anomalies > +0.25° C are shaded dark. Contours are drawn with an interval of 1° C, with the 0° C contour not shown (Robock and Mao 1995).*

September) 1816 anomaly pattern of normalised tree-ring-density anomaly (Briffa et al. 1998) and surface temperature reconstructions for the same period (this study). Since the tree-ring density network and the predictands for the temperature reconstruction (Luterbacher et al. 2003) are fully independent, it is highly remarkable that the two patterns are in such a good agreement. Both panels show pronounced negative anomalies all over Central Europe, Spain, Italy, the British Isles and most of Scandinavia. Over south-eastern and north-eastern Europe on the other hand weak positive anomalies or anomalies close to zero are dominant. This example points to a good agreement also in the spatial distribution of the temperature reconstructions used in this study with other temperature estimates.

Figure 5.5 depicts the European surface temperature fields of the second summer following each of the 16 volcanic eruptions in table 3.2. The similarity of the 16 summer anomaly fields is highly remarkable. The homogeneity of the temperature response over all 16 eruptions can be interpreted as a result of the fact that the volcanic signal is a short, but very strong radiative forcing, resulting in distinct temperature response and dominating the other forcing

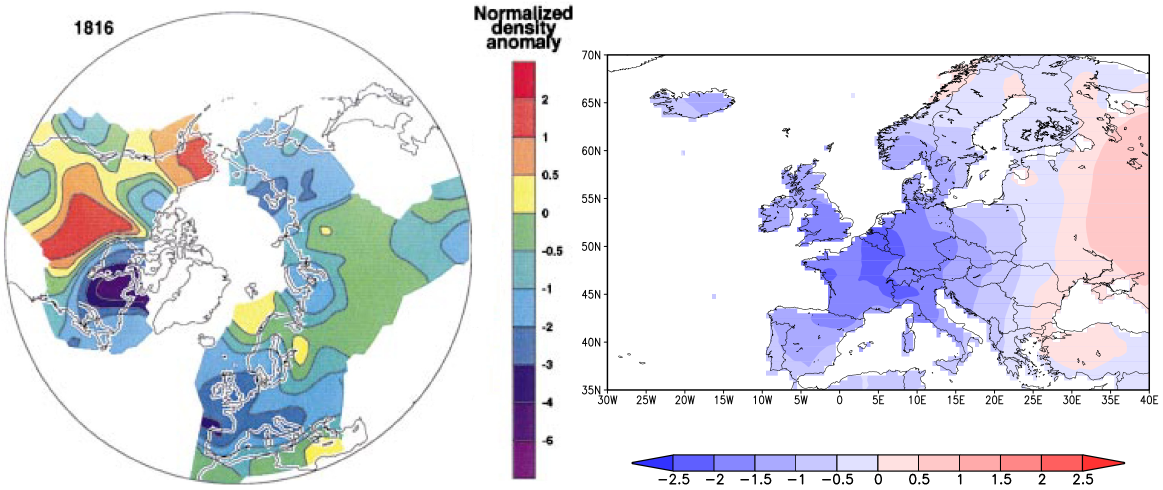

Figure 6.4: *Spatial pattern of normalised tree-ring-density anomalies, corresponding to summer (April to September) temperature anomalies (left panel) (Briffa et al. 1998) and European surface temperature anomaly field of summer (April to September) 1816 (wrt 1881–1960) (this study).*

for one to two years. Figure 6.5 illustrates the maximum global volcanic radiative forcing (rightmost bar) following the Pinatubo 1991 of about -3 Wm^{-2} (Hansen et al. 2002) compared with the global, annual mean radiative forcings 1750–2000 (IPCC 2001). It is apparent that the volcanic forcing, at its maximum, is dominant over the other forcings. The negative radiative forcing of the eruption of Mount Pinatubo exceeded the magnitude of the positive forcing associated with the greenhouse gases during the second half 1991 and much of 1992 (McCormick et al. 1995). The estimate of the maximum radiative forcing following Pinatubo eruption in Hansen et al. (2002) is substantially smaller than in Andronova et al. (1999), -5.4 Wm^{-2}, and larger than in (Ramachandran et al. 2000), mainly due to different assumptions on the aerosol optical depth. It has to be taken in consideration that the radiative forcing varies largely over the globe and can reach much higher values over some regions. For the eruptions of Agung 1963 and El Chichon 1982 the maximum global forcing is estimated to about -2 Wm^{-2} (Hansen et al. 2002). Summarised this values confirm my suggestion on the major role of the volcanic radiative forcing in the first and second post-eruption years resulting in a distinct temperature response. Crowley and Kim (1999) and Crowley (2000) estimated that 22–23% of the decadal-scale temperature variance can be explained by volcanism. Over the interval 1400–1850, the volcanic contribution increases to 41–49%, thereby indicating a very important role for volcanism during the Little Ice Age (Crowley 2000, see also Luterbacher et al. 2001).

I made several attempts to compare the modelled zonal distribution of net radiative forcing

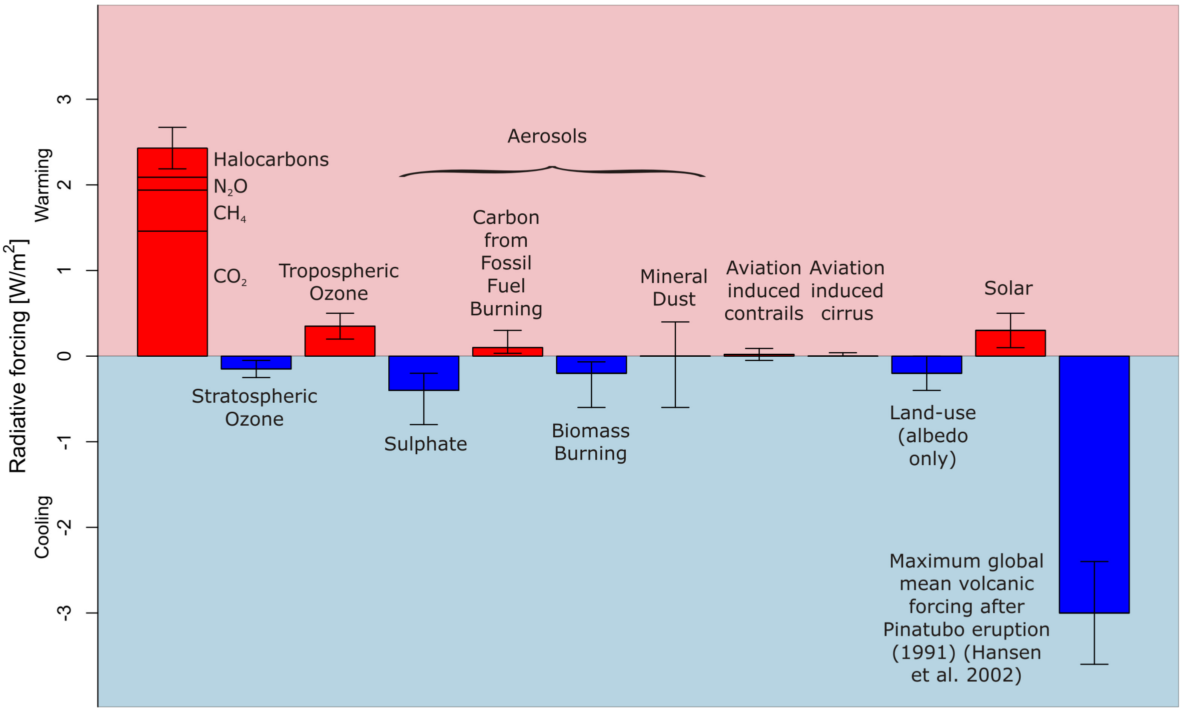

Figure 6.5: *Global, annual mean radiative forcings (Wm^{-2}) for the period from pre-industrial to present (1750–). The height of the rectangular bar denotes a central or best estimate value while its absence denotes no best estimate is possible. The vertical line about the rectangular bar indicates an estimate of the uncertainty range, guided by the spread in the published values of the forcing and physical understanding (IPCC 2001). The rightmost bar displays the estimated maximum global mean volcanic forcing following the Pinatubo eruption 1991 (Hansen et al. 2002) (drawn after McCormick et al. 1995).*

(Andronova et al. 1999) and the aerosol optical depth (Robertson et al. 2001) with the European summer temperature anomaly fields (not shown). This relationship turned out to be complex and difficult to assess. For most of the eruptions the maximum cooling in Europe does not occur at the same latitude as the maximum modelled net radiative forcing. A possible explanation is the major effect of the advective processes and transport of latent heat disturbing the relatively small regional differences of radiative forcing within Europe. An additional difficulty is given by the possible time lag between radiative forcing and surface temperature cooling (cf. section 6.2.1).

6.3 Indirect Dynamical Effects on the Atmospheric Circulation

6.3.1 Volcanic Effects on European Winter Temperature

The winter surface temperature response to tropical volcanic eruptions was a main issue of the research on volcanic forcing over the last decade. This resulted in various publications on this phenomenon based on observation, reconstruction and modelling studies. There are problems in comparing the results, as some authors accounted for the ENSO signals, which occurred simultaneously to several recent eruptions. In this study the El Niño effect is not removed (see section 4.4). Robock and Mao (1995) removed the ENSO signal by regression and revealed a large temperature difference in the tropical ocean, but virtually no difference all over Europe (see fig. 8 and 9 in Robock and Mao 1995) between the winter temperature composites with and without ENSO signal. Kodera (1994) calculated the difference between January temperature composites with an El Niño and a simultaneous volcanic signal, and Januaries with El Niño signal only. They showed that El Niño resulted in a cooling of the January temperatures over Europe, meaning that the El Niño would rather lead to a weakening of the volcano-induced post-eruption winter warming over Europe.

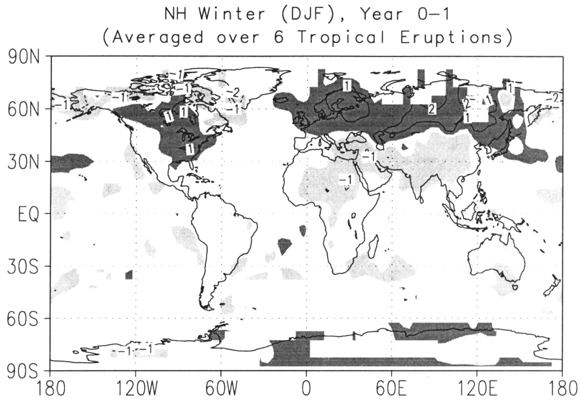

Figure 6.6: *Northern Hemisphere winter anomaly patterns for the first (left panel) and the second (right panel) winter after six tropical eruptions, after first removing the ENSO signal. Areas with anomalies < -0.25° C are shaded lightly and areas with anomalies > +0.25° C are shaded darkly. Contours are drawn with an interval of 1° C, with the 0° C contour not shown (Robock and Mao 1995).*

The lower panels in figure 5.3 show the composite European winter temperature in the first and second winter following 16 eruptions. The temperature pattern is dominated by a winter warming over Northern Europe in the first winter, and a more pronounced and extended warming over Northern and Central Europe and the northern Mediterranean during the second winter. The pronounced warming over Northern Europe and especially Fennoscandia is dominant in 13 of 16 of the second post-eruption winters (figure 5.6).

The winter warming response is consistent with the findings of various other publications. Figure 6.6 depicts the global temperature composite of the first (left panel) and the second (right panel) winter following six tropical eruptions over the period 1880–1995 composited by Robock and Mao (1995). Even though the number of composited eruptions in Robock and Mao (1995) is substantially smaller and they removed the ENSO-signal, the composite temperature field is in remarkably good agreement with our results for both the first and second winter. The warming in the first winter composite field covers the same regions and is of a similar magnitude (figure 6.6, left panel; figure 5.3, lower left panel). Both studies show a warming over Iceland in the first winter and no warming in the second winter. Weak negative anomalies in the second winter are located over southern Spain and over the Black Sea region in both composites. In contrast to our results, the warming over Northern Europe during the second winter (< 1°C) (figure 6.6, right panel) is smaller than in the first winter (> 1°C) (figure 6.6, right panel). The positive anomalies of the second winter calculated in this study reach up to 2°C and extend further south than presented in Robock and Mao (1995). The difference of the magnitude and the geographical extension can be explained by the different selection of the composited eruptions. Figure 5.6 reveals, that some of the eruptions prior to 1880, which are not included in Robock and Mao (1995), showed a very extended warming over Europe and resulted in the stronger positive anomalies in the composite field. However, it must be noted, that the temperature reconstructions for the 16th and 17th century are less reliable (cf. section 6.1).

The winter composite anomaly field by Kelly et al. (1996) averaging 5 winters following volcanic eruptions (cf. above) resembles the first winter anomaly composite in figure 5.3 (lower left panel). Over most parts of Europe positive anomalies are dominant, significant over northernmost Scandinavia. Again, in contrast to the rest of Europe a cooling is visible over Spain, the eastern Mediterranean and the Black Sea.

Kodera (1994) found similar results when compositing the three volcanic Januaries of 1992, 1983, 1964 (first winter), using data of the Japan Meteorological Agency. A maximum warming (> 2°C) over southern Scandinavia, the British Isles, the Baltic and northern Central Europe associated with a weak cooling over southern Spain and the Black Sea. The contrast between negative and positive anomalies is even enhanced when they subtracted the signal of the five El Niño Januaries 1966, 1970, 1973, 1977 and 1987. The warming in the first post-eruption January, shown in Kodera (1994), is stronger than in the first winter in this study. I suggest this difference is caused by the fact that Kodera (1994) averaged temperatures of only three Januaries and the role of the extraordinary winter warming 1991/92 (first winter after Pinatubo eruption) is dominant. The NCEP reanalysis of the winter 1991/1992 reveals positive temperature anomalies of more than 4°C! over Northern Europe (Stenchikov et al. 2002). Anomalies of the same magnitude can be found in the NCEP reanalysis of the following winter 1992/93 over the Northern Europe. The geographical distribution of the anomalies over Europe (NCEP reanalysis) for the two winters compares relatively well with our composite anomaly fields for the first and second winter following 16 eruptions during the past 500 years.

Summarised, it can be said, that the observational studies on the temperature response to major volcanic eruptions by Groisman (1992), Kodera (1994), Robock and Mao (1995) and Kelly et al. (1996) confirm the results of this study over the past 100 or 200 years. The highly resolved temperature reconstructions back to 1500, used in this study, offer more evidence on the regional temperature response to a large set of major eruptions further back in time. Figure 5.6 illustrates that the winter warming observed following the six most recent major eruptions, can be found after most of the previous major eruptions over the last five centuries. Exceptions are given by the second winter following the Cosiguina eruption 1835, showing no warming, and the second post-eruption winter of Serua 1692 and Krakatau 1883, when the warming is shifted to the south. However, the volcanic signal is overlapped by different other forcings and internal variability. Additionally, it has to be taken into consideration that the reliability of the temperature reconstructions is rapidly decreasing before 1700. A second uncertainty is the precise dating of some eruptions before 1700 such as Kelut, Ruiz, Gamkonora and Serua. Taking into account these problems the agreement of the 16 different post-eruption winter anomaly fields is highly remarkable.

Our results concerning the winter warming are consistent not only with observational studies but also with GCM studies, such as Graf et al. (1994), Hansen (1996), Kirchner et al. (1999), Graf (2002), Rozanov et al. (2002) and Stenchikov et al. (2002). Figure 6.7 illustrates the surface temperature anomaly simulated with volcanic forcing of the winter 1991/92 (first winter after Pinatubo 1991) with reference to ensemble runs without aerosol. The simulated distribution of the temperature anomalies in winter 1991/92 is similar to the composite post-eruption winter temperature distribution over the past five centuries. The positive anomalies are located over Scandinavia, the Baltic and the northern British Isles and the negative anomalies over southern Spain and the eastern Mediterranean. This pattern is in good agreement with the observations in the eastern Mediterranean during the first and second winter following the Pinatubo eruption 1991, suggesting winter temperature response opposite to the rest of Europe in winter. In both winters it was snowing in Jerusalem, a very unusual occurrence (Graf 2002). Large populations of corals at the bottom of the Red Sea died that winter (Genin et al. 1995), because the water at the surface cooled and convectively mixed the entire depth of the water. The enhanced supply of nutrients produced anomalously large algal and phytoplankton blooms, which smothered the coral (Robock 2000). This coral death

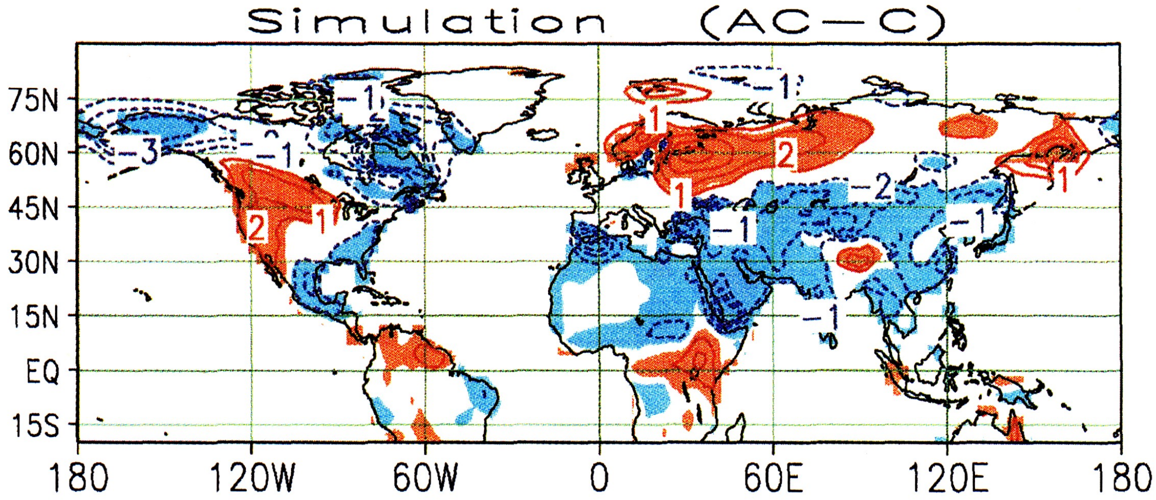

Figure 6.7: *Anomalies of the surface air temperature (Kelvin) in the winter (DJF) 1991–1992 simulated in the run with climatological sea surface temperature (SST) (shading corresponds to 10% confidence level). The simulated anomalies are calculated with respect to the ensemble runs without aerosol (Kirchner et al. 1999).*

had only happened before in winters following large volcanic eruptions (Genin et al. 1995). Looking at the global context of the anomaly distribution, Graf (2002) identified the temperature anomalies over the Mediterranean as part of a large-scale wave-like pattern in contrast to the cooling over the mid- and high-latitude continents, which would be expected due to the radiative forcing. This points to an explanation for the temperature distribution in changes of the atmospheric circulation, which will be discussed in the following section.

6.3.2 Changes in Sea Level Pressure and the Atmospheric Circulation

The winter warming patterns following volcanic eruptions are closely related to the tropospheric and stratospheric circulation. Perlwitz and Graf (1995) examined the observations of NH winter stratospheric and tropospheric circulation for the past 40 years and found that the dominant mode of circulation of the stratosphere is a strong polar vortex (polar night jet), which occurs simultaneously with a 500 hPa pattern with a low anomaly over Greenland and high anomalies over North America, Europe, and east Asia (Robock 2000). Perlwitz and Graf (1995) call this pattern the "baroclinic mode". The pattern strongly resembles the North Atlantic Oscillation (NAO) (Hurrell 1995, Wanner et al. 2001) and the Arctic Oscillation (AO) (Thompson and Wallace 1998, Thompson and Wallace 2000, Thompson et al. 2000).

The connection between stratospheric circulation and surface air temperature anomalies in the NH winter after a large tropical volcanic eruption is illustrated schematically in figure

6.8. The heating of the tropical lower stratosphere by absorption of terrestrial and solar near-infrared radiation expands that layer and produces an enhanced pole-to-equator temperature difference. The strengthened polar vortex traps the wave energy of the tropospheric circulation, and the stationary wave pattern known as the NAO dominates the winter circulation, producing the positive temperature anomalies (Robock 2000).

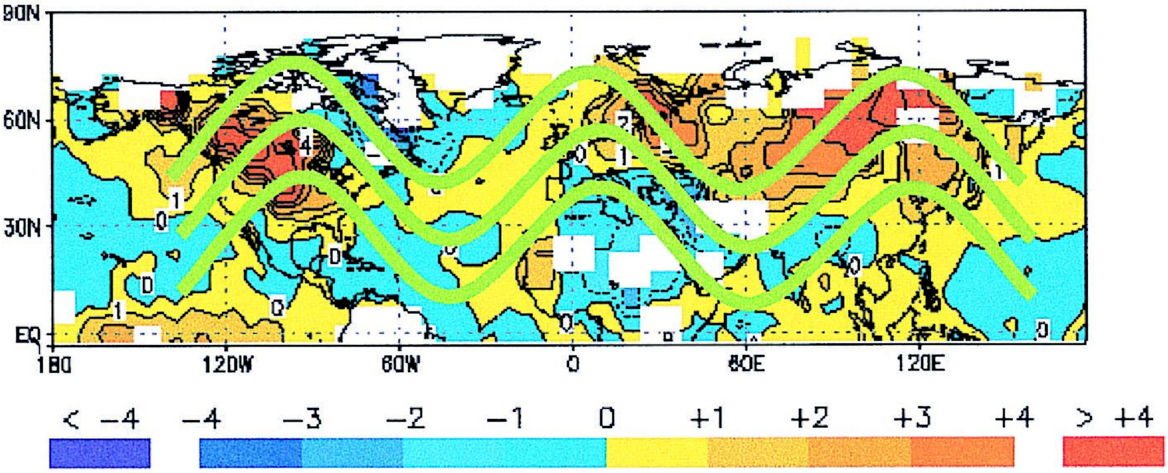

Figure 6.8: *Schematic diagram of how tropical lower stratospheric heating from volcanic aerosols produces the winter warming temperature pattern at the surface. The map at the bottom is surface air temperature anomalies (wrt 1961–1990) for the 1991–1992 NH winter (DJF) following the 1991 Mount Pinatubo eruption. The green curves indicate the anomalous tropospheric wind patterns responsible for horizontal advection that produced these temperature anomalies (Robock 2000). The data is provided by Jones and Briffa (1992).*

The post-eruption SLP and GPH_{500} anomaly fields of the second winter in figure 5.17 correspond relatively well with this theory. Both anomaly fields reveal an enhanced north-south gradient. This can be interpreted as the consequence of the strengthened polar vortex following tropical volcanic eruptions. In the composite absolute SLP and GPH_{500} fields of the second winter (not shown) a wave-like pattern can be observed. As mentioned above the SLP field of the second winter following the 16 eruptions, showing negative anomalies over Iceland and positive anomalies slightly north of the Azores, resembles the pressure field of a typical positive NAO mode. The large difference between north-western and south-western Europe on the 500 hPa level leads to enhanced geostrophic west winds. During winter the westerlies often transport warm and moist air over the European continent. The contours of the GPH_{500} anomaly field (figure 5.17) are latitude-parallel directed over the Atlantic, resulting in strong west winds directed towards the British Isles. Over the continent the isohypses turn to the north, triggering southwest winds over Scandinavia and the Baltic, exactly the region with the most pronounced surface temperature warming in the second winter. However, it has to be taken into consideration that the temperature reconstructions are not independent of the SLP and GPH_{500} reconstructions and are reconstructed using the same predictors. Moreover, it has to be taken into account that the composite anomaly field represents a mean state of a field, which could be characterised by large variability. The pressure response to the different eruptions is much less homogenous for the different eruptions than the temperature response. The location of the centres of positive and negative anomalies varies substantially between the different events. The majority of the post-eruption winters show an enhanced north-south pressure gradient.

Because of the high variability it is difficult to compare the composite pressure anomaly fields (this study) with other studies using a different set of eruptions and different definitions of the reference period. Taking this problems into account it can still be stated, that other authors found similar typical pressure fields in post-eruption winters. Kodera (1994) averaged the GPH_{500} fields over the Januaries 1964, 1983 and 1992 and calculated the difference to a composite of five El Niño Januaries over the same period. They found a wave-like pattern over Europe with a north-south gradient substantially stronger in post-eruption Januaries than in El Niño Januaries. The anomaly field shows most positive values over France and negative values over northernmost Scandinavia. Kelly et al. (1996) composited the SLP fields of the first winter following 5 eruptions (cf. above) using the same reference period as this study. They found significantly positive anomalies of about 3 hPa located over the Mediterranean and France and significantly negative values (-5 hPa) in a latitudinal band located around northern Scandinavia. The general pattern corresponds relatively well to our first winter composite of 16 eruptions (figure 5.15), even though the centre of positive anomalies is located much more to the east than in this study.

6.3.3 Volcanic Effects on the North Atlantic Oscillation (NAO)

As mentioned above the pressure anomaly fields of the second winter is similar to a positive NAO pattern. Composite analysis of the NAO index, reconstructed by Luterbacher et al. (2002a) over the past five centuries, was performed to investigate the significance of the post-eruption winter NAO following 16 tropical volcanic eruptions. The results are displayed in figure 5.18 and table 5.3. As expected the winter NAO is found to be significantly positive in the second winter following volcanic eruptions. It is remarkable that the NAO index of the second winter was positive after 14 of 16 eruptions. In one case the index was strongly positive in the first and negative in the second winter. These results offer more evidence for the mechanisms describing a forced positive winter NAO pattern following tropical eruptions (cf. 6.3.2). However, these findings need to be confirmed as there are different objections. In contrast to our results no significant change can be found, performing the same analysis with the NAO index reconstructed by Cook et al. (2002). Furthermore it is irritating that the NAO index (Luterbacher et al. 2002a) is again significantly positive in the fourth winter, and significantly negative in the fifth winter, although there seems to be no physical explanation. In two cases the positive mode in the fourth winter is possibly a signal of the Tarawera (1886, VEI=5) and Awu (1966, VEI=4) eruption, three years after the Krakatau and Agung eruption. I suppose that a second eruption, following only three years after another, results in a faster circulation change due to the remaining stratospheric aerosols of the previous eruption. It should be noted, that other forcings can also result in a similar circulation response. One forcing, causing circulation changes, is the 11-year solar cycle, as the 11-year cycle in ultraviolet flux and ozone amount combine to produce anomalous stratospheric heating and circulation (Kodera et al. 1991, Haigh 1996, Robock 1996, Shindell et al. 1999). Another forcing is simply global warming, which increases the thickness of the troposphere in the tropics more than at higher latitudes, also enhancing the pole-to-equator gradient (Graf et al. 1995).

6.4 Volcanic Effects on Precipitation

The volcanic effects on precipitation are very poorly investigated. Robock and Liu (1994) analysed the volcanic signal in GCM simulations and found reduced tropical precipitation for 1–2 years following large eruptions. The global hydrological cycle is fuelled by evaporation, and the cooling after the eruptions produced this effect (Robock 2000). Robock and Liu (1994) also found a reduction in Sahel precipitation that matched the observed enhancement of the Sahel drought following the El Chichon eruption. No significant changes were found over Europe.

Portman and Gutzler (1996) analysed volcanic effects on monthly total precipitation over the USA by compositing data of the U. S. Historical Climatology Network over the 20th century. They found positive monthly precipitation anomalies exceeding 15 mm in magnitude in the south-eastern United States during the first winter and spring after eruptions. Precipitation anomalies that are smaller in magnitude and yet significant, such as positive anomalies in the north-western United States and negative anomalies in the central and eastern United States, were found during the summer of the first post-eruption calendar year (Portman and Gutzler 1996). However, the presence of apparently significant anomalies beginning before, as well as a few years after eruptions suggests that the sample sizes were to small to yield robust composite volcanic signals (Portman and Gutzler 1996).

I experienced similar difficulties when analysing the composite precipitation anomaly fields displayed in figure 5.19. The precipitation anomalies in first and second post-eruption summer and winter are all of small magnitudes and show no homogenous pattern. The strongest negative anomalies can be observed in the first summer. These dry conditions might be related to reduced evaporation, due to summer cooling. However, the standard deviations are large and there is no explanation for the positive anomalies over other parts of Europe. Much more evidence is required to understand this mechanism. The wet conditions over Fennoscandia and the British Isles, Iceland and the French west coast during the second winter can be interpreted as a result of the enhanced westerlies transporting warm moist air over the continent resulting in more winter precipitation. Again the anomalies are not significant and the connection has to be proved. It has to be taken into account that the reliability of the precipitation is rapidly decreasing back in time (cf. section 6.1). In late autumn 2003, there will be a new release of the precipitation reconstructions, with which these results can be compared.

Humphreys (1940) and others have suggested that volcanic aerosols settling from the upper troposphere may act as cloud condensation nuclei, thereby enhancing or reducing regional rainfall amounts. However, a more likely source of changes in precipitation is a large-scale dynamical perturbation of the atmospheric circulation patterns (Portman and Gutzler 1996). Such a perturbation could be related, for example, to differential surface cooling.

6.5 Duration of the Volcanic Perturbations and Timing of the Maximum Effect

Composite analysis of post-eruption summer and winter temperature, SLP, GPH_{500} and NAO index revealed maximum anomalies in the second summer and winter. As discussed above this corresponds to the summer and winter following between 13 and 24 months after an eruption depending on the date of the eruption. It would be desirable to average eruptions, which occurred during the same season of the year, to precisely determine the timing of the maximum effect. After comparing the anomaly fields qualitatively, I hypothesise, that the maximum response happens in the summer or winter between 9 and 15 months after the eruption. An example is the extraordinary cold summer 1816, following 14 months after the maximum of the Tambora eruption. Kelly et al. (1996) identified the strongest global cooling over a 2-year period starting early in the year after the eruption. Robock and Mao (1995) found the maximum cooling to occur approximately one year after the eruption. For the winter signal Robock and Mao (1995) revealed a persistence of the winter warming effect over Eurasia in the first and second winter and Groisman (1992) examined 2-year or 3-year average patterns of warming over Eurasia after large eruptions. The climate response during the third to fifth years will be discussed in the next section.

6.6 Reversal of the Volcanic Response in the Opposite Conditions

Adams et al. (2003) reevaluated the statistical connection between the timing of explosive volcanic eruptions and El Niño events by analysing two different reconstructions of El Niño activity and two independent chronologies of volcanic activity. They suggested the presence of a significant, multi-year, El Niño-like response to explosive tropical eruptions in past centuries, leading to roughly a doubling of the probability of observing an El Niño event in the first winter following the event. In the fourth, fifth and sixth post-eruption year a significant rebound into La Niña-like conditions was found, suggesting that the volcanic forcing tends to set up and pace a pattern of El Niño/La Niña-like alteration, before the response to the event appears to finally be damped out by internal noise. This finding is independent of previous analyses based on the restricted instrumental climate record (Adams et al. 2003). I used the same method to analyse the multi-year response of the summer and winter temperature and winter NAO to 16 tropical volcanic eruptions over the past 500 years (cf. figure 5.9, 5.10 and 5.18). For all parameters a similar reversal of the primary response of first years to opposite conditions in the third, fourth or fifth year can be found. The highly significant summer cooling in the second summer returns to a weak warming in the third and a significant warming in the fourth summer. Figure 5.11 shows the spatial pattern over Europe and reveals positive anomalies in the fourth summer mainly over France, Spain and Germany. The winter warming in the first and second year changes to a highly significant cooling in the fifth year. It is remarkable, that the cooling in the fifth winter occurred over the same regions as the warming in the second winter (cf. figure 5.12). The anomaly field of the fifth winter corresponds to a nearly opposite pattern of the second winter. In general, an annual oscillation of warm and cold conditions can be observed from the second to the fifth post-eruption winter. A very similar annual alteration can be observed in the composite analysis of the NAO index, displayed in figure 5.18.

The overlapping of different forcings and the complexity of feedback mechanisms in the atmosphere/ocean interactions allow no explanation for these phenomena with our methods. The El Niño/La Niña-like alteration was simulated in GCM studies and is consistent with recently proposed mechanisms for the response of tropical Pacific coupled ocean-atmosphere dynamics to an imposed radiative forcing anomaly (Adams et al. 2003). No similar mechanism is known for the alteration in the NAO. My results suggest that the winter NAO alteration is associated to the changes in the winter temperature. Although the two parameters are not reconstructed independently, this could point to a connection of the post-eruption alteration with changes in the stratospheric pole-equator temperature gradient. GCM studies would be required for a better understanding of these mechanisms.

Chapter 7

Conclusions

The aim of this study is a better understanding of the European climate response to volcanic eruptions over the past five centuries. In order to achieve this goal a new compilation of temperature, precipitation and pressure reconstructions for the North Atlantic / European region was analysed. The study focuses on the timing, the magnitude and spatial distribution of the volcanic response within Europe.

The conclusions can be summarised as follows:

- Major volcanic eruptions result in a cooling of the average summer temperature over the European land regions in the first and the second post-eruption summer. This can be explained by radiative cooling due to scattering by stratospheric aerosols. It has been shown that the maximum cooling in the European average temperature of about -0.4°C often occurred during the second summer following large eruptions.

- The European winter average temperature response to tropical eruptions reveals a significant warming effect with its maximum in the second post-eruption winter. I assume that this reflects a dynamic response to the strengthening of the equator-to-pole temperature gradient in the lower stratosphere, caused by radiative heating of the aerosol layer in the tropics.

- The summer and winter temperature response has been found to be very consistent after all 16 major eruptions over the last 500 years, especially in the second post-eruption winter and summer. This suggests a dominant role of the volcanic forcing compared to other radiative forcings during the two years following major eruptions.

- There are large regional differences in the temperature response over Europe. The strongest cooling effect during summer tends to occur over Northern and Central Europe, whereas over the Mediterranean no effect can be noticed. The winter warming is shown to be most pronounced over Northern Europe (more than 2°C). Somewhat cooler conditions are observed over the eastern and western Mediterranean.

- The pressure response is characterised by large variability between the different eruptions. In general the sea level pressure and the geopotential height fields indicate negative anomalies over Northern Europe and positive anomalies over Southern Europe. The north-south pressure gradient is most distinct over Western Europe and the eastern North Atlantic resulting in enhanced geostrophic west winds over the European west coast and southwest winds over Northern Europe. The geostrophic winds could be the explanation for the pronounced winter warming over Northern Europe. This relationship needs to be confirmed with independent (not sharing the same predictors) pressure and temperature reconstructions.

- The SLP pattern observed in the second winter following 16 eruptions resembles a strongly positive NAO mode. The analysis of a winter NAO index reconstruction suggests a significant positive NAO response to major tropical eruptions during the second post-eruption winter. This finding is consistent with a recent GCM study (Stenchikov et al. 2002) presenting a plausible mechanism of AO response to large tropical eruptions.

- The results, reported in the present study, suggest a reversal of the primary response of the winter NAO index and summer and winter temperature to opposite conditions in the third, fourth or fifth year. A similar alteration following major eruptions was found in the El Niño Southern Oscillation (ENSO). In contrary to the ENSO, no atmospheric circulation mechanism is known to explain the alteration of temperature and the winter NAO in post-eruption years. Moreover the signal after the second year seems to be strongly influenced by different other forcings and internal variability. The method used in this study is not suitable to account for the different overlapping radiative forcing and therefore allows no robust results on the volcanic signal after the second post-eruption year.

- The effects of volcanic eruptions on seasonal precipitation are revealed to be complex and much less pronounced than on the other parameters. It is apparent that changes in the atmospheric circulation could also lead to precipitation anomalies. The wet conditions at the European west coasts during the second post-eruption winter associated with enhanced westerlies could indicate such a connection. However, these parameters were not reconstructed independently and the precipitation anomalies are not significant.

- The climate response to eruptions is dependent on the latitude of the volcano. Especially the winter temperature response is shown to differ between high-latitudinal and tropical eruptions.

- The analysis of highly resolved climate reconstructions offer extended scientific understanding on the regional to continental response to volcanic eruptions. The achieved results attest the method a large potential of determining the volcanic effects on different climatic parameters, their timing and spatial distribution. However, the following limitations are revealed as well. The detection of a significant volcanic signal is possible only as long as the volcanic radiative forcing is large enough (i.e. about two post-eruption years). Furthermore the method offers no direct evidence on the atmospheric mechanisms causing the volcanic response. Only combined with model simulations the method provides optimal skills for an integrated understanding of volcanic effects on climate.

Chapter 8

Outlook

There is a lot of further work that has to be done to evaluate the climate response to volcanic eruptions. In a next step the data quality (RE values) should be included in the analysis to estimate the reliability of the results for the different regions and time periods. It would be desirable to perform the same analysis with independent climate reconstructions for all climate parameters which would allow to establish causal connections between the different parameters. This is an aim of the PALVAREX project within the NCCR Climate and will be conducted by Casty (2004, in prep.). Moreover, the study area could be extended to have a better spatial coverage, which would allow to interpret the European climate response in a global context. A longer record of high-quality reconstructions would allow a more robust determination of the volcanic signal due to the larger set of major volcanic episodes. If analysing further back in time the quality of the reconstructions and the accuracy of the dating of the volcanic eruptions become the limiting factors. It is not promising to include minor eruptions of the past 500 years in the composite analysis to increase the number of averaged volcanoes, as their signal is weaker and could be damped out by other forcings and uncertainties of the earlier reconstructions.

In this study the non-volcanic components are not removed by filtering. I try to account for the different other forcings and internal variability by compositing a relatively large set of eruptions. However, it would be desirable to extract the volcanic signal out of the different climatic parameters. Hence, other radiative forcings, such as solar and greenhouse gas forcing, and mechanisms such as the ENSO, should be precisely reconstructed.

GCM studies offer extended insight in the climate response to the different radiative forcings. It would be therefore especially promising to compare the results of this study with highly resolved model simulations using the same dating of volcanic eruptions, which are currently under investigation at the NCAR (C. Ammann, personal communication).

References

Adams, J. B., M. E. Mann, and C. Ammann (2003). Re-examining the 'Volcano-El Niño' hypothesis using paleoclimate information. *Nature*, In review.

Ammann, C. M., G. A. Meehl, W. M. Washington, and C. S. Zender (2003). A Monthly and Latitudinally Varying Volcanic Forcing Dataset in Simulations of 20th Century Climate. *Geophysical Research Letters* **30** (12), doi:10.1029/2003GL016875.

Ammann, C. M. and P. Naveau (2003). Statistical analysis of tropical explosive volcanism occurrences over the last 6 centuries. *Geophysical Research Letters* **30** (5), doi:10.1029/2002GL016388.

Andronova, N. G., E. V. Rozanov, F. Yang, and M. E. Schlesinger (1999). Radiative forcing by volcanic aerosols from 1850 to 1994. *Journal of Geophysical Research* **104** (D14), 16807–16826.

Angell, J. K. and J. Korshover (1985). Surface Temperature Changes Following the Six Major Volcanic Episodes Between 1780 and 1980. *Journal of Climate and Applied Meteorology* **24** (9), 937–951.

Bertrand, C., J.-P. van Ypersele, and A. Berger (1999). Volcanic and solar impacts on climate since 1700. *Climate Dynamics* **15**, 355–367.

Bluth, G. J. S., S. D. Doiron, S. C. Schnetzler, A. J. Krueger, and L. S. Walter (1992). Global tracking of the SO_2 clouds from the June 1991 Mount Pinatubo eruptions. *Geophysical Research Letters* **19**, 151–154.

Bradley, R. S. (1988). The Explosive Volcanic Eruption Signal in Northern Hemisphere Continental Temperature Records. *Climatic Change* **12**, 221–243.

Briffa, K. R., P. D. Jones, F. H. Schweingruber, and T. J. Osborn (1998). Influence of volcanic eruptions on Northern Hemisphere summer temperature over the past 600 years. *Nature* **393**, 450–455.

Casty, C. (2004). In preparation.

Chenoweth, M. (1996). Ships' Logbooks and "The Year Without a Summer". *Bulletin of the American Meteorological Society* **77** (9), 2077–2093.

Cook, E. R., R. D. D'Arrigo, and M. E. Mann (2002). Multiproxy Reconstruction of the Winter North Atlantic Oscillation Index since A.D. 1400. *Journal of Climate* **15**, 1754–1764.

Crowley, T. J. (2000). Causes of Climate Change Over the Past 1000 Years. *Science* **289**, 270–277.

Crowley, T. J. and K.-Y. Kim (1999). Modelling the temperature response to forced climate change over the last six centuries. *Geophysical Research Letters* **26** (13), 1901–1904.

de Boer, J. Z. and D. T. Sanders (2002). *Volcanoes in Human History: The Far-Reaching Effects of Major Eruptions.* Princeton University Press, Princeton and Oxford.

Duchon, C. E. (1979). Lanczos filtering in one and two dimensions. *Journal of Applied Meteorology* **18**, 1016–1022.

Forsyth, P. Y. (1988). In the wake of Etna, 44 B. C.. *Classical Antiquity*, 49–57.

Franklin, B. (1784). Meteorological imaginations and conjectures. *Manchester Literary and Philosophical Society Memoirs and Proceedings* **2** (122), (Reprinted in Weatherwhise, 35, 262, 1982.).

Genin, A., B. Lazar, and S. Brenner (1995). Vertical mixing and coral death in the Red Sea following the eruption of Mount Pinatubo. *Nature* **377**, 507–510.

Graf, H. (2002). Klimaänderungen durch Vulkane. *promet* **28** (3/4), 133–138.

Graf, H.-F., J. Perlwitz, and I. Kirchner (1994). Northern hemisphere tropospheric midlatitude circulation after violent volcanic eruptions. *Contributions to Atmospheric Physics* **67**, 3–13.

Graf, H.-F., J. Perlwitz, I. Kirchner, and I. Schult (1995). *Atmospheric Ozone As a Climate Gas.*, Chapter On the interrelationship between recent climate trends, ozone change and increased greenhouse gas forcing., pp. 163–179. Springer-Verlag, New York.

Groisman, P. Y. (1992). Possible regional consequences of the Pinatubo eruption. *Geophysical Research Letters* **19** (15), 1603–1606.

Haigh, J. (1996). The impact of solar variability on climate. *Science* **272**, 981–984.

Hansen, J. (1996). *Global Environment Change.*, Chapter A Pinatubo climate modelling investigation., pp. 233–272. Number 42 in NATO ASI Series.

Hansen, J., I. Fung, A. Lacis, D. Rind, S. Lebedeff, R. Ruedy, G. Russell, and P. Stone (1988). Global climate changes as forecast by the Goddard Institute for Space Studies three-dimensional model. *Journal of Geophysical Research* **93**, 9341–9364.

Hansen, J., M. Sato, L. Nazarenko, R. Ruedy, A. Lacis, D. Koch, I. Tegen, T. Hall, D. Shindell, B. Santer, P. Stone, T. Novakov, L. Thomason, R. Wang, Y. Wang, D. Jacob, S. Hollandsworth, L. Bishop, J. Logan, A. Thompson, R. Stolarski, J. Lean, R. Willson, S. Levitus, J. Antonov, N. Rayner, D. Parker, and J. Christy (2002). Climate forcings in Goddard Institute for Space Studies SI2000 simulations. *Journal of Geophysical Research* **107** (D18), doi:10.1029/2001JD001143.

Harshvardhan (1979). Perturbations of the zonal radiation balance by stratospheric aerosol layer. *Journal of Atmospheric Science* **36**, 1274–1285.

Humphreys, W. J. (1913). Volcanic dust and other factors in the production of climatic changes, and their possible relation to ice gases. *J. Franklin Institute*, 131–172.

Humphreys, W. J. (1940). *Physics of the Air.* Dover, Mineola, New York.

Hurrell, J. W. (1995). Decadal trends in the North Atlantic Oscillation: Regional temperatures and precipitation. *Science* **269**, 676–679.

IPCC (2001). *Climate Change 2001: The Scientific Basis. Contribution of Working Group I to the Third Assessment Report of the Intergovernmental Panel on Climate Change.*, pp. 881. Cambridge University Press, Cambridge, United Kingdom and New York, NY, USA.

Jones, P. D. and K. R. Briffa (1992). Global surface air temperature variations during the twentieth century: Part 1, spatial, temporal and seasonal details. *The Holocene* **2**, 165–179.

Jones, P. D., T. M. L. Wigley, and G. Farmer (1991). *Greenhouse-gas-induced Climatic Change: a Critical Appraisal of Simulations and Observations.*, Chapter The volcanic contribution to climate change of the past 100 years., pp. 153–172. Elsevier, Amsterdam.

Kalnay, E., M. Kanamitsu, R. Kistler, W. Collins, D. Deaven, L. Gandin, M. Iredell, S. Saha, G. White, J. Woollen, Y. Zhu, A. Leetmaa, R. Reynolds, M. Chelliah, W. Ebisuzaki, W.Higgins, J. Janowiak, K. C. Mo, C. Ropelewski, J. Wang, R. Jenne, and D. Joseph (1996). The NCEP/NCAR 40-Year Reanalysis Project. *Bulletin of the*

American Meteorological Society **77** (3), 437–471.

Kelly, P. M., P. D. Jones, A. Robock, and K. R. Briffa (1998). The contribution of Hubert H. Lamb to the study of volcanic effects on climate. *Weather* **53**, 209–222.

Kelly, P. M., J. Pengqun, and P. D. Jones (1996). The spatial response of the climate system to explosive volcanic eruptions. *International Journal of Climatology* **16**, 537–550.

Kelly, P. M. and C. B. Sear (1984). Climatic impact of explosive volcanic eruptions. *Nature* **311**, 740–743.

Kirchner, I. and H. F. Graf (1995). Volcanoes and El Niño: Signal separation in Northern Hemisphere winter. *Climate Dynamics* **11**, 341–358.

Kirchner, I., G. L. Stenchikov, H. F. Graf, A. Robock, and J. C. Antuña (1999). Climate model simulation of winter warming and summer cooling following the 1991 Mount Pinatubo volcanic eruption. *Journal of Geophysical Research* **104** (D16), 19039–19055.

Kistler, R., E. Kalnay, W. Collins, S. Saha, G. White, J. Woollen, M. Chelliah, W. Ebisuzaki, M. Kanamitsu, V. Kousky, H. van den Dool, R. Jenne, and M. Fiorino (2001). The NCEP/NCAR 50-Year Reanalysis. *Bulletin of the American Meteorological Society* **82** (2), 247–267.

Kodera, K. (1994). Influence of volcanic eruptions on the troposphere through stratospheric dynamical processes in the Northern Hemisphere winter. *Journal of Geophysical Research* **99**, 1273–1282.

Kodera, K., M. Chiba, and K. Shibata (1991). A general circulation model study of the solar and QBO modulation of the stratospheric circulation during the Northern Hemisphere winter. *Geophysical Research Letters* **18**, 1209–1212.

Lamb, H. H. (1970). Volcanic dust in the atmosphere, with a chronology and assessment of its meteorological significance. *Philosophical Transactions of the Royal Society of London. Series A, Mathematical and Physical Sciences* **266** (1178), 425–533.

Lamb, H. H. (1977). Supplementary volcanic dust veil index assessments. *Climate Monitor* **6**, 57–67.

Lamb, H. H. (1983). Update of the chronology of assessments of the volcanic dust veil index. *Climate Monitor* **12**, 79–90.

Lorenz, E. N. (1956). Empirical Orthogonal Functions and Statistical Weather Prediction. Statistical forecasting project report no. 1, contract af 19, M.I.T.

Luterbacher, J., D. Dietrich, H. Wanner, and E. Xoplaki (2003). European temperature variability over the last 500 years, uncertainties, extremes. Submitted.

Luterbacher, J., R. Rickli, E. Xoplaki, C. Tinguely, C. Beck, C. Pfister, and H. Wanner (2001). The Late Maunder Minimum (1675-1715) – A Key Period for Studying Decadal Scale Climatic Change in Europe. *Climatic Change* **49**, 441–462.

Luterbacher, J., E. Xoplaki, D. Dietrich, P. D. J. T. D. Davies, J. F. Conzalez-Rouco, H. von Storch, D. Gyalistras, C. Casty, and H. Wanner (2002a). Extending North Atlantic Oscillation Reconstructions Back to 1500. *Atmospheric Science Letters* **2**, 114–124.

Luterbacher, J., E. Xoplaki, D. Dietrich, R. Rickli, J. Jacobeit, C. Beck, D. Gyalistras, C. Schmutz, and H. Wanner (2002b). Reconstruction of sea level pressure fields over the Eastern North Atlantic and Europe back to 1500. *Climate Dynamics* **18**, 545–561.

Mann, M. E., R. S. Bradley, and M. K. Hughes (1998). Global-scale temperature patterns and climate forcing over the past six centuries. *Nature* **392**, 779–787.

Mao, J. and A. Robock (1998). Surface Air Temperature Simulations by AMIP General Circulation Models: Volcanic and ENSO Signals and Systematic Errors. *Journal of Climate* **11**, 1538–1552.

Mass, C. F. and D. A. Portman (1989). Major volcanic eruptions and climate: A critical evaluation. *Journal of Climate* **2**, 566–593.

McCormick, M. P., L. W. Thomason, and C. R. Trepte (1995). Atmospheric effects of the Mt Pinatubo eruption. *Nature* **373**, 399–404.

Minnis, P., E. F. Harrison, L. L. Stowe, G. G. Gibson, F. M. Denn, D. R. Doelling, and W. L. Smith (1993). Radiative climate forcing by the Mount Pinatubo eruption. *Science* **259**, 1411–1415.

Mitchell, J. M. (1961). Recent secular changes of the global temperature. *Annals of the New York Academy of Sciences* **95**, 235–250.

Mitchell, J. M. (1970). A preliminary evaluation of atmospheric pollution as a cause of the global temperature fluctuation of the past century. pp. 139–155.

New, M., M. Hulme, and P. D. Jones (2000). Representing Twentieth-Century Space-Time Climate Variability. Part II: Development of 1901-96 Monthly Grids of Terrestrial Surface Climate. *Journal of Climate* **13** (13), 2217–2238.

Newhall, C. G. and S. Self (1982). The volcanic explosivity index (VEI): An estimate of explosive magnitude for historical volcanism. *Journal of Geophysical Research* **87**, 1231–1238.

Parker, D. E., H. . Wilson, P. D. Jones, J. R. Christy, and C. K. Folland (1996). The impact of Mount Pinatubo on world-wide temperatures. *International Journal of Climatology* **16**, 487–497.

Perlwitz, J. and H.-F. Graf (1995). The statistical connection between tropospheric and stratospheric circulation of the northern hemisphere in winter. *Journal of Climate* **8**, 2281–2295.

Plinius, C. (109). *Epistulae. Liber VI.*

Portman, D. and D. Gutzler (1996). Explosive volcanic eruptions, the El Ninõ-Southern Oscillation, and U.S. climate variability. *Climatic Change* **9**, 17–33.

Preisendorfer, R. W. (1988). *Principal Component Analysis in Meteorology and Oceanography.* Elsevier, Amsterdam.

Ramachandran, S., V. Ramaswamy, G. L. Stenchikov, and A. Robock (2000). Radiative impact of the Mount Pinatubo volcanic eruption: Lower stratospheric response. *Journal of Geophysical Research* **105**, 24409–24429.

Robertson, A., J. Overpeck, D. Rind, E. Mosley-Thompson, G. Zielinski, J. Lean, D. Koch, J. Penner, I. Tegen, and R. Healy (2001). Hypothesized climate forcing time series for the last 500 years. *Journal of Geophysical Research* **106** (D14), 14783–14803.

Robock, A. (1991). *Greenhouse-Gas-Induced Climatic Change: A Critical Appraisal of Simulations and Observations*, Chapter The volcanic contribution to climate change of the past 100 years, pp. 429–444. Elsevier Sci., New York.

Robock, A. (1996). Stratospheric control of climate. *Science* **272**, 972–973.

Robock, A. (2000). Volcanic eruptions and climate. *Review of Geophysics* **38** (2), 191–219.

Robock, A. and M. P. Free (1995). Ice cores as an index of global volcanism from 1850 to the present. *Journal of Geophysical Research* **100** (D6), 11549–11567.

Robock, A. and M. P. Free (1996). *Climatic Variations and Forcing Mechanisms of the Last 2000 Years*, Chapter The volcanic record in ice cores for the past 2000 years. Springer-Verlag, New York.

Robock, A. and Y. Liu (1994). The volcanic signal in Goddard Institute for Space Studies three-dimensional model simulations. *Journal of Climate* **7**, 44–55.

Robock, A. and J. Mao (1992). Winter warming from large volcanic eruptions. *Geophysical Research Letters* **19**, 2405–2408.

Robock, A. and J. Mao (1995). The volcanic signal in Surface Temperature Observations. *Journal of Climate* **8**, 1086–1103.

Robock, A. and C. Mass (1982). The Mount St. Helens Volcanic Eruption of 18 May 1980: Large Short-Term Surface Temperature Effects. *Science* **216** (4546), 628–630.

Rozanov, E. V., M. E. Schlesinger, N. G. Andronova, F. Yang, S. L. Malyshev, V. A. Zubov, T. A. Egorova, and B. Li (2002). Climate/chemistry effects of the Pinatubo volcanic eruption simulated by the UIUC stratosphere/troposphere GCM with interactive photochemistry. *Journal of Geophysical Research* **107**, doi:10.1029/2001JD000974.

Sapper, K. (1917). Beiträge zur Geographie der tätigen Vulkane. *Zeitschrift für Vulkanologie*, 65–197.

Sapper, K. (1927). *Vulkankunde.* Englehorn Verlag, Stuttgart, Germany.

Sato, M., J. E. Hansen, M. P. McCormick, and J. B. Pollack (1993). Stratospheric Aerosol Optical Depths, 1850-1990. *Journal of Geophysical Research* **98** (D12), 22987–22994.

Sear, C. B., P. M. Kelly, P. D. Jones, and C. M. Goodess (1987). Global surface-temperatures responses to major volcanic eruptions. *Nature* **330**, 365–367.

Sedlacek, W. A., E. J. Mroz, A. L. Lazrus, and B. W. Gandrud (1983). A Decade of Stratospheric Sulphate Measurements Compared With Observations of Volcanic Eruptions. *Journal of Geophysical Research* **88** (C6), 3741–3776.

Shapiro, S. S. and M. B. Wilk (1965). An analysis of variance test for normality (complete samples). *Biometrika* **52**, 591–611.

Shindell, D., D. Rind, N. Balachandran, J. Lean, and P. Lonergan (1999). Solar cycle variability, ozone, and climate. *Science* **284**, 305–308.

Simkin, T. and L. Siebert (1994). *Volcanoes of the World, 2nd ed.* Geoscience Press, Tucson, Arizona.

Simkin, T. and L. Siebert (2003). *Volcanoes of the World: An Illustrated Catalog of Holocene Volcanoes and their Eruptions.* Smithsonian Institution, Global Volcanism Program Digital Information Series, GVP-3.

Song, J. (1998). Reconstruction of the Southern Oscillation from dryness/wetness in China for the last 500 years. *International Journal of Climatology* **18**, 1345–1355.

Stenchikov, G. I., I. Kirchner, A. Robock, H.-F. Graf, J. C. Antuña, R. G. Grainger, A. Lambert, and L. Thomason (1998). Radiative forcing from the 1991 Mount Pinatubo volcanic eruption. *Journal of Geophysical Research* **103** (D12), 13837–13857.

Stenchikov, G. I., A. Robock, V. Ramaswamy, M. D. Schwarzkopf, K. Hamilton, and S. Ramachandran (2002). Arctic Oscillation response to the 1991 Mount Pinatubo eruption: Effects of volcanic aerosols and ozone depletion. *Journal of Geophysical Research*, doi:10.1029/2002JD002090.

Stothers, R. B. (1984). The great Tambora eruption in 1815 and its aftermath. *Science* **224**, 1191–1198.

Stothers, R. B. (1996). Major optical depth perturbations to the stratosphere from volcanic eruptions: The pyrheliometric period, 1881–1969. *Journal of Geophysical Research* **101**, 3901–3920.

Thompson, D. W. J. and J. M. Wallace (1998). The Arctic Oscillation signature in the wintertime geopotential height and temperature fields. *Geophysical Research Letters* **25**, 1297–1300.

Thompson, D. W. J. and J. M. Wallace (2000). Annular modes in the extratropical circulation, part I, Month-to-month variability. *Journal of Climate* **13**, 1000–1016.

Thompson, D. W. J., J. M. Wallace, and G. C. Hegerl (2000). Annular modes in the extratropical circulation, part II, Trends. *Journal of Climate* **13**, 1018–1036.

Trenberth, K. and D. A. Paolino (1980). The Northern Hemisphere sea level pressure data set: trends, errors and discontinuities. *Monthly Weather Review* **108**, 855–872.

von Storch, H. and F. W. Zwiers (1999). *Statistical Analysis in Climate Research.* Cambridge University Press.

Wanner, H., S. Brönnimann, C. Casty, D. Gyalistras, J. Luterbacher, C. Schmutz, D. B. Stephenson, and E. Xoplaki (2001). North Atlantic Oscillation - Concepts and Studies. *Surveys in Geophysics* **22** (4), 321–381.

Wanner, H., D. Gyalistras, J. Luterbacher, R. Rickli, E. Salvisberg, and C. Schmutz (2000a). Klimawandel im Schweizer Alpenraum.

Wanner, H., H. Holzhauser, C. Pfister, and H. Zumbühl (2000b). Interannual to centennial scale climate variability in the European Alps. *Erdkunde* **54**, 62–69.

Wilks, D. S. (1995). *Statistical Methods in the Atmospheric Sciences.* Academic Press, San

Diego.

Yarnal, B. (1992). *Synoptic climatology in environmental analysis.* Belhaven Press, London and Florida.

Zielinski, G. A. (2000). Use of paleo-records in determining variability within the volcanism-climate system. *Quaternary Science Review* **19**, 417–438.

Appendix A

Additional Data

Table A.1: *Eruption list derived from ice cores, see Ammann et al. (2003) for details.*

Year	Volcano	Lat	Lon	VEI	NHem-Ice	SHem-Ice	Dust Veils
1443	? Soufriere de Guadeloupe (C-14c: 1440)	16.05	61.7W	P	I,R	I,Co	
1452	Kuwae, Vanuatu	-16.8	168.5E	6	I,C,R?,Lw	I,Co,Lw	
1459	? Pele,W-Indies	14.82	61.17	?	I,G,C,R,Lw	I	
1463	? Kelut, Java	-8.0	112.3E	3	I,R	I	
?1490	? unknown	trop		?	I	I	
?1504	? Atitlan, Guatemala	14.58	91.2W	3?	C,R	Co?	L
1512	? Sangeang Api, Sunda	-8.18	119.1E	3			
	? Gunungapi Wetar, Banda	-6.64	126.7E	3	G?,R	I	
1522	? Santa Ana, El Salvador	13.85	89.6W	3			
	? Arenal, Costa Rica (C-14: 1525)	10.46	84.7W	4	I	I,M	
1554	? Merapi, Java	-7.54	110.4E	3	I,G?,R,A	Co?,M?	L
1568	? Savo, Salomon Islands	-9.13	159.8E	3			
	? Billy Mitchell (C-14: 1580)	-6.09	155.2E	6	I,G?	I	
1571	? unknown	trop		?	I,G,C	Co?	
1586	Kelut, Java	-8.0	112.3E	5?	I,G,C,R	I,Co?	L
1595	Raung, Java	-8.1	114.0E	5?			
	Ruiz, Colombia	4.9	75.3W	4	I,G,R?	I,Co,Pa	L
1600	Huynaputina, Peru	-16.6	70.85W	6?	I,G,C,R,Lw?	I,Co,Pa,Lw?	L
?*1605	Momotombo, Nicaragua	12.42	86.5W	4	I,G?,A	M	L?
*1619	? unknown	trop		?	I,G,R?	I,Co	
1622	? Colima, Mexico	19.51	103.6W	4			
	Raoul Island, Kermadec (C-14: 1630)	-29.0	177.9W	4	I?,C,R	I,Co	
1641	Parker, Indonesia	-6.06	124.5E	6	I,G,C,R	I,Co	L
1660	? Teon, Banda	-6.92	129.1E	4?			
	? Guagua Pichinchia, Ecuador	-0.17	78.6W	4	I,G	I,Co?	L
1665	? Long Island, New Guinea (C-14: 1660)	-5.35	147.1E	6?	I,G,R	I,Co?	L
1674	Gamkonora, Indonesia	1.38	127.5E	5?	I?,G,C,R	Co,M?	L
1680	Tongkoko, Sulawesi	1.5	125.2E	5?	C,R?	I,Co?	L
1693	Serua, Banda	-6.3	130.0E	4?	I,G,C,R?	I,Co	L
1712	? Awu, Indonesia	3.67	125.5E	3	I,G?,C	I,Co?	L
?1721	Raoul Island, Kermadec (C-14: 1720)	-29.0	177.9E	4			
	Cerro Bravo, Colombia (T)	5.09	75.3W	4	I,G?,C,A?,R?	I	
1728	? Sangay, Ecuador	-2.03	78.3W	3	I,G,C,R	I,Co	
?1737	Fuego, Guatemala	14.47	90.88W	4?	G,C	Co?	
1744	Cotopaxi, Ecuador	-0.68	78.4W	4	I,C,R?	I	L
?1749	? Taal, Philippines	14.0	120.9E	3	I?,R?	I	
1752	? Little Sunda, Indonesia (Tambora?)	-8.0(?)	118E?		G?,C	I,Co?	L
1760	Michoacan, Mexico	19.48	102.3W	4			
	Makian, Indonesia	0.32	127.4E	4?	I,G,R?	Co?,Le?	L
1774	? Papandajan, Indonesia	-7.32	107.7E	3			
	? Tungurahua, Ecuador	-1.47	78.4W	3	G?,C?,R?	I	L
1789	? unknown	trop		?	I,C	I	
1794	? San Martin, Mexico	18.57	95.2W	4?	I?,G	I	
1808	unknown	trop		?	I,G,C,A?,R,Lw,Da	I,S,Co,Da,Pa,Lw	L
1813	Soufriere St. Vincent, W-Indies	13.33	61.2W	4			
	Awu, Indonesia	3.67	125.5E	4?			
	Suwanose-Jima, Japan	29.5	129.7E	4	I,R	I,Da	L
1815	Tambora, Sunda	-8.25	118E	7	I,G,C,A?,R,Da,Lw	I,S,Co,Da,Pa,Lw	L
1823	Galunggung, Java	-7.25	108.1E	5	I,G?,C?,A?	Co?,Da,M	L
1831	Babuyan Claro, Philippines	19.52	121.9E	4?	I,G,C,A?,R,Lw	I,S?,Co,Lw	L
1835	Coseguina, Nicaragua	12.98	87.6W	5	I,G,C,Lw	I,S?,Co,Lw	L
1861	Makian, Indonesia	0.32	127.4E	4?	I,G,R?	S,Co	L
1880	Fuego, Guatemala	14.47	90.9W	4?			
	Cotopaxi, Ecuador	-0.68	78.4W	3	I,C	I	
1883	Krakatoa, Sunda	-6.1	105.4E	6	I,G,C,R,Lw	I,S,Co,Lw,Bo	L,St
1890	Colima, Mexico	19.51	103.6W	4	I,G,A?,R?	I,S?,Co,Bo?	St
1902	Pelee, W-Indies	14.82	61.2W	4			
	Soufriere St. Vincent, W-Indies	13.33	61.2W	4	I,G,C	I,Co	L,St
1903	Santa Maria, Guatemala	14.76	91.5W	6?	I,G,C,R	I,Co,Bo	L,St
?1911	Lolobau, SW-Pacific	-4.9	151.2E	4			
	Taal, Philippines	14.0	120.9E	4			
	Semeru, Java	-8.1	112.9E	3	I,C	I,Co?,Bo?	Ha
1928	Paluweh, Sunda	-8.32	121.7E	3	I,G,A?,St	LF?,Bo?	St
1953	Ambrym, Vanuatu	-16.0	168.1E	4+			
	Lamington, New Guinea	-9.0	148.1E	4			
	Bagana, SW-Pacific	-6.0	155.2E	4	I,G?,A?	I,LF?,Bo?	L*
1963	Agung, Sunda	-8.34	115.5E	4	I?,C,A?	I,Co,LF,Bo	L,DH,Sa
1968	Fernandina, Galapagos	-0.37	91.5W	4	I,G,C,A,R	I?	L,Sa
1974	Fuego, Guatemala	14.47	90.9W	4	C,R?	LF?,Bo	HR,V,Sa
1982	El Chichon, Mexico	17.36	93.2W	5	I,G?,A,R,Z	LF	Th,Ho,Sa
1991	Pinatubo, Philippines	15.13	120.3E	6	A,Z	CoD,Di,Kr	Mi,Mc,Sa

Table A.2: *Normalised average temperature (column two) of the five pre- and five post-eruption summers displayed in figure 5.9. The different quantiles after a Monte Carlo re-sampling (c.f section 4.3) are shown in columns three to six. Years with positive composite temperatures (P) at the 95% and 99% confidence level are marked by P* and P**, respectively; Years with negative composite temperatures (N) at the 95% and 99% confidence level are marked by N* and N**, respectively.*

Years	Mean temp.	0.50%	2.50%	97.50%	99.5%	Significance
-4	0.049	-0.291	-0.22	0.229	0.3	P
-3	0.131	-0.295	-0.224	0.233	0.309	P
-2	-0.036	-0.283	-0.223	0.226	0.298	N
-1	-0.158	-0.289	-0.221	0.222	0.299	N
0	0.143	-0.286	-0.222	0.236	0.307	P
1	-0.144	-0.286	-0.217	0.234	0.297	N
2	-0.447	-0.286	-0.22	0.231	0.299	N**
3	0.201	-0.288	-0.215	0.233	0.305	P
4	0.267	-0.29	-0.217	0.229	0.309	P*
5	-0.007	-0.289	-0.226	0.231	0.31	N

Table A.3: *Normalised average temperature (column two) of the five pre- and five post-eruption winters displayed in figure 5.10. The different quantiles after a Monte Carlo re-sampling (c.f section 4.3) are shown in columns three to six. Years with positive composite temperatures (P) at the 95% and 99% confidence level are marked by P* and P**, respectively; Years with negative composite temperatures (N) at the 95% and 99% confidence level are marked by N* and N**, respectively.*

Years	Mean temp.	0.50%	2.50%	97.50%	99.5%	Significance
-4	-0.059	-0.662	-0.502	0.495	0.643	N
-3	0.356	-0.663	-0.513	0.508	0.658	P
-2	0.267	-0.676	-0.51	0.504	0.636	P
-1	-0.003	-0.669	-0.509	0.489	0.629	N
0	-0.547	-0.658	-0.498	0.495	0.648	N*
1	0.042	-0.722	-0.518	0.483	0.616	P
2	0.73	-0.681	-0.515	0.493	0.637	P**
3	-0.352	-0.665	-0.512	0.479	0.634	N
4	0.314	-0.686	-0.508	0.488	0.646	P
5	-0.749	-0.656	-0.51	0.499	0.65	N**

Table A.4: *Normalised winter NAO index (column two), reconstructed by Luterbacher et al. (2002a), of the five pre- and five post-eruption winters displayed in figure 5.18. The different quantiles after a Monte Carlo resampling (c.f section 4.3) are shown in columns three to six. Years with positive composite NAOI (P) at the 95% and 99% confidence level are marked by P* and P**, respectively; Years with negative NAOI (N) at the 95% and 99% confidence level are marked by N* and N**, respectively.*

Years	NAO index	0.50%	2.50%	97.50%	99.5%	Significance
-4	-0.24	-0.547	-0.42	0.416	0.537	N
-3	-0.057	-0.538	-0.413	0.409	0.542	N
-2	0.145	-0.538	-0.421	0.413	0.543	P
-1	0.099	-0.53	-0.42	0.416	0.533	P
0	-0.332	-0.526	-0.417	0.409	0.528	N
1	-0.098	-0.552	-0.425	0.412	0.537	N
2	0.486	-0.552	-0.413	0.406	0.537	P*
3	0.015	-0.548	-0.423	0.415	0.546	P
4	0.512	-0.534	-0.41	0.404	0.534	P*
5	-0.531	-0.536	-0.422	0.413	0.536	N*

Table A.5: *Normalised winter NAO index (column two), reconstructed by Cook et al. (2002), of the five pre- and five post-eruption winters displayed in figure B.11. The different quantiles after a Monte Carlo resampling (c.f section 4.3) are shown in columns three to six. Years with positive composite NAOI (P) at the 95% and 99% confidence level are marked by P* and P**, respectively; Years with negative NAOI (N) at the 95% and 99% confidence level are marked by N* and N**, respectively.*

Years	NAO index	0.50%	2.50%	97.50%	99.5%	Significance
-4	-0.07	-0.47	-0.36	0.36	0.46	N
-3	-0.30	-0.47	-0.36	0.36	0.46	N
-2	0.23	-0.48	-0.36	0.36	0.47	P
-1	0.02	-0.47	-0.36	0.36	0.46	P
0	-0.14	-0.47	-0.36	0.37	0.46	N
1	0.11	-0.47	-0.36	0.36	0.46	P
2	0.08	-0.47	-0.36	0.36	0.47	P
3	0.06	-0.47	-0.36	0.36	0.46	P
4	0.22	-0.46	-0.36	0.36	0.47	P
5	-0.22	-0.47	-0.36	0.35	0.46	N

Appendix B

Additional Plots

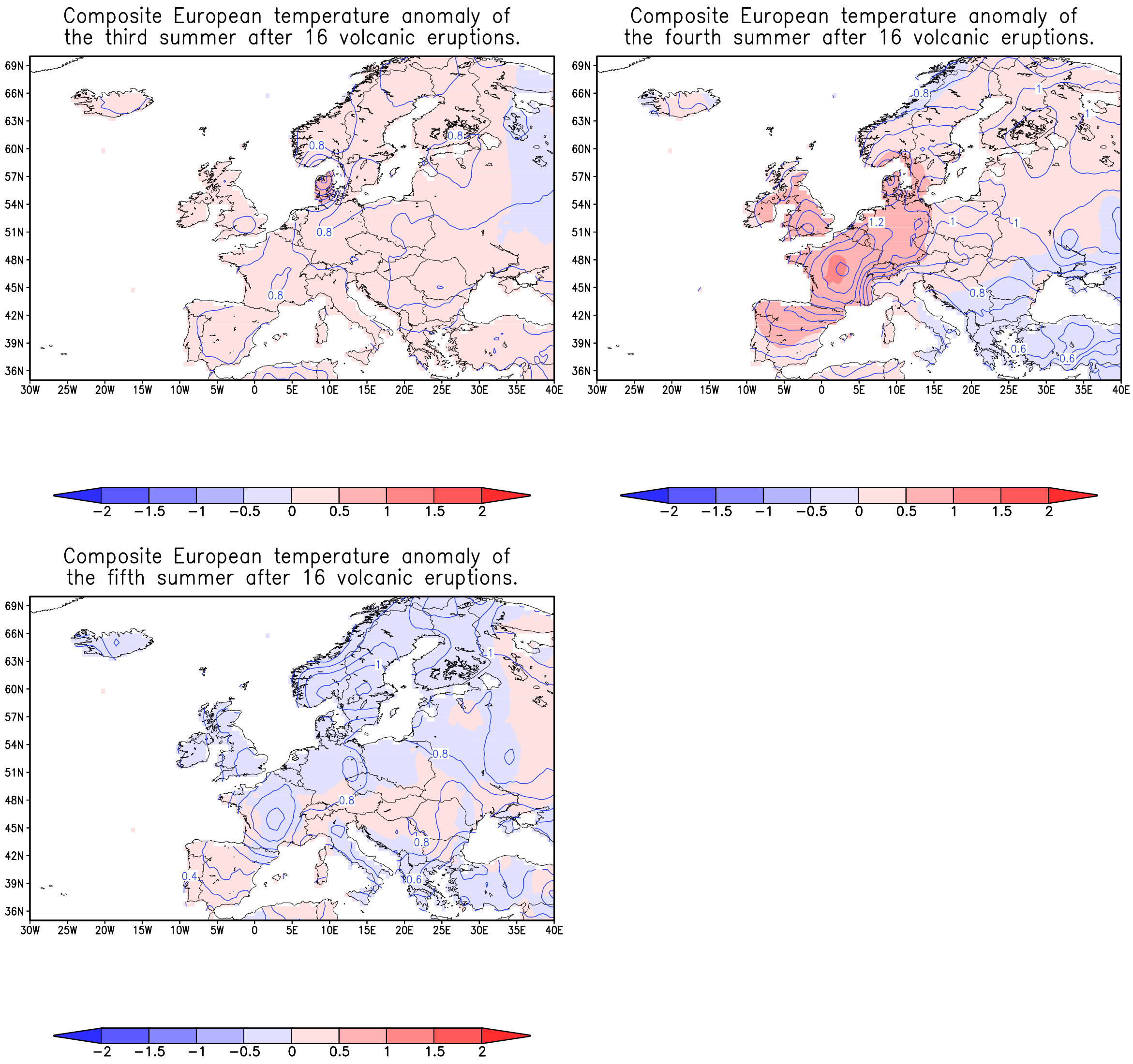

Composite European temperature anomaly of the third summer after 16 volcanic eruptions.

Composite European temperature anomaly of the fourth summer after 16 volcanic eruptions.

Composite European temperature anomaly of the fifth summer after 16 volcanic eruptions.

Figure B.1: *Composite surface temperature anomaly fields (°C, shaded) of the third (upper left panel), fourth (upper right panel) and fifth (lower panel) summer following 16 tropical volcanic eruptions. The blue contours mark the standard deviations in °C.*

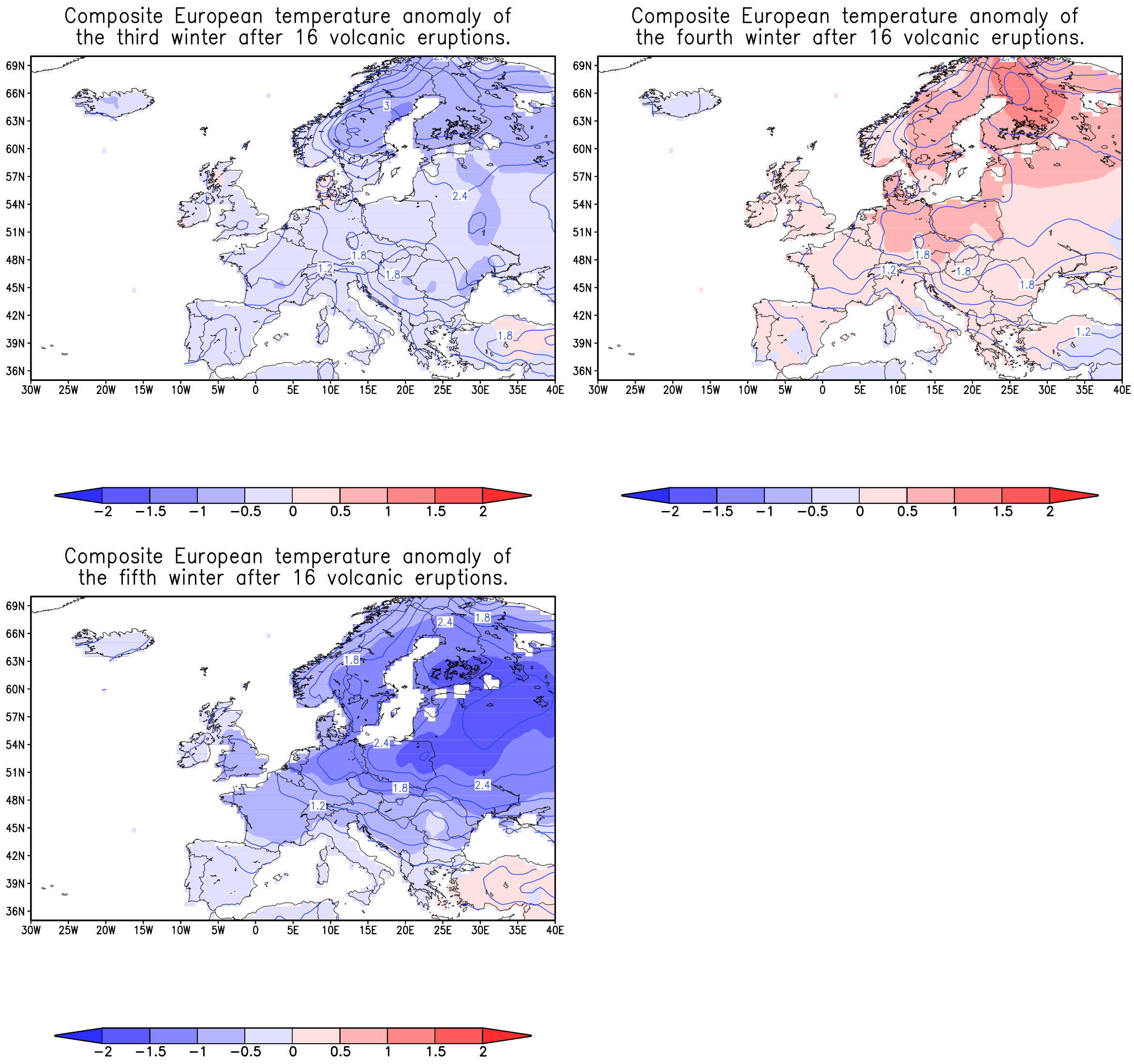

Figure B.2: *Composite surface temperature anomaly fields (°C, shaded) of the third (upper left panel), fourth (upper right panel) and fifth (lower panel) winter following 16 tropical volcanic eruptions. The blue contours mark the standard deviations in °C.*

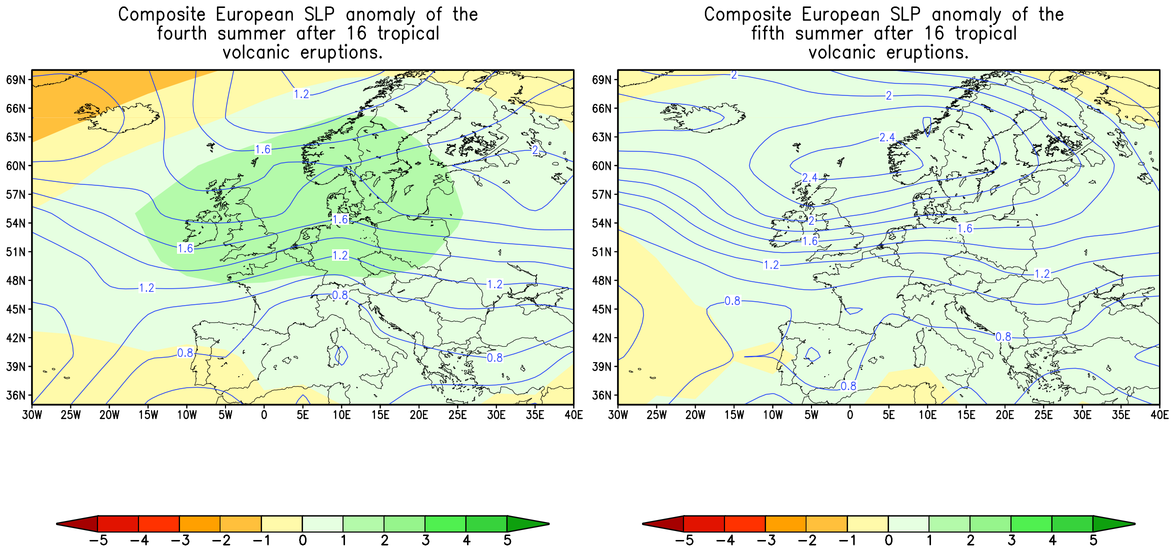

Figure B.3: *Composite SLP anomaly fields (hPa, shaded) of the fourth (left panel) and fifth (right panel) summer following 16 tropical volcanic eruptions. The blue contours mark the standard deviations in hPa.*

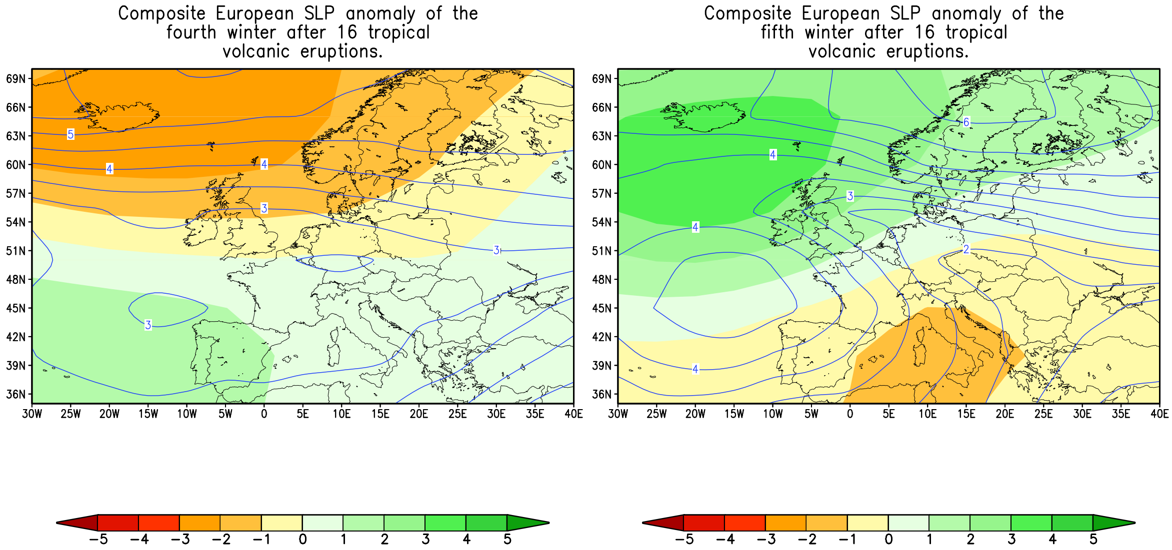

Figure B.4: *Composite SLP anomaly fields (hPa, shaded) of the fourth (left panel) and fifth (right panel) winter following 16 tropical volcanic eruptions. The blue contours mark the standard deviations in hPa.*

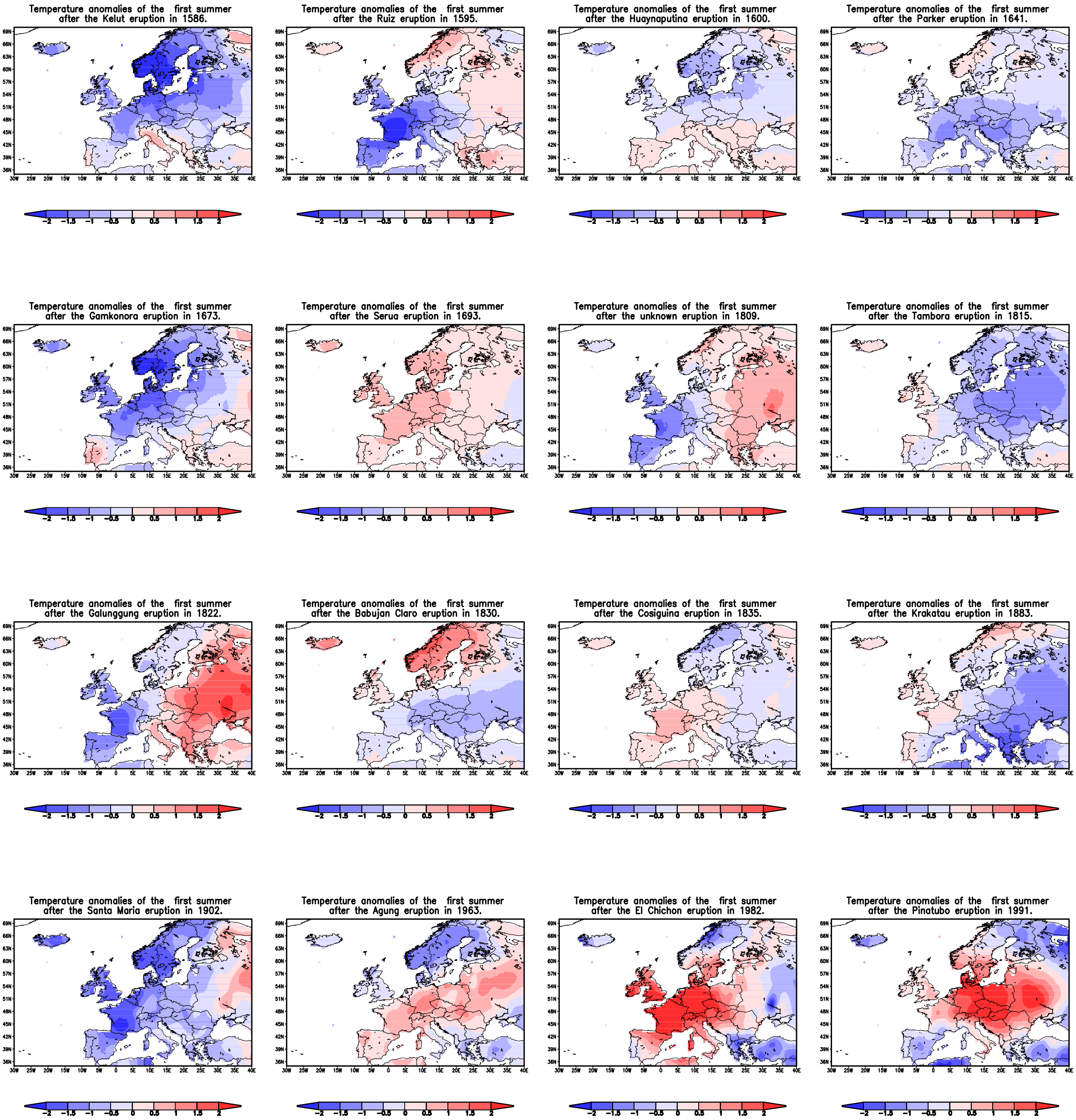

Figure B.5: *European land surface temperature anomaly field (°C, shaded) of the first summer following each of the 16 selected major volcanic eruptions averaged in figure 5.3.*

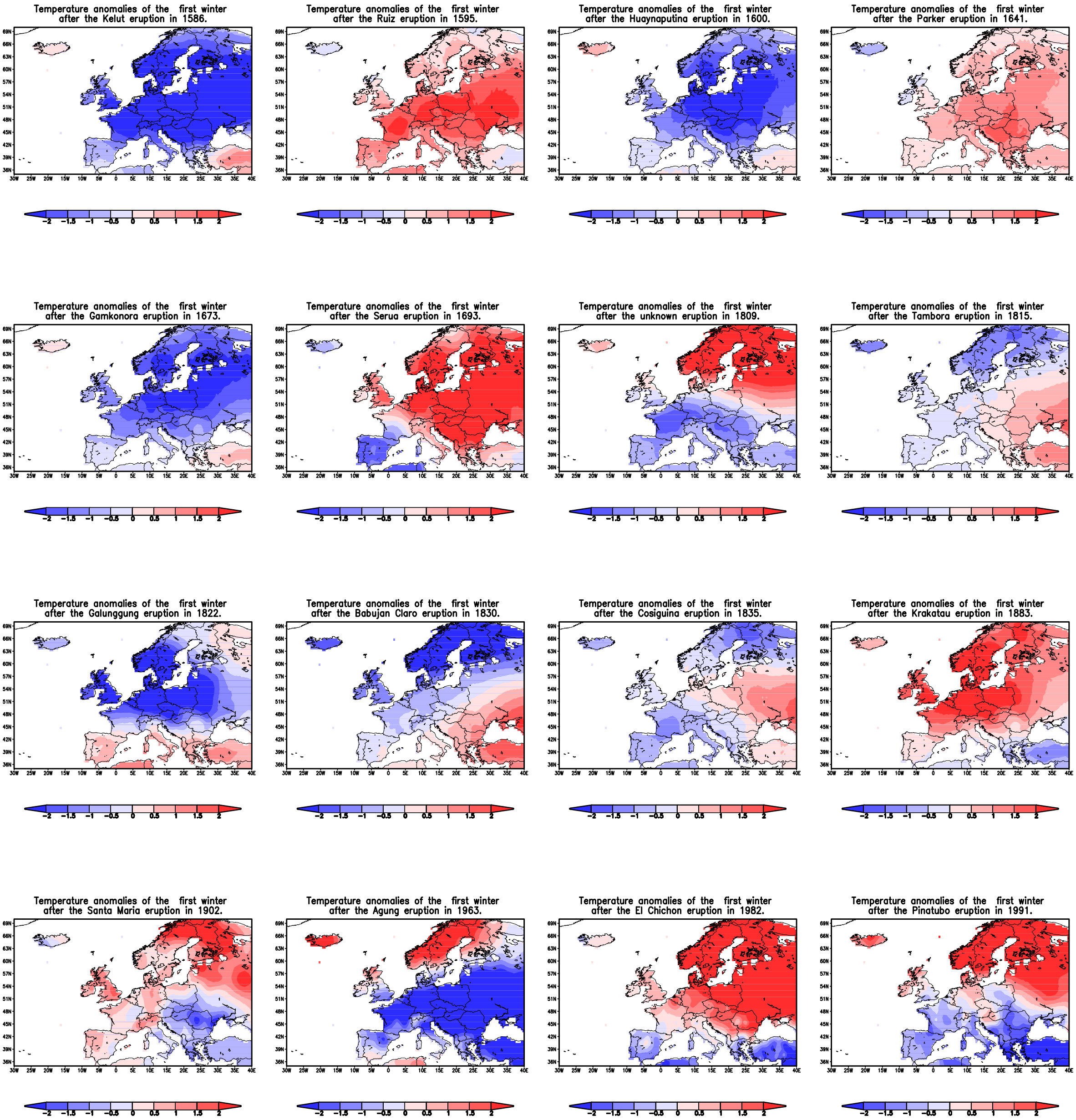

Figure B.6: *European land surface temperature anomaly field (°C, shaded) of the first winter following each of the 16 selected major volcanic eruptions averaged in figure 5.3.*

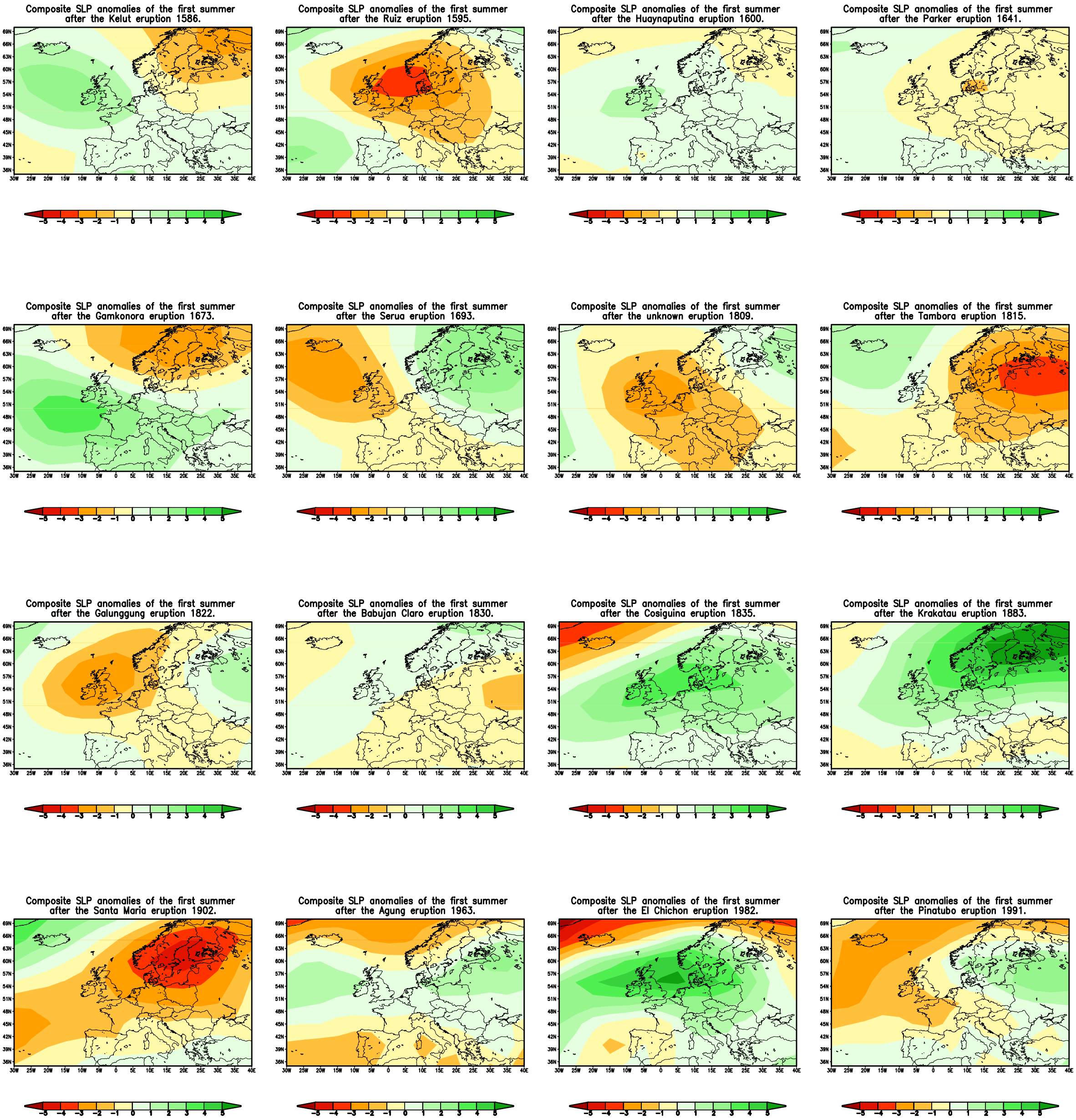

Composite SLP anomalies of the first summer after the Kelut eruption 1586.

Composite SLP anomalies of the first summer after the Ruiz eruption 1595.

Composite SLP anomalies of the first summer after the Huaynaputina eruption 1600.

Composite SLP anomalies of the first summer after the Parker eruption 1641.

Composite SLP anomalies of the first summer after the Gamkonora eruption 1673.

Composite SLP anomalies of the first summer after the Serua eruption 1693.

Composite SLP anomalies of the first summer after the unknown eruption 1809.

Composite SLP anomalies of the first summer after the Tambora eruption 1815.

Composite SLP anomalies of the first summer after the Galunggung eruption 1822.

Composite SLP anomalies of the first summer after the Babujan Claro eruption 1830.

Composite SLP anomalies of the first summer after the Cosiguina eruption 1835.

Composite SLP anomalies of the first summer after the Krakatau eruption 1883.

Composite SLP anomalies of the first summer after the Santa Maria eruption 1902.

Composite SLP anomalies of the first summer after the Agung eruption 1963.

Composite SLP anomalies of the first summer after the El Chichon eruption 1982.

Composite SLP anomalies of the first summer after the Pinatubo eruption 1991.

Figure B.7: *European SLP anomaly fields (hPa, shaded) of the first summer following each of the 16 selected major volcanic eruptions averaged in figure 5.13.*

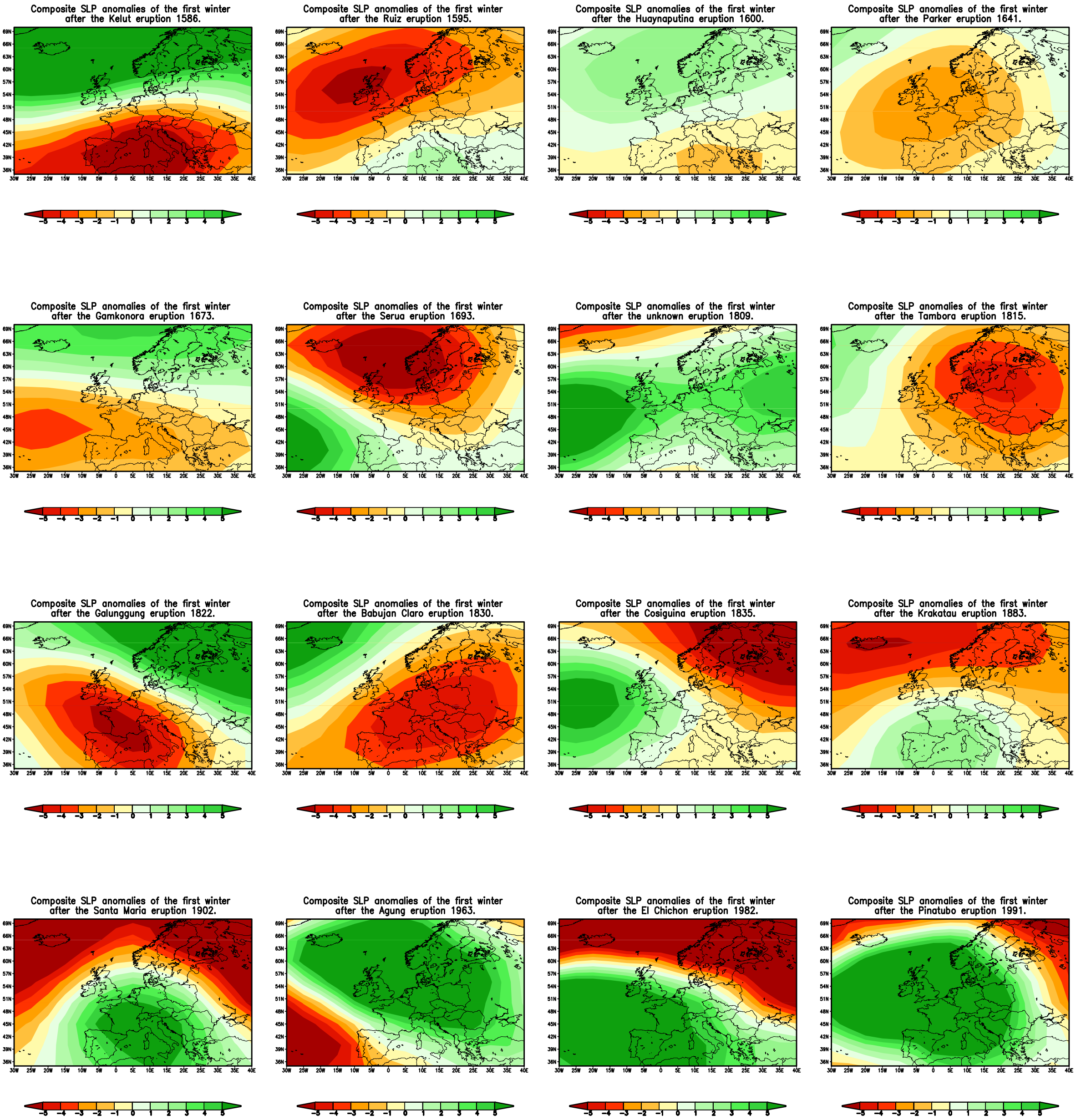

Figure B.8: *European SLP anomaly fields (hPa, shaded) of the first winter following each of the 16 selected major volcanic eruptions averaged in figure 5.15.*

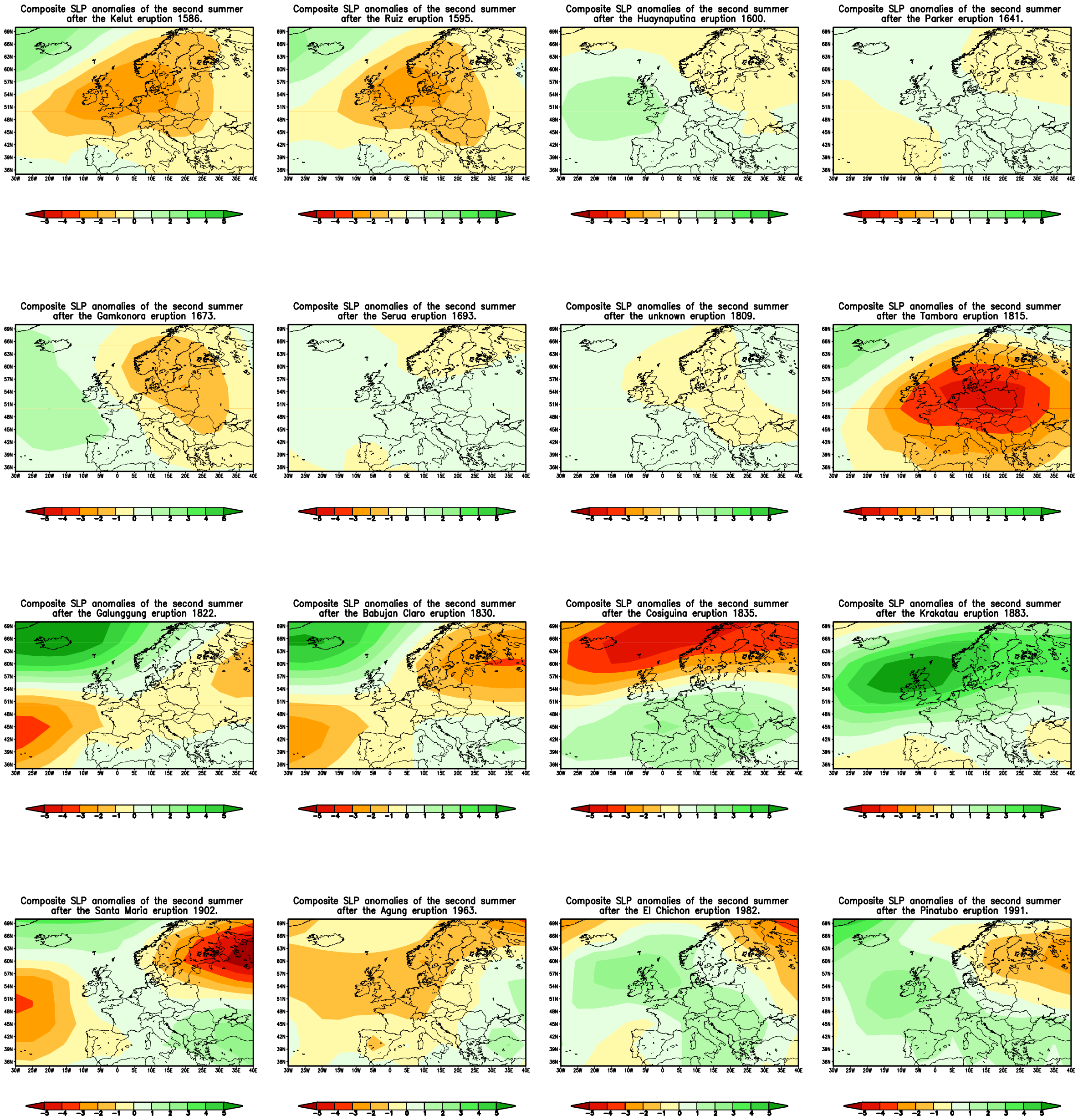

Composite SLP anomalies of the second summer after the Kelut eruption 1586.

Composite SLP anomalies of the second summer after the Ruiz eruption 1595.

Composite SLP anomalies of the second summer after the Huaynaputina eruption 1600.

Composite SLP anomalies of the second summer after the Parker eruption 1641.

Composite SLP anomalies of the second summer after the Gamkonora eruption 1673.

Composite SLP anomalies of the second summer after the Serua eruption 1693.

Composite SLP anomalies of the second summer after the unknown eruption 1809.

Composite SLP anomalies of the second summer after the Tambora eruption 1815.

Composite SLP anomalies of the second summer after the Galunggung eruption 1822.

Composite SLP anomalies of the second summer after the Babujan Claro eruption 1830.

Composite SLP anomalies of the second summer after the Cosiguina eruption 1835.

Composite SLP anomalies of the second summer after the Krakatau eruption 1883.

Composite SLP anomalies of the second summer after the Santa Maria eruption 1902.

Composite SLP anomalies of the second summer after the Agung eruption 1963.

Composite SLP anomalies of the second summer after the El Chichon eruption 1982.

Composite SLP anomalies of the second summer after the Pinatubo eruption 1991.

Figure B.9: *European SLP anomaly fields (hPa, shaded) of the second summer following each of the 16 selected major volcanic eruptions averaged in figure 5.13.*

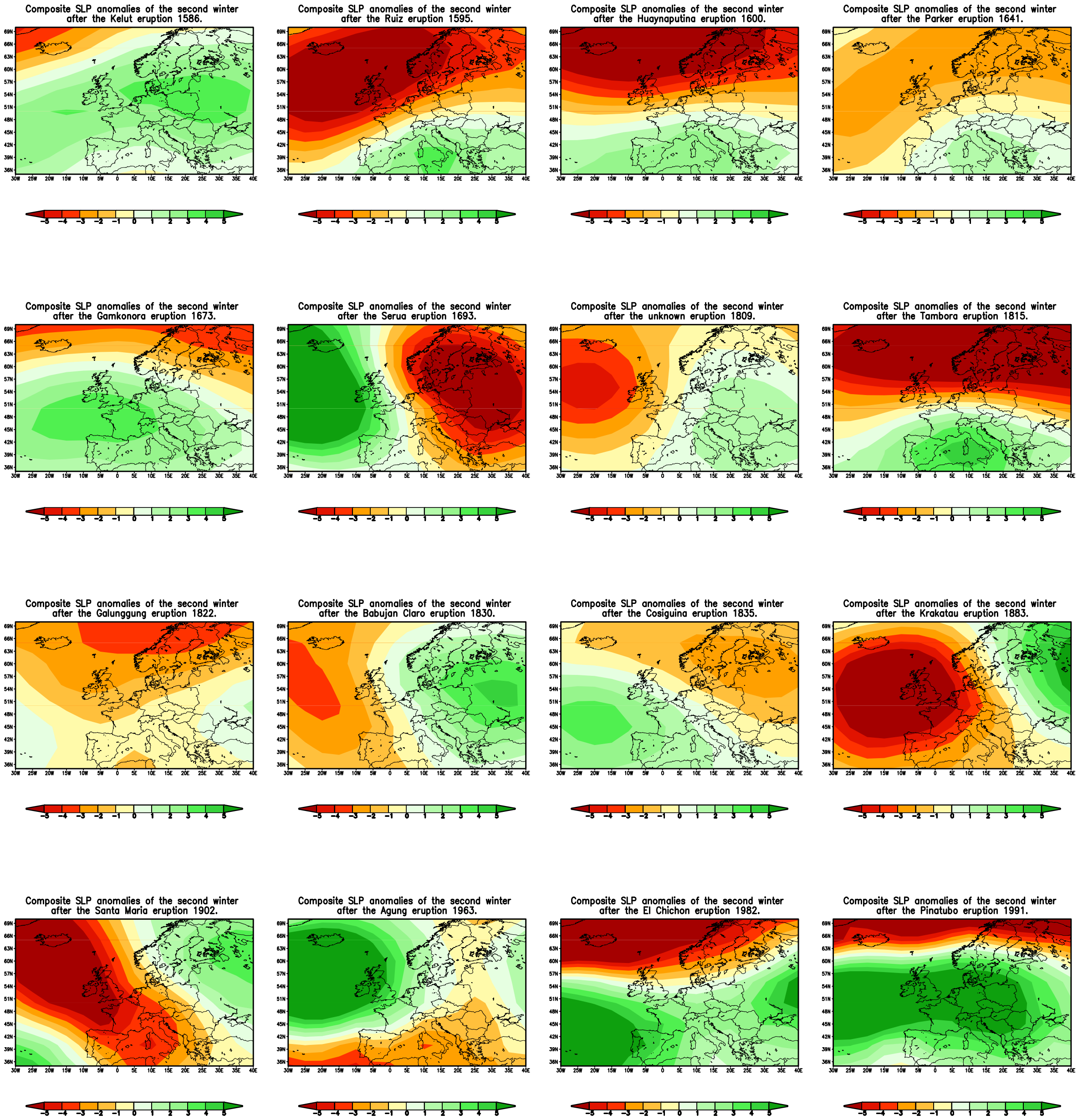

Composite SLP anomalies of the second winter after the Kelut eruption 1586.

Composite SLP anomalies of the second winter after the Ruiz eruption 1595.

Composite SLP anomalies of the second winter after the Huaynaputina eruption 1600.

Composite SLP anomalies of the second winter after the Parker eruption 1641.

Composite SLP anomalies of the second winter after the Gamkonora eruption 1673.

Composite SLP anomalies of the second winter after the Serua eruption 1693.

Composite SLP anomalies of the second winter after the unknown eruption 1809.

Composite SLP anomalies of the second winter after the Tambora eruption 1815.

Composite SLP anomalies of the second winter after the Galunggung eruption 1822.

Composite SLP anomalies of the second winter after the Babujan Claro eruption 1830.

Composite SLP anomalies of the second winter after the Cosiguina eruption 1835.

Composite SLP anomalies of the second winter after the Krakatau eruption 1883.

Composite SLP anomalies of the second winter after the Santa Maria eruption 1902.

Composite SLP anomalies of the second winter after the Agung eruption 1963.

Composite SLP anomalies of the second winter after the El Chichon eruption 1982.

Composite SLP anomalies of the second winter after the Pinatubo eruption 1991.

Figure B.10: *European SLP anomaly fields (hPa, shaded) of the second winter following each of the 16 selected major volcanic eruptions averaged in figure 5.15.*

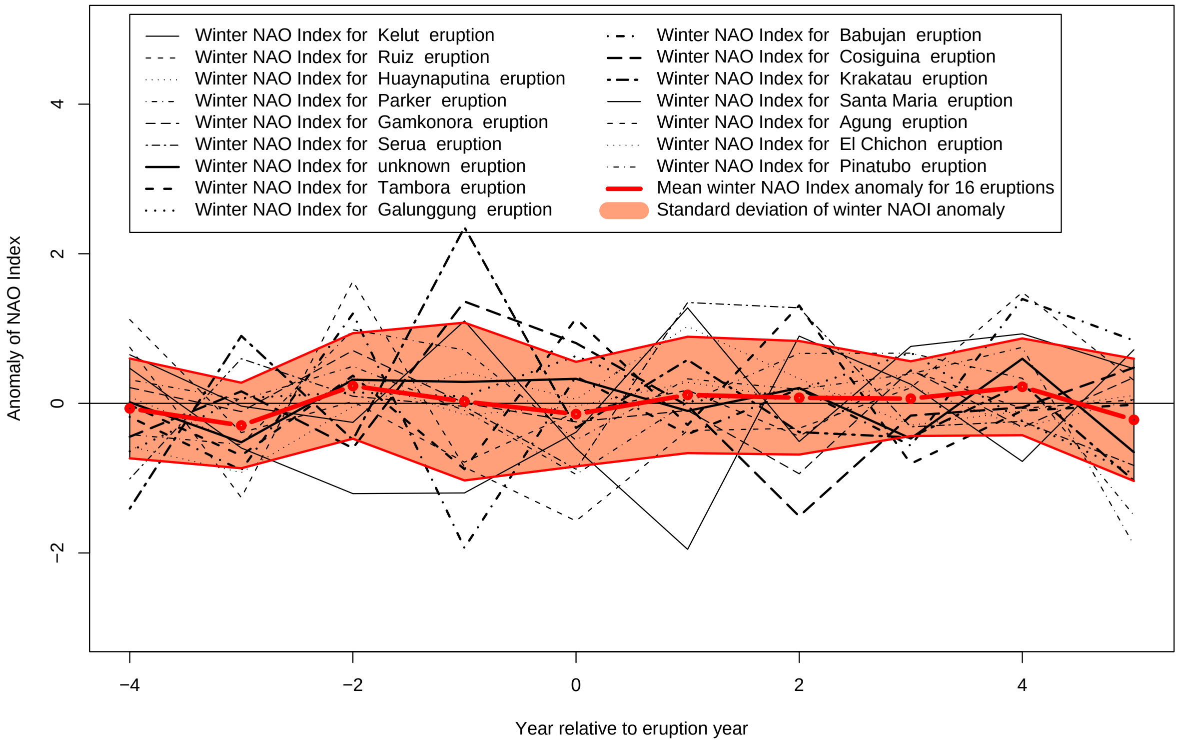

Figure B.11: *Normalised winter NAOI (December to March), reconstructed by Cook et al. (2002), for 16 tropical volcanic eruptions and composite winter NAOI (thick red line) with standard deviations (orange).*